

ERRATA

Equation 2.12 should read

$$t_{K0}(I) = I^K \hat{K} \hat{I} \sqrt{\frac{(2I - K)!}{(2I + K + 1)!} \frac{(2K)!}{(K!)^2}} f_K \quad (1)$$

Equation 3.11 should be

$$\begin{aligned} \sigma_T(\theta, \phi, t) = & \sigma_0 + P_2(\cos(\theta + \phi))P_2(\cos 80^\circ)t_{20}^{planar}(t)\sigma_2 \\ & + P_4(\cos(\theta + \phi))P_4(\cos 80^\circ)t_{40}^{planar}(t)\sigma_4. \end{aligned}$$

and equation 3.14,

$$\begin{aligned} \ln N^*(\theta, \phi, t) = & \ln(N_0^* e^{-n\sigma_0}) - P_2(\cos(\theta + \phi))P_2(\cos 80^\circ)t_{20}^{planar}(t)n\sigma_2 \\ & - P_4(\cos(\theta + \phi))P_4(\cos 80^\circ)t_{40}^{planar}(t)n\sigma_4 \end{aligned} \quad (2)$$

Equation 6.24 should be

$$p_y = \frac{1}{2}[\hat{t}_{10}^+(1/2) - \hat{t}_{10}^-(1/2)], \quad (3)$$

and equation 6.25 should be

$$\hat{t}_{10}^\pm(1/2) = K_y^y(0^\circ)\hat{t}_{10}^\pm(p). \quad (4)$$

Abstract

KOSTER, JAMES EDWARD. A Test of Time Reversal Invariance with Polarized Neutrons and Aligned ^{165}Ho . (Under the direction of Christopher Robert Gould.)

A test of time reversal invariance in the forward elastic scattering amplitude for 2 MeV polarized neutrons incident on aligned holmium has been conducted. The experiment was sensitive to the five-fold spin correlation (FC) $(\vec{s} \cdot \vec{I} \times \vec{k})(\vec{I} \cdot \vec{k})$ where \vec{s} and \vec{k} are the spin and momentum of the neutron and \vec{I} is the spin of the ^{165}Ho target. This correlation is parity conserving but odd under time reversal. Data were obtained with the Triangle Universities Nuclear Laboratory polarized beam facility and its Cryogenic Polarized Target Facility. The rotating target cryostat aligned the holmium single crystal and rotated it in the horizontal plane at temperatures below 280 millikelvin. The neutron polarization was reversed every 100 milliseconds and the alignment axis of the holmium was rotated relative to the neutron beam every 14 minutes. An asymmetry was extracted at each angle by comparing the transmission for neutrons of opposite polarization. A T-violating FC analyzing power of $(1.0 \pm 6.3) \times 10^{-4}$ was derived. Systematic errors and effects due to the sequential action of T-even amplitudes are shown to be negligible. This test of reciprocity is compared to detailed balance tests of forward and backward reaction rates with unpolarized nuclei.

Novel measurements of the nuclear deformation effect in holmium are also presented. The deformation effect cross sections agree very well with previous data. A coupled channels, optical model calculation of the energy dependent deformation effect is presented. Deformation parameters $\beta_2 = 0.29$, $\beta_4 = -0.02$, and $\beta_6 = 0.08$ are derived from fits to the data and are compared to other deformation parameters used in the literature.

A TEST OF
TIME REVERSAL INVARIANCE
WITH POLARIZED NEUTRONS
AND ALIGNED ^{165}HO


by
JAMES EDWARD KOSTER

A thesis submitted to the Graduate Faculty of
North Carolina State University
in partial fulfillment of the
requirements for the Degree of
Doctor of Philosophy

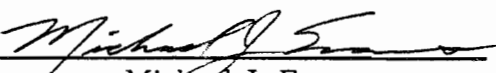
Department of Physics

Raleigh
1990

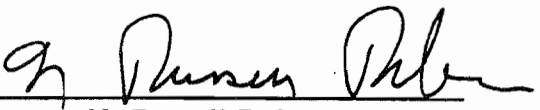
APPROVED BY:



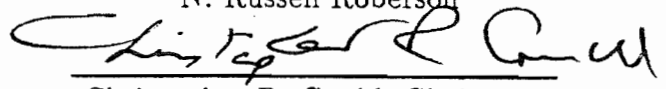
David G. Haase



Michael J. Evans



N. Russell Roberson



Christopher R. Gould, Chairman

BIOGRAPHY

James Edward Koster

Personal

Born in Lancaster, Pennsylvania, July 24, 1963

Married Holly Ann Shamberger, July 17, 1982

Education

B.S., Texas Christian University, Fort Worth, Texas, 1985

Positions

Astronomy Laboratory Instructor, TCU, 1982-1985

President, TCU Chapter of Society of Physics Students, 1984-1985

Teaching Assistant, NCSU, 1985-1987

Research Assistant, NCSU, 1987-present

Professional Affiliations

American Physical Society

Sigma Pi Sigma

Sigma Xi

Publications

A Mechanism for Precise Rotation of Nuclear Targets at Low Temperatures, J.E. Koster, C.R. Gould, D.G. Haase, and N.R. Roberson, *Physica B* **165**, 153 (1990).

Comment on Superconducting Fixed Points and Interpolations, J.E. Koster, D.G. Haase, and R.G. Goodrich, *Cryogenics* **29**, 1017 (1989).

Studies of Parity and Time Reversal Symmetries in Neutron Scattering from ^{165}Ho , D.G. Haase, C.R. Gould, J.E. Koster, N.R. Roberson, L.W. Seagondollar, J.P. Soderstrum, M.B. Schneider, and X. Zhu, *Hyperfine Interactions* **43**, 133 (1988).

Contributed Abstracts

Holmium Deformation Effect Measured with a Rotating Aligned Target, J.E. Koster, C.R. Gould, D.G. Haase, L.W. Seagondollar, N.R. Roberson, W.S. Wilburn, and X. Zhu, *Bull. Am. Phys. Soc.* **35**, 926 (1990).

An Aligned Nuclear Target Cryostat, J.E. Koster, C.R. Gould, D.G. Haase, N.R. Roberson, and X. Zhu, Bull. Am. Phys. Soc. **33**, 2199 (1988).

A Cryostat for Testing Time Reversal Invariance in Aligned Holmium, J.E. Koster, C.R. Gould, D.G. Haase, N.R. Roberson, and X. Zhu, Bull. Am. Phys. Soc. **33**, 1589 (1988).

Compound Nucleus Contributions to Spin-Spin Cross Sections, J.E. Koster, C.R. Gould, and X. Zhu, Bull. Am. Phys. Soc. **31**, 1763 (1986).

Radiation Spectra from Electron Bombardment of Non-Thin Targets, J.E. Koster, L. Estep, and C.A. Quarles, Bull. Am. Phys. Soc. **29**, 1106 (1984).

Co-authored Abstracts

Report on Operation of the New TUNL Intense Atomic Beam Polarized Source and ECR Ionizer, T.B. Clegg, et. al., Proceedings, 7th International Conference on Polarization Phenomena, PARIS (1990), 3E.

Brute Force Polarized Nuclear Targets for Neutron Scattering Experiments, D.G. Haase, O.K. Baker, C.R. Gould, C.D. Keith, J.E. Koster, N.R. Roberson, and J.P. Soderstrum, contribution to the 1989 IUCF Topical Conference "Physics with Polarized Beams on Polarized Targets", World Scientific (1990).

Cold Fusion, J.E. Koster, Proceedings, Hampton University Graduate Studies at CEBAF, Physics Division/CEBAF (1990), 134.

ACKNOWLEDGEMENTS

Nothing is carried out in isolation; fortunately a thesis provides a chance to say “Thanks” in print. The members of my committee and research group have been good role models—as professional researchers and as teachers. I hope I can emulate their qualities in the future. Chris Gould, Dave Haase, and Russell Roberson have imparted knowledge each in very different areas; more importantly, they have also been friends. I thank Worth Seagondollar for his colorful anecdotes about the people and events in nuclear physics that preceded me. C.A. Quarles served me my first taste of real research. I have enjoyed the company of all the students and postdocs, past and present, in the polarized target group, particularly Joe Zhu, Scott Wilburn, and Chris Keith. The other students and staff at TUNL have always gone out of their way to be helpful. I am grateful, and aspire to be so helpful in kind. Paul Carter, Bob Rummel, and Ken Sweeton have kept the various components of the lab in reliable working order—no small feat. Sidney Edwards and Pat Mulkey have always been ready with projects and with wit, regardless of how little lead time I gave them. I have been spoiled by the excellent advice and beautiful work of Al Lovette and his staff at the TUNL machine shop, and the staff of the NCSU machine shop. I must also thank Frank Bratsch, whose timely supply of liquid helium has made this research so less difficult. I thank Pat Gibson and Karen Mitchell for their cheerful assistance. I appreciate the financial and advisorial support of Gary Mitchell and Ed Bilpuch that has made my work

possible and enabled me to travel to present it. The friendliness and helpfulness of the students from Duke and UNC are a model to all. Special thanks to Paul Felsher for his willing help in typography.

I have enjoyed and benefitted from discussions with Dave Davis, Jean-Paul De-
laroche, and Artur Thiel. Steve Krieger and Phillip Young have graciously pro-
vided calculations as well.

Finally, to my son, I ask of the world that you be given opportunities as I have—
what you make of them is up to you. This dissertation is dedicated with love
to my wife Holly, whose love and encouragement have sustained me in this—my
self-indulgence—these many years.

Contents

LIST OF FIGURES	ix
LIST OF TABLES	xii
1 INTRODUCTION	1
2 EXPERIMENTAL APPARATUS	11
2.1 NUCLEAR ORIENTATION	11
2.2 HOLMIUM SPIN STRUCTURE	15
2.3 ROTATING TARGET REFRIGERATOR	19
2.3.1 DILUTION REFRIGERATOR CRYOSTAT	19
2.3.2 ROTATION SYSTEM	23
2.3.3 HOLMIUM TARGET	28
2.3.4 THERMOMETRY	30
2.3.5 ELECTRONICS	31
2.4 UNPOLARIZED NEUTRONS	34
3 NUCLEAR DEFORMATION EFFECT MEASUREMENT	46
3.1 DATA ACQUISITION	46
3.2 DATA REDUCTION AND ANALYSIS	47
3.3 DEFORMATION EFFECT RESULTS	64

4	COUPLED CHANNELS CALCULATION OF DEFORMATION EFFECT	70
4.1	FORMALISM	70
4.2	RESULTS	72
4.3	COMPARISON TO OTHER DEFORMATION PARAMETERS .	79
4.4	DISCUSSION	81
5	POLARIZED BEAM APPARATUS	83
5.1	PREPARATION OF POLARIZED BEAM	83
5.2	MONITORING OF POLARIZED BEAM	86
5.3	FAST SPIN-FLIP	89
5.4	VAX INTERFACE AND DATA ACQUISITION	91
6	FIVE-FOLD CORRELATION MEASUREMENT	96
6.1	ANALYSIS	96
6.2	TRI CONTRIBUTIONS TO SPIN ASYMMETRY	100
6.3	RESULTS	105
6.4	DISCUSSION OF RESULTS	109
7	CONCLUSIONS	113
8	APPENDICES	115
8.1	HOLMIUM TARGET THICKNESS	115
8.2	DEFORMATION CALCULATION CODE	120
	REFERENCES	122

List of Figures

1.1	Geometry for the five-fold correlation.	4
1.2	Transmission of polarized neutrons through an aligned target, and the time reversed scattering.	5
2.1	Nuclear Orientation.	12
2.2	Nuclear spins in a holmium single crystal.	16
2.3	Alignment of holmium nuclei in the basal plane as a function of temperature.	17
2.4	Dilution Refrigerator.	21
2.5	Dilution refrigerator gas handling system.	24
2.6	Helium flow rate as a function of still heating.	25
2.7	Rotation system.	26
2.8	Cooling of the holmium target with time.	32
2.9	Mixing chamber temperature as a function of heat input.	33
2.10	Computer control of the rotation drive.	35
2.11	Floor plan of the Triangle Universities Nuclear Laboratory.	36
2.12	59° beam line.	38
2.13	Neutron production cell.	39
2.14	Neutron beam set-up.	41
2.15	Block diagram of electronics for processing detector signals	43

3.1	Ratio of neutron detector yield to beam current, with dead-time correction, at 1.8 MeV	48
3.2	Transmission yield after slow time drift is removed.	52
3.3	Normalized detector yield for 1.8 MeV neutrons and an aligned target.	54
3.4	Fourier transform of transmission through an aligned target.	55
3.5	Normalized detector yield for 1.8 MeV neutrons and an unaligned target.	56
3.6	Fourier transform of transmission through an unaligned target.	57
3.7	Normalized detector yield for 1.5 MeV neutrons and an aligned target.	58
3.8	Fourier transform of the 1.5 MeV data.	59
3.9	Logarithm of yield as a function of angle, with variations in degree of alignment.	62
3.10	Chi-square fit of logarithm of yield as a function of c-axis offset.	63
3.11	The dependence of the goodness of fit, χ^2 , on the coefficient σ_2	65
3.12	Different sets of $\sigma_2(E)$	68
4.1	The dependence of σ_2 on β_2 at 3.9 MeV.	73
4.2	The calculated energy dependent σ_2 and experimental data.	76
4.3	The calculated energy dependent σ_0 and experimental data.	77
4.4	Deduced shape of a ^{165}Ho nucleus.	78
5.1	TUNL Atomic Beam Polarized Ion Source.	84
5.2	Polarimeter for continuous monitoring of proton polarization.	88
5.3	The effect of monotonic change in detector yield with time.	90
5.4	Block diagram of electronics at computer interface.	93
5.5	Logic diagram of the timing signals used for spin-flipping.	94
6.1	Angular dependence of $(\vec{s} \cdot \vec{I})(\vec{I} \cdot \vec{k})$ for coplanar vectors.	104

6.2	Proton polarization during one block of runs.	107
6.3	Angle and spin asymmetries in neutron transmission as a function of θ	110
6.4	Proton beam position in the horizontal plane as a function of run number.	111
8.1	Cross section of cylindrical holmium target.	116
8.2	View of the target within the solid angle of the detector collimator.	118

List of Tables

1.1	Precision of selected P-even T-odd experiments.	8
2.1	Energy losses in neutron production cell.	40
2.2	Dead times in various PSD module configurations.	44
3.1	Experimental parameters for the four measurements of $\sigma_2(E)$. . .	66
3.2	Results of σ_2 measured as a function of incident neutron energy. .	66
4.1	Parameters for the deformed optical model calculation.	71
4.2	Lowest order cross section terms as a function of individual deforma- tions.	74
4.3	Deformation parameters extracted from experimental σ_2 in the present calculation.	79
4.4	Sets of deformation parameters for $A \approx 165$	80
6.1	Spin correlations and their associated beam and target statistical tensor ranks.	98
6.2	Experimental constant parameters for the FC measurement. . . .	105
6.3	Experimental variable parameters for the FC measurement.	106
6.4	Deduced analyzing powers for the FC measurement.	108

Chapter 1

INTRODUCTION

Symmetries in physical interactions and the underlying conservation laws provide vital tools for interpreting physical phenomena. The fundamental discrete symmetries are charge conjugation (C), parity (P), and time reversal (T). Time reversal invariance (TRI) means that a process running backwards in time is as physically plausible as a process running forward in time. This is intuitive in the elastic collision of two billiard balls. A movie of the collision looks realistic when played either forward or backward in time. Many macroscopic processes do not appear at first to be TRI—for instance, the breaking of a bottle. This is because it is exceedingly difficult to set up the reverse process where all glass fragments start from the correct positions with the correct velocities. An equivalent way to understand TRI is that when time t is substituted by $-t$ in an equation governing the motion, the form of the equation is unchanged.

There is indirect evidence that T is not always invariant. The CPT theorem (Lüders 1957) in quantum field theory states that the combination CPT is conserved. A violation of the combination CP therefore implies simultaneous time reversal violation. In 1964 CP violation was discovered in the decay of neutral kaons (Christenson, et. al.). No other indication of time reversal noninvariance (TRNI) has been found in the intervening quarter century. The challenge in the

study of fundamental symmetries is to find another system in which TRNI is manifested.

We first consider the implications of TRI on nuclear scattering. We review the properties of the scattering (S) matrix. (For details see Blatt and Weisskopf 1952, Blin-Stoyle 1973, Frauenfelder and Henley 1975, or Sachs 1987.) The S-matrix can be viewed as the operator transforming an initial state ψ_i into a final state ψ_f . A particular element $S_{\alpha\beta} = \langle \beta | S | \alpha \rangle$ connects an incoming channel α with an outgoing channel β . The probability that the system ends up in channel β given that it began in channel α is just $|S_{\alpha\beta}|^2$. Conservation of the total probability leads to the property $SS^\dagger = 1$ where S^\dagger is the Hermitian conjugate of S . Thus the scattering matrix is unitary. If the system is TRI, then any time reversed state $T\psi$ is an eigenstate of the system when ψ is an eigenstate of the system and T is a time reversal operator. This symmetry leads to the consequence in the S-matrix description of scattering,

$$S_{\alpha\beta} = S_{\beta_T\alpha_T}, \quad (1.1)$$

where α_T is the time reversed channel of α in which all the spins and momenta have been reversed. Equation 1.1 is the “reciprocity” theorem and depends on TRI; its form for angular momentum eigenstates is

$$\langle \vec{k}_\beta, s_\beta, m_\beta | S | \vec{k}_\alpha, s_\alpha, m_\alpha \rangle = (-1)^{s_\alpha + s_\beta - m_\alpha - m_\beta} \langle -\vec{k}_\alpha, s_\alpha, -m_\alpha | S | -\vec{k}_\beta, s_\beta, -m_\beta \rangle. \quad (1.2)$$

Here \vec{k}_α is the relative momentum in channel α , and s and m are the spin and its third component. The time reversed channels are seen to have linear momenta reversed (“motion reversal”) and the spins inverted. The phase in equation 1.2 is not unique—it depends on the definition of the operator T —but is conventional (e.g. Frauenfelder and Henley 1975).

One class of tests follows directly from equation 1.2. By preparing a system successively in the channels α and β_T the relative reaction rates can be compared. These tests search for T-odd spin correlations in neutron scattering. The simplest

parity conserving (P-even) correlation is the five-fold correlation (FC),

$$\vec{s} \cdot (\vec{I} \times \vec{k})(\vec{I} \cdot \vec{k}) \quad (1.3)$$

where \vec{s} and \vec{k} are the spin angular momentum and linear momentum (wavevector) of the incident neutron and \vec{I} is the spin of the target nucleus. This correlation was suggested by Baryshevskii (1983) and elaborated on by Barabanov (1986) and Kabir (1986). Because the FC is quadratic in \vec{I} , the target must be aligned rather than polarized—a preferential spin axis must exist rather than a direction. The FC is maximized by placing the target alignment axis in the x - z plane 45° off the z -direction defined by the incident neutron momentum (figure 1.1). The neutrons are polarized vertically (the y -direction.) The time reversed case for this transmission is illustrated (figure 1.2) where the “movie is run backward” (operator T)—and the spins are reversed in accordance with equation 1.2. This time reversed case, when viewed from a different direction (rotation operator R), is identical to the original scattering except that the neutron spin is flipped. Under TRI, the two transmissions proceed at the same rate. If the FC is present in the forward elastic scattering amplitude, however, the transmission rate will differ. If

$$f(0^\circ) = c_1 + c_2(\vec{s} \cdot \vec{I} \times \vec{k})(\vec{I} \cdot \vec{k}), \quad (1.4)$$

then reversing the neutron spin changes the sign of the second term (here c_1 and c_2 are complex constants.) The optical theorem relates the total cross section to the imaginary part of the amplitude,

$$\sigma_T = \frac{4\pi}{k} \text{Im} f(0^\circ), \quad (1.5)$$

thus the total cross section is different for \vec{s} parallel and antiparallel to $(\vec{I} \times \vec{k})(\vec{I} \cdot \vec{k})$:

$$\Delta\sigma_T = \frac{4\pi}{k} \text{Im}[f(0^\circ)^+ - f(0^\circ)^-] \propto |\vec{s} \cdot (\vec{I} \times \vec{k})(\vec{I} \cdot \vec{k})|. \quad (1.6)$$

This difference is manifested in the relative transmission rates for polarized neutrons through the target. More formally, all momenta change sign under the

$$\underline{T} \text{ (odd): } (\underline{I} \cdot \underline{k}) (\underline{I} \times \underline{k}) \cdot \underline{s}$$

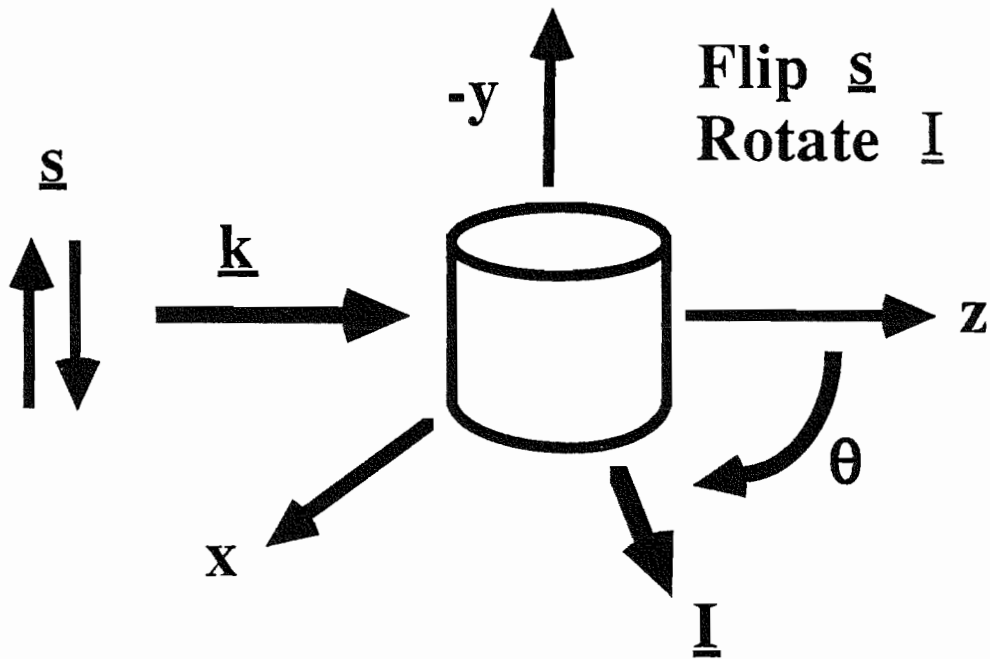


Figure 1.1: Geometry for the five-fold correlation.

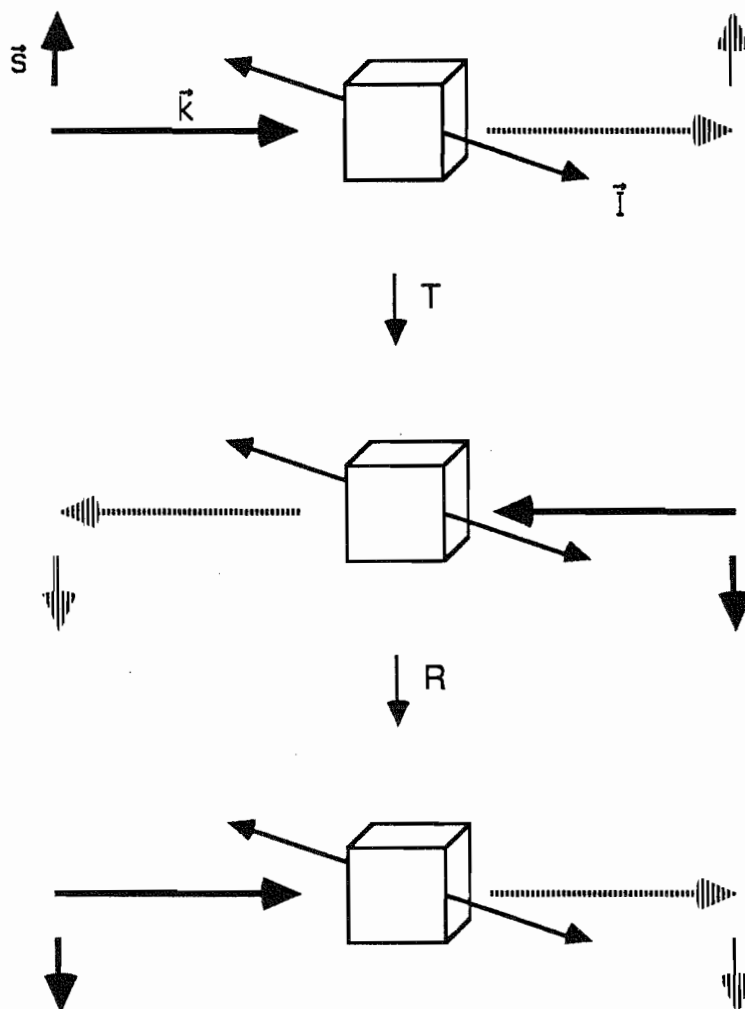


Figure 1.2: Transmission of polarized neutrons through an aligned target, and the time reversed scattering.

influence of the quantum mechanical time reversal operator. Thus the FC term in $f(0^\circ)$ changes sign whereby the form of $f(0^\circ)$ is different in the time reversed case.

Figure 1.2 implies the spin of the outgoing projectile is analyzed. Indeed the experiment must utilize a polarizer and an analyzer to be a true reciprocity—and hence TRI—test (Stodolsky 1986). The transmission asymmetry can be mimicked by two sequential T-conserving interactions. These are the helicity $(\vec{s} \cdot \vec{k})$ and the aligned target term $(\vec{s} \cdot \vec{I})(\vec{I} \cdot \vec{k})$. The real part of either amplitude precesses the neutron spin into the I - k plane, where the imaginary part of the other amplitude attenuates the beam preferentially with neutron spin. The analyzer permits rejection of such false-T-odd spin precessing events. Such an experiment is difficult to carry out because a polarized beam, an aligned target, and a polarimeter (i.e. double scattering) are needed, with the implication of technical complexity and low count rates.

In practice it is possible to carry out this test without analyzing the spin of the outgoing particle—as implied in figure 1.1—because the two T-even terms are P-odd and therefore small. If in addition the target alignment axis is rotated, a number of false asymmetry effects can be cancelled by searching only for the $\sin \theta \cos \theta$ or $\sin 2\theta$ dependence (figure 1.1) of the FC (Gould 1987). The potential false asymmetries are discussed more fully in chapter 6.

Another test of the reciprocity theorem is the comparison of the polarization P of particles scattered in an unpolarized beam and the analyzing power or asymmetry A obtained from the polarized beam (the time reversed case.) These so-called P - A tests measure the equality $P = A$ which is deduced from equation 1.1 (Bohr and Mottelson 1969). The P - A comparisons have been done for p - p scattering (Davis 1986), ^3He - p scattering (Trelle 1984), and n - p scattering (Bhatia 1982) in which all results are consistent with TRI. A similar type of test has also been proposed for neutron transmission (Kabir 1988a,b).

If incoherent sums are taken in the reciprocity theorem, the principle of “de-

tailed balance" is obtained. Equation 1.1 becomes

$$\sum_{m_\alpha m_\beta} |S_{\alpha\beta}|^2 = \sum_{m_\alpha m_\beta} |S_{\alpha_T\beta_T}|^2. \quad (1.7)$$

Detailed balance sometimes obtains, however, regardless of TRI as when the first-order Born approximation is a valid description for the S-matrix or when only two states are relevant for the S-matrix. The archetypal test of detailed balance involves the non-zero degree scattering of unpolarized nuclei. For nuclear scattering $A(a,b)B$, the "golden rule" of transitions rates

$$\frac{d\sigma_{\alpha\beta}}{d\Omega} = \frac{\pi\lambda_\alpha^2}{(2s_a + 1)(2s_A + 1)} \sum_{m_\alpha m_\beta} |S_{\alpha\beta}|^2 \quad (1.8)$$

and detailed balance lead to

$$\frac{(2s_a + 1)(2s_A + 1)\lambda_\beta^2}{(2s_b + 1)(2s_B + 1)\lambda_\alpha^2} \frac{d\sigma_{\alpha\beta}/d\Omega}{d\sigma_{\beta\alpha}/d\Omega} = 1. \quad (1.9)$$

Here s_i is the spin of particle i and λ_α^2 is the square of the relative wavelength in the incoming channel. The most precise tests of this type are for $^{27}\text{Al}(p,\alpha)^{24}\text{Mg}$ (Blanke 1983 and Driller 1979), both observing rates consistent with detailed balance. The 1979 measurement was performed at two compound nuclear (CN) resonances in ^{28}Si . An experimental asymmetry was formed from the relative reaction rates at the two resonance energies. The 1983 experiment was performed in the overlapping CN resonance regime. The relative reaction rates were compared at a minimum and a maximum. The experiments are difficult because the time reversed reaction must be matched in terms of center of mass energy and scattering angle. Being a detailed balance test, consistency with equation 1.9 does not imply directly TRI. For example, Blanke, et. al. had to argue that the relative phase between the reaction amplitude for TRI and the perturbing TRNI amplitude was not $\pi/2$, which would have caused a null result regardless of TRI. In addition, these tests lack sensitivity to spin-dependent TRNI.

Time reversal invariance has other consequences in addition to the reciprocity theorem. The relative phase of competing radiative transitions $E(L + 1)$ and

$M(L)$ is real (Lloyd 1951). The ratio of the transitions is

$$\delta = \frac{\langle I_f || E(L+1) || I_i \rangle}{\langle I_f || M(L) || I_i \rangle} = |\delta| e^{i\eta} \quad (1.10)$$

where the reduced matrix elements are taken between an initial state of spin I_i and a final state of spin I_f . Deviation of η from 0 or π implies TRNI and measurements are reported as $\sin \eta$. The statement of relative reality of phases is based, however, on a first-order perturbation approximation, which—while very good—ultimately necessitates higher order corrections that lead to a small phase difference ξ . These corrections correspond to so-called “final state interactions”, e.g., between the emitted photon and the atomic electron cloud (Boehm 1988). The transitions are measured for correlations among spin and momenta. Since these tests really determine $\sin(\eta + \xi)$, suppositions about the final state interactions must always be made in order to draw conclusions on TRNI. Indeed, the observation of non-zero $\sin(\eta + \xi)$ by Gimlett, et. al. (1981) is accounted for by $\sin \xi$.

We have reviewed several types of tests of TRI for which the quantities representing TRNI are quite varied: polarization-analyzing power comparisons, detailed balance in nuclear reactions, and relative phases of electromagnetic transition matrix elements. The relative precision for the respective observable for the most sensitive of each type of test is given in table 1.1. Also tabulated is the

Table 1.1: Precision of selected P-even T-odd experiments.

Type of Test	Observable	TRNI Bound
$P - A$	3×10^{-3}	$ P - A < 8.4 \times 10^{-3}$
detailed balance	5×10^{-3}	$\xi \leq 1.25 \times 10^{-3}$
γ correlations	4×10^{-4}	$ \sin \eta \leq 10^{-3}$
β decay	2×10^{-4}	$ D \leq 1.2 \times 10^{-3}$

measurement of a TRNI term in beta decay (of ^{19}Ne , Hallin, et. al. 1984). The

bound is on the strength D of the correlation $D\vec{I} \cdot (\vec{k}_e \times \vec{k}_\nu)/E_e E_\nu$ among the parent nuclear spin \vec{I} and the outgoing momenta of the electron and the neutrino, \vec{k}_e and \vec{k}_ν .

The real quantity of interest however, is the bound any test places on TRNI in the underlying effective nucleon-nucleon interaction. This issue has been investigated by French, et. al. (1987) for detailed balance tests via the concept of the spreading width Γ^T . It is defined as

$$\Gamma^T = 2\pi \langle H'^2 \rangle / d \quad (1.11)$$

where d is the mean spacing between energy levels in the compound nucleus and $\langle H'^2 \rangle$ is the mean of the squared elements of the TRI violating Hamiltonian H' . They have estimated how Γ^T arises for the compound nuclear matrix elements from a T-violating effective nucleon-nucleon interaction. The strength of the latter interaction relative to the TRI interaction is commonly denoted α_T , and they give

$$\alpha_T^2 \simeq \Gamma^T / \Gamma^{TRI} \simeq \Gamma^T / (2\pi 10^5 eV) \quad (1.12)$$

where $\Gamma^{TRI} \sim 1$ MeV is the TRI spreading width of the strong interaction. French, et. al. (1988) also applied Γ^T and α_T in an analysis of CN energy level and width fluctuations. More recently Harney, et. al. (1990) employed these in a reanalysis of the detailed balance tests, inferring a bound $\Gamma^T \leq 5.5 \times 10^{-2} eV$ and therefore $\alpha_T \leq 2.6 \times 10^{-4}$. (Harney, et. al. use the symbol F instead of α_T .)

A new P-even test of TRI should have a precision competitive with the values in table 1.1, and more importantly, good sensitivity to α_T . It should be as free as possible from ambiguities inherent in detailed balance tests or arising from final state interactions. Explicit spin-dependence is also desirable. Transmission of polarized neutrons is already a fertile system for the study of parity nonconservation (PNC, Bowman 1990a) because asymmetries in transmission can be measured to high precision. The small amount of PNC in nucleon-nucleon scattering is enhanced in the compound nuclear scattering of a neutron and a nucleus (see, for

example, Weidenmüller 1990) and compound nuclear enhancement is expected to occur for TRNI as well. Furthermore, transmission measurements test TRI independent of dynamical assumptions (Arash 1985), that is, final state interactions. For these reasons, the five-fold correlation is of particular interest.

No transmission experiments with polarized neutrons and aligned targets have been accomplished previously. In the present work we describe the construction and testing of a cryogenically aligned ^{165}Ho target, and a preliminary test of TRNI in the direct reaction energy regime using 2 MeV polarized neutrons. The target and its alignment and rotation are described in chapter two. The holmium nucleus is non-spherical, which gives rise to a large deformation effect cross-section. This deformation has been observed with stationary aligned targets, but never with a rotating target. The deformation effect experiment is described in chapter three, and calculations which reproduce the energy dependence of the effect are presented in chapter four. The apparatus relevant to the polarized neutron beam is described in chapter five and the FC experiment is discussed in chapter six. A summary and conclusions are given in chapter seven.

Chapter 2

EXPERIMENTAL APPARATUS

2.1 NUCLEAR ORIENTATION

An oriented nuclear system is one in which the populations $p(m)$ of magnetic substates m of the nuclei are unequal. The system is aligned if $p(m) = p(-m)$ and polarized if $p(m) \neq p(-m)$. These situations are illustrated schematically in figure 2.1. The quantization axis to which these substates refer is often provided by a magnetic field B which interacts with the nuclear magnetic dipole moment μ , related to the spin \vec{I} of the nucleus by $\vec{\mu} = g\mu_N\vec{I}$. Here g is the gyromagnetic ratio of the nuclei and μ_N the nuclear magneton. The static magnetic field lifts the energy degeneracy among the magnetic substates; the energy splitting is

$$E_m = -\vec{\mu} \cdot \vec{B} = -m\mu B. \quad (2.1)$$

For a system in thermal equilibrium, the "population parameters" $p(m)$ follow a Boltzmann distribution,

$$p(m) = e^{-E_m/kT}. \quad (2.2)$$

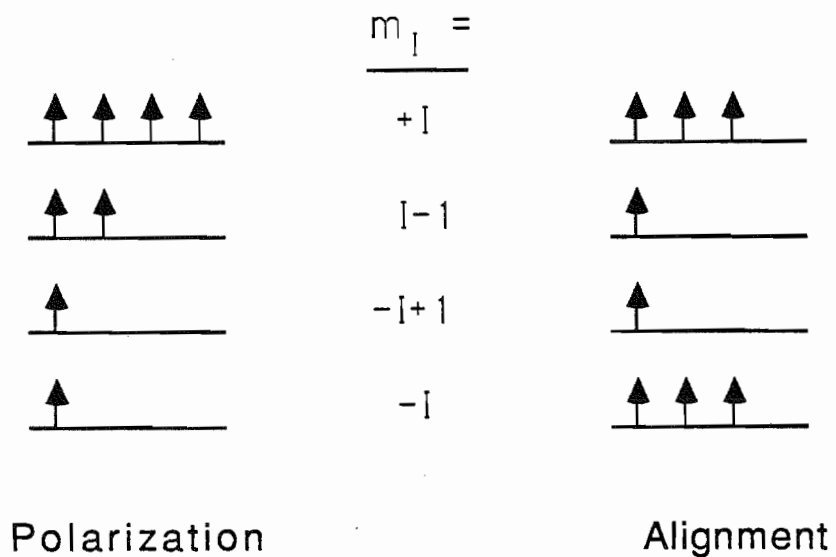


Figure 2.1: Nuclear Orientation. The occupation of each magnetic substate m is represented by the number of arrows.

Hence to achieve appreciably different occupations of sublevels, the energy splitting must be comparable to the thermal energy kT , requiring a very large magnetic field and a very low temperature. This method of orienting nuclei is termed “Brute Force Orientation” and is the method used at TUNL’s Cryogenic Polarized Target Facility (CPTF). The target is placed in a large (~ 7 tesla) magnetic field (provided by a superconducting magnet) at a temperature typically tens of millikelvin. In the limit $T \rightarrow 0$, the spins attain the lowest energy state $|m| = I$. Orientation can be described by the parameters f_1 and f_2 (Tolhoek 1953 or DeGroot 1965). Polarization is defined by f_1 :

$$f_1 = \langle m \rangle / I \quad (2.3)$$

where $\langle m \rangle$ is the expectation value:

$$\langle m \rangle = \sum_{m=-I}^I m p(m) / \sum_{m=-I}^I p(m). \quad (2.4)$$

For the alignment depicted in figure 2.1, f_1 equals zero and f_2 is defined by

$$f_2 = [\langle m^2 \rangle - I(I+1)/3] / I^2. \quad (2.5)$$

For an unoriented target $f_1 = f_2 = 0$. This set of orientation parameters can of course be extended to higher orders f_K —alignment refers to non-zero f_K for only K even while polarization refers to the general case of non-zero f_K . An excellent reference for brute force orientation is Stone and Postma (1986).

The f_K are widely favored by the low temperature physics community, but an alternate set of parameters, the statistical tensors $t_{KQ}(I)$ is used to describe the orientation of the TUNL holmium target. Statistical tensors are used by Barabanov (1987) and Hnizdo and Kemper (1986) and have very simple rotation properties. The use of a target whose spin direction is frequently changed therefore makes tensor formalism more attractive. The t_{KQ} are proportional to elements of the density matrix for the spin system. A general quantum mechanical state is defined as

$$|\Psi\rangle = \sum_m a_m |m\rangle$$

$$= \sum_m \langle m | \Psi \rangle | m \rangle, \quad (2.6)$$

where $|m\rangle$ is the basis set of substates of the system hamiltonian. The ensemble of nuclei is then described by the density matrix ρ with elements

$$\rho_{mm'} = a_m a_{m'}^*. \quad (2.7)$$

An equivalent description is afforded by the irreducible statistical tensors of rank K , $0 \leq K \leq 2I$, defined by

$$t_{KQ} = \hat{I} \sum_{mm'} (-1)^{I-m} \langle Im'I - m | KQ \rangle \rho_{mm'}, \quad -K \leq Q \leq K, \quad (2.8)$$

where $\hat{I} = \sqrt{2I+1}$. We are interested in a description of this ensemble after an arbitrary rotation. We use the rotation matrices of Brink and Satchler (1962):

$$D_{mm'}^j(\alpha\beta\gamma) = \langle jm | e^{-i\alpha J_z} e^{-i\beta J_y} e^{-i\gamma J_z} | jm' \rangle \quad (2.9)$$

$$= e^{-i\alpha m} d_{mm'}^j(\beta) e^{-i\gamma m'} \quad (2.10)$$

with Euler angles $(\alpha\beta\gamma)$ and angular momentum operator J . When the state is rotated, the statistical tensors transform as

$$t'_{KQ} = \sum_{Q'} D_{Q'Q}^K(\alpha\beta\gamma)^* t_{KQ'} \quad (2.11)$$

with the same frame used to describe the rotated (primed) and unrotated (unprimed) states. The rank K of the irreducible tensors is preserved under rotation. The convention here is that of Simonius (1974). In the case of an axially symmetric spin system, the tensors reduce to t_{K0} , which equals the B_K of Blin-Stoyle and Grace (1957) and equals $(-)^K B_K$ of Krane (1973). Both B_K thus defined are also referred to as statistical tensors, and have been used with mixed phase conventions (see Krane 1973). The relation between the t_{K0} and the f_K is

$$t_{K0}(I) = I^K \hat{K} \hat{I} \sqrt{\frac{(2I-K)!}{(2I+K+1)!}} \left(\frac{(K!)^2}{(2K)!} \right)^{1/2} f_K \quad (2.12)$$

Explicit use of t_{KQ} will be made later for the description of the holmium target.

2.2 HOLMIUM SPIN STRUCTURE

Holmium is a metallic rare earth, with unusual magnetic properties. Below 132 K it is a ferromagnet, but at 20 K it becomes antiferromagnetic (Koehler 1966). The atomic spins form a spiral staircase structure along the *c*-axis of the hexagonal close-packed (hcp) holmium crystal. Each basal or *a*-*b* plane consists of nuclei whose spins are parallel, directed 10° out of the plane but otherwise along an *a*- or *b*-axis. Successive planes have net spin rotated 30° about the *c*-axis. This structure is depicted in figure 2.2. In a magnetically saturated sample the domains are aligned; mirror domains in a crystal with no magnetic history cancel the polarization otherwise present along the *c*-axis, but alignment with respect to this axis remains. Because of the unpaired $4f$ electrons, holmium has one of the largest effective hyperfine fields—on order of 740 Tesla—of all the elements. The hyperfine interaction orients the nuclei similar to an external BFO magnetic field. Because of the magnitude of the interaction, the nuclear magnetic substate energy splitting becomes comparable to the thermal energy even at hundreds of millikelvins. For any one *a*-*b* plane this spontaneous alignment of the nuclei is plotted in figure 2.3 as a function of temperature. The temperature dependence is calculated using an effective hamiltonian whose eigenvalues are parametrized empirically by A and P in

$$E_m/k = mA + P\left[m^2 - \frac{1}{3}I(I+1)\right] \quad (2.13)$$

with $A = 0.319 \pm 0.003K$ and $P = 0.004 \pm 0.001K$ (Krusius 1969). The graph illustrates that by 100 mK, 96% of the maximum achievable alignment has been reached. It is also relatively easy to polarize holmium, as both the *a*- and *b*- axes are easy directions of magnetization (Strandburg 1962). Only a small external field is necessary to polarize the electrons. The orientation is imparted to the nuclei by the hyperfine interaction.

The alignment with respect to the crystalline *c*-axis is obtained from the alignment within each plane and the conic spin structure. The ground state of the ^{165}Ho

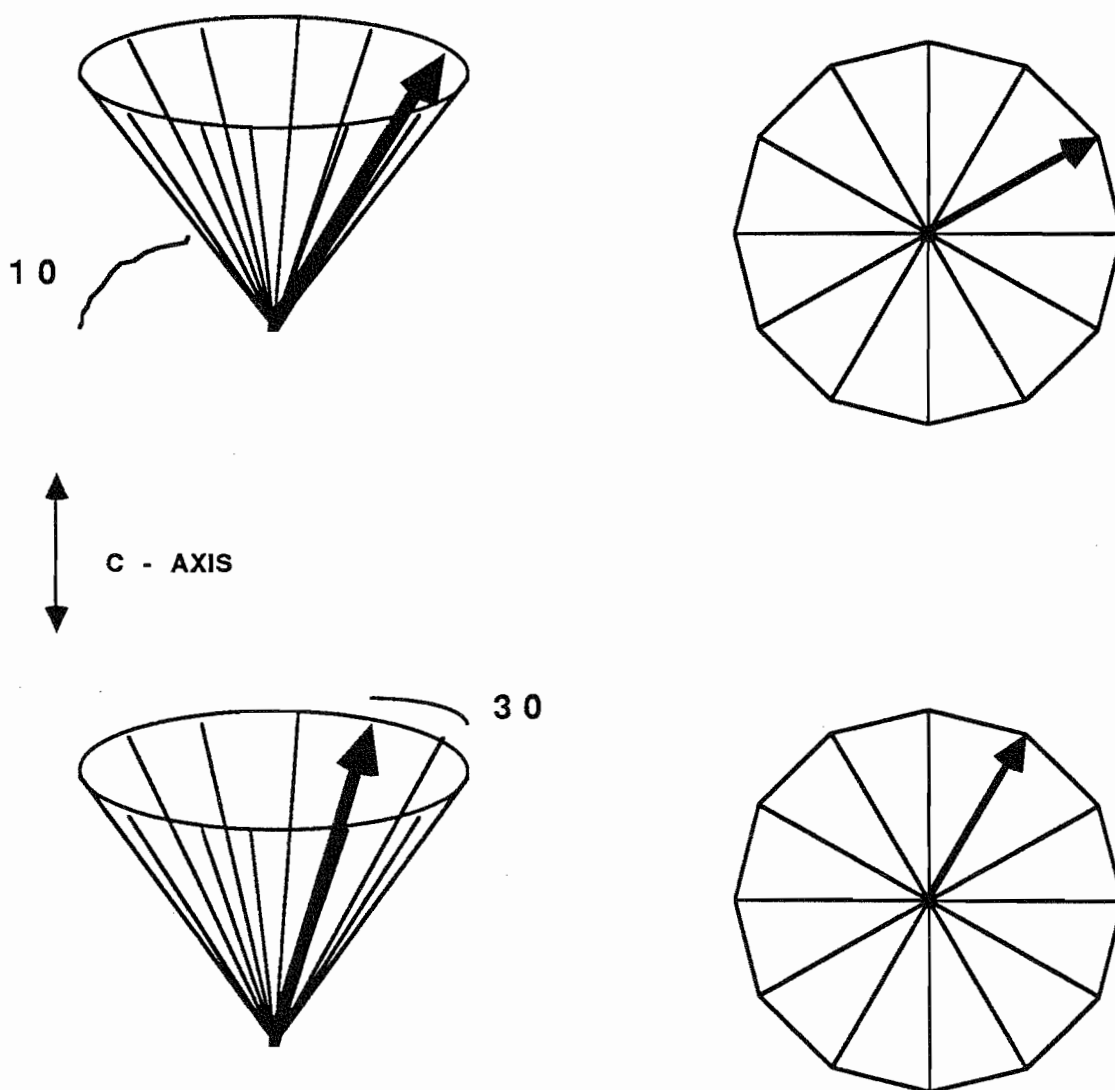


Figure 2.2: Nuclear spins in a holmium single crystal. The 3-D view of the net spin of a basal plane is shown on the left. The corresponding projection of the spin in the basal plane is drawn on the right.

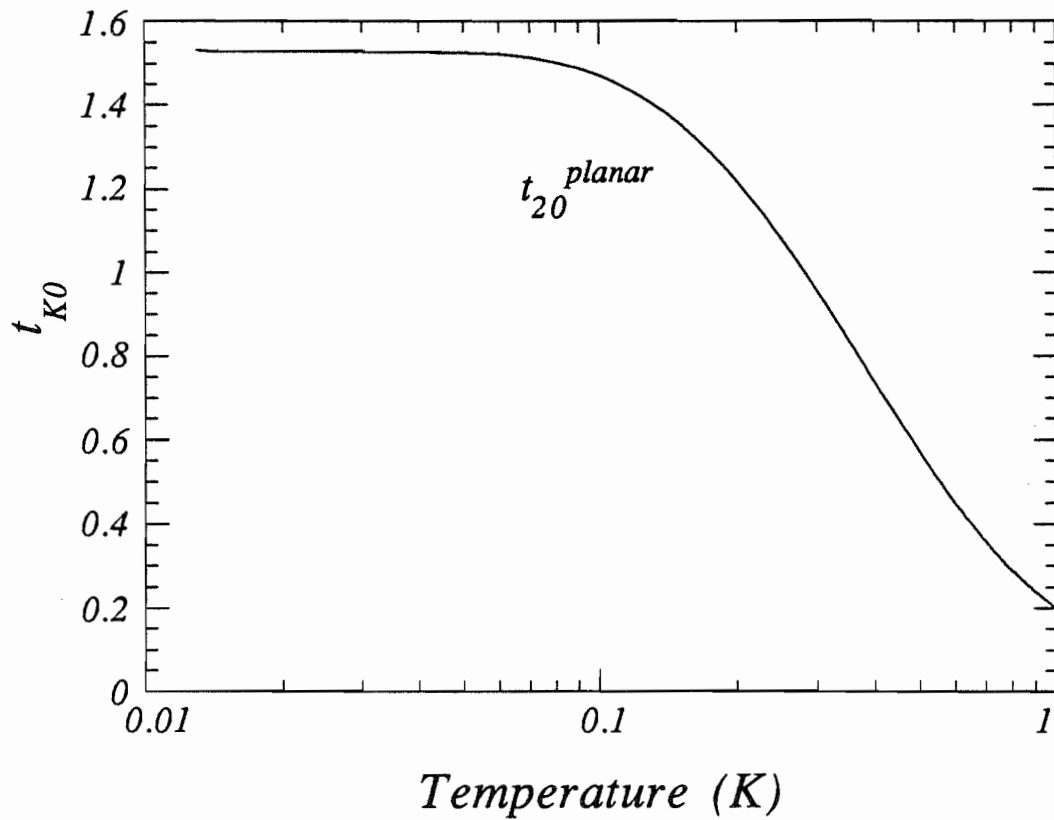


Figure 2.3: Alignment of holmium nuclei in the basal plane as a function of temperature.

nucleus is spin $I = 7/2$, hence an ensemble of nuclei can be described with non-zero statistical tensors up to rank $2I + 1 = 8$. The ensemble comprising one basal plane is assigned t_{KQ}^{planar} to describe the extent that the nuclei collectively parallel the local effective magnetic field. Since this subsystem possesses cylindrical symmetry, $t_{KQ}^{planar} = t_{K0}^{planar} \delta_{Q0}$ where δ_{Q0} is the Dirac delta function. We are interested in alignment, i.e. $K = 2$. In the limit of zero temperature, t_{20}^{planar} obtains its maximum value

$$[t_{20}^{planar}(I)]_{max} = (2I)! \sqrt{\frac{5(2I+1)}{(2I-2)!(2I+3)!}} \quad (2.14)$$

or

$$[t_{20}^{planar}(7/2)]_{max} = \sqrt{7/3} \doteq 1.5275. \quad (2.15)$$

(Note that our normalization of t_{KQ} means that only t_{00} has a maximum equal to 1, unlike some other orientation parameters such as Alfimenkov, 1973.) As in figure 2.2 a single crystal is axially symmetric about the c-axis. Therefore there is an alignment \hat{t}_{20} with respect to the c-axis, determined by rotating the various t_{20}^{planar} as in equation 2.11

$$\hat{t}_{20} = d_{00}^2(80^\circ) t_{20}^{planar} = P_2(\cos 80^\circ) t_{20}^{planar}, \quad (2.16)$$

where 80° is the angle between each net basal plane spin and the c-axis and $P_2(\cos\beta)$ is a Legendre polynomial. Equation 2.16 holds regardless of the particular directions of a and b within the basal plane. (In fact, the topic of the exact turn angle and whether any phenomena such as spin-slip or stacking faults are present in the spin structure of holmium is currently under study. See, for example, Cowley 1988 or Stewart 1989.) The alternate method of deriving equation 2.16, involving averages directly over the orientation parameters B_K (Marshak and Turrell, 1979) yields the same result. In the experiments we ultimately need the alignment t_{20} with respect to the beam direction— \hat{t}_{20} representing the whole single crystal ensemble can be rotated into this with equation 2.11. However, the beam direction is not necessarily an axis of symmetry, so t_{2Q} can be non-zero for Q non-zero—indeed some of these will be of interest later.

2.3 ROTATING TARGET REFRIGERATOR

In this section we discuss the refrigerator required to align the holmium target, and the rotation system used to rotate the target. These are among the most complicated components in the experiments and, not surprisingly, required the most time and effort to construct.

2.3.1 DILUTION REFRIGERATOR CRYOSTAT

The purpose of the refrigerator is to cool a single crystal of holmium to near 100 mK, to achieve near maximum alignment of the nuclear spins. The cooling power has to be sufficient to cool the large target necessary for a neutron counting experiment and to remove any heat dumped in the target by the neutron beam (although for the present beams of several MeV in energy and $8\text{k neutrons s}^{-1}\text{cm}^{-2}$ in intensity, this heating is only of order 10 nW.) The cooling has to be continuous over several days to enable counting enough neutrons.

Dilution refrigerators—the workhorses of online nuclear orientation experiments everywhere—are well suited to these requirements. Their operation depends on the phase separation that occurs at several hundred millikelvin in a mixture of ^3He – ^4He . The lighter fluid, or “concentrated layer”, is virtually 100% ^3He ; the “dilute” layer is 94% ^4He + 6% ^3He . The concentration of ^3He in the dilute side is essentially reached by 40 mK and remains even in the limit of zero temperature. Below about one-half a Kelvin, ^4He is a Bose condensate—it has collapsed to its ground state and is a thermally inert superfluid. The spin $1/2$ ^3He atoms below this temperature behave like a weakly interacting Fermi gas. The cooling occurs in a dilution refrigerator (DR) when the ^3He atoms diffuse down across the phase boundary from the concentrated to the dilute layer. The Fermi gas expands into the inert ^4He superfluid analogous to the expansion of liquid refrigerant into a vapor phase. The process is made continuous by pumping the ^3He out of the dilute side and injecting it back into the concentrated side. Little

^4He is pumped off since even up to 900 mK the vapor pressure of ^4He is far less than that of ^3He . Thus the dilute side ends at a liquid-vacuum interface in the "still" of the DR which is pumped on by a sealed, room temperature vacuum pump. These components are shown in figure 2.4, which is a schematic of the DR used.

Another element in the DR as illustrated in figure 2.4 is the coldplate or ^4He pot (DeLong 1971). Pumping a reservoir of liquid ^4He provides cooling from 4.2 K to around 1.3 K, below the condensation temperature 3.2 K of ^3He . Thus ^3He is returned to the cryostat and liquefied through another reservoir (the condensor) which is in good thermal contact with the coldplate. The coldplate is replenished with liquid continuously by a very small leak (or flow impedance) from the ^4He bath. The other components shown are heat exchangers, which provide pre-cooling of the hot concentrated side through thermal contact with the cold dilute side. A good discussion of the properties of ^3He and ^4He at low temperatures is found in McClintock (1984); dilution refrigerators are treated in Lounasmaa (1974) and Anderson (1970), with quantitative discussion by Wheatley (1968).

The rotating target cryostat at TUNL's CPTF is similar to an S.H.E. Model DRI-430 commercial DR. It was fabricated at the machine shops of NCSU and Duke U. and assembled at the Low Temperature Laboratory at NCSU. The cryostat is housed in a custom designed ^4He dewar (Janis Research) with a 28 liter LN_2 jacket. The dewar capacity is 22 liters of ^4He in the belly above the vacuum can, permitting 60 hrs between liquid helium transfers. The dewar has a demountable tail section that extends into the neutron beam path consisting of a 4" *OD*, 1/16" wall aluminum outer tail, a 1/32" wall aluminum 77 K shield, and a 2 $\frac{1}{4}$ " *OD*, 0.025" wall stainless steel dewar tail. The vacuum can enclosing the DR within the dewar is also stainless steel, with a 2.00" *OD*, 0.035" tail. The 4 K seals are effected with indium o-rings (Lim 1986). The copper coldplate is continuously filled through a 0.004" *ID* tube (having a flow impedance of about $2.5 \times 10^{11} \text{ cm}^{-3}$) from the liquid helium dewar, and is pumped on by a Welch 1397

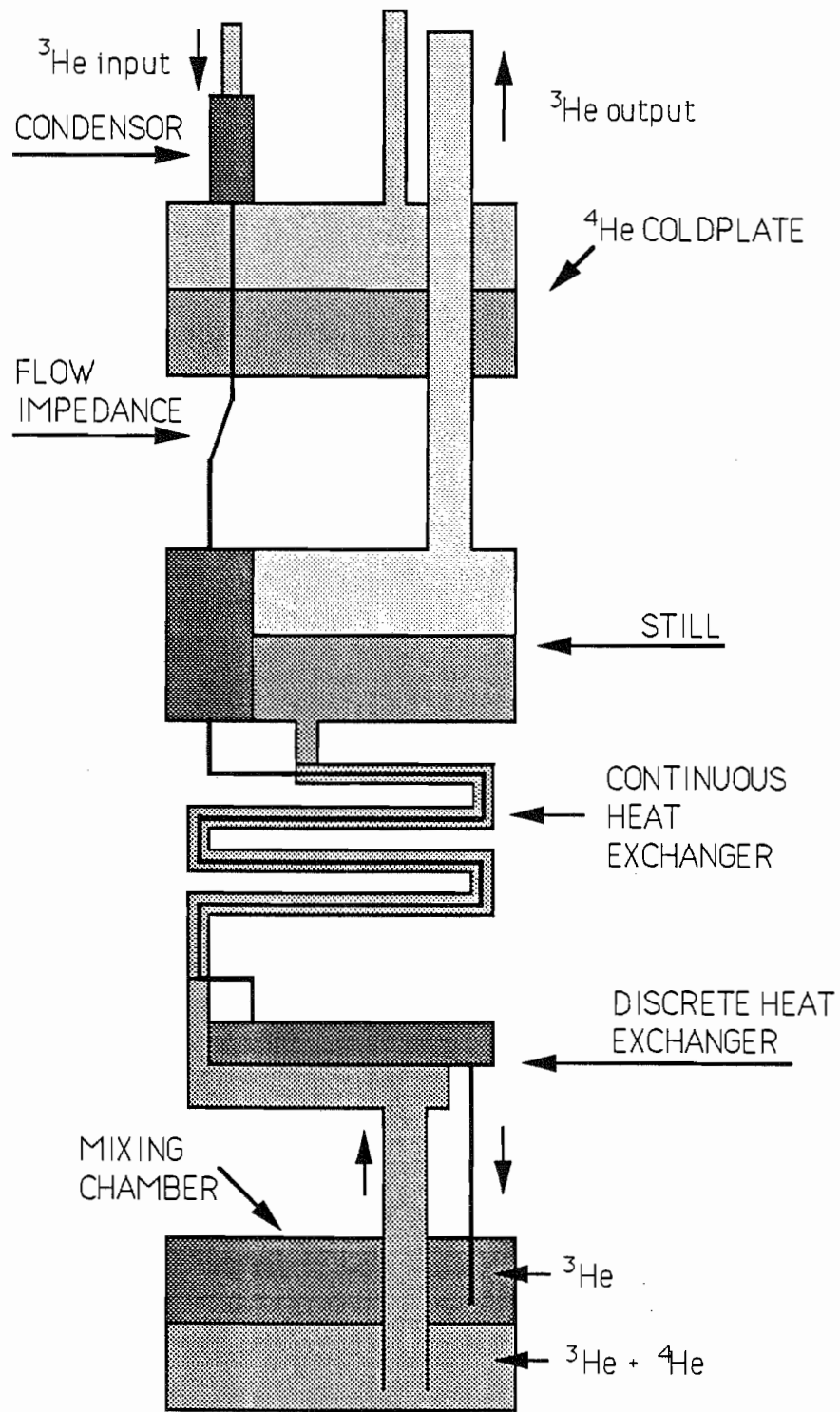


Figure 2.4: Dilution Refrigerator.

mechanical pump at room temperature. Heating tests on the coldplate yielded a cooling capacity of greater than 30 milliwatts. The condenser is a copper cylinder with brass endcap, clamped onto the coldplate by a nut and threaded tail. Its volume when empty was 6 cm^3 , but it is filled with 18 disks punched from copper felt (Energy Conservation Systems FM1005), then pressed into the condenser. Normal condensation pressure is 6–10 inches Hg absolute. The cap and connections are soldered with solid wire 50/50 lead-tin solder and ZnCl flux. Placed upstream of the condenser in the ^3He return line is a precooler, similar in design but with a 19 cm^3 volume, which resides outside the vacuum can in the liquid helium bath at 4 K. The concentrated side is heat-sunk at the still by being wound around and soldered to it. There is a flow impedance both upstream and downstream of this still exchanger which raises the condensation pressure to aid in liquefaction. These are simply suitable lengths of 0.004" *ID* tube (Smith 1988). Their total impedance was measured (Fagaly and Bohn 1976) to be $7.37 \times 10^{12} \text{ cm}^{-3}$ —a third of which was below the still. The copper still is annular, with a volume of 40.6 cm^3 and thus a capacity of L^4He equivalent to $28\frac{1}{2}$ liters of gas at STP. Two heat exchangers are downstream of the still on the concentrated side. The first is a continuous exchanger similar to the design of Frossati (1977). A 2 meter length of copper-nickel tube, 0.16 *cm* diameter, was flattened and wound in a spiral, then inserted in a 0.48 *cm OD* stainless steel tube which itself had been wound in a spiral. The inner spiral contains the concentrated flow; the outer, the dilute. The lower heat exchanger is the discrete type (Rosenbaum and Breuer 1981), with a semicircular copper body. The copper mixing chamber is annular, with a volume of 10.7 cm^3 when empty. However, the interiors of the mixing chamber and the discrete exchanger are plated with silver and packed with 0.5–0.8 μ silver powder. The maximum total volume of all these components except the precooler is estimated for ^3He to be 14.1 cm^3 or $8\frac{1}{2} \text{ l}$ gas at STP; for ^4He , 65.0 cm^3 or 49 l gas at STP. The components are separated by 0.010" wall stainless steel struts, and have numerous tapped holes for thermometers, heaters, and other instruments.

The gas handling system is of conventional design, illustrated in figure 2.5, employing a 4 inch oil diffusion pump backed by a 660 l/min sealed mechanical pump to recirculate the ^3He mixture. The cryostat is run with 30 l of ^4He and 8 l of ^3He , a mixture which optimizes the level of the phase separation in the mixing chamber. In this configuration—without the holmium target mounted—the mixing chamber reached a base temperature of 42 mK and had a cooling power of $85 \mu\text{W}$ at 110 mK, with the recirculating flow rate at $120 \mu\text{moles/sec}$. Typically, 3.4 mW of heat is applied to the still, keeping its temperature around 640 mK. The flow rate as a function of still heating is plotted in figure 2.6.

2.3.2 ROTATION SYSTEM

The novel feature of the cryostat is the central access which allows a rotating axle to pass from room temperature above the refrigerator to the cryogenic holmium target below the mixing chamber. The rotation system is illustrated in figure 2.7. Starting from the top, the rotation drive consists of a computer controlled Vexta stepping motor (2 phase, PH266M-E1.2) with a 25 : 1 Berg antibacklash step-down gearbox (servogear, SX-B4-14.) The shaft angle is monitored by a 13 bit absolute angle encoder (BEI Motion Systems, M25) providing angular control of the upper end of the axle to $\pm 0.04^\circ$. This rotation drive system is coupled into the cryostat vacuum with a commercial rotation seal (Ferrofluidics MB-188-L-N-090) and flexible couplers. An outer central shaft of 0.50" OD, 0.035" wall stainless steel extends from below the rotation seal to the vacuum can. The axle continues through this 45 inches to a level between the vacuum can top flange and the coldplate. This axle is mostly 3/8" OD, 0.030" wall stainless steel, interrupted by three solid copper couplers, 0.44" OD. The copper couplers block radiation down both the axle and the outer shaft, rubbing against the latter within the helium bath and also at the level of the vacuum can flange. Another flexible bellows coupler connects that axle to a 3/16" OD, 0.010" wall stainless steel shaft which continues 14 inches to below the mixing chamber. At that point the axle

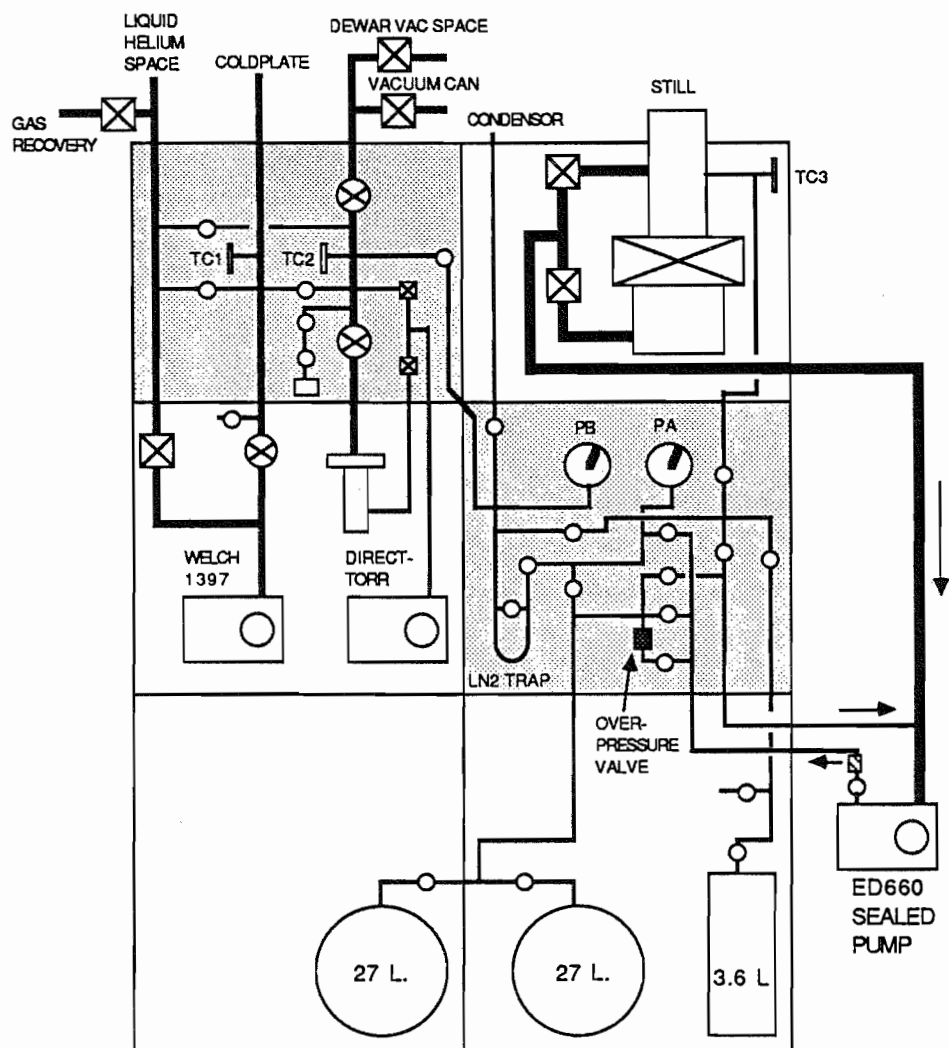


Figure 2.5: Dilution refrigerator gas handling system

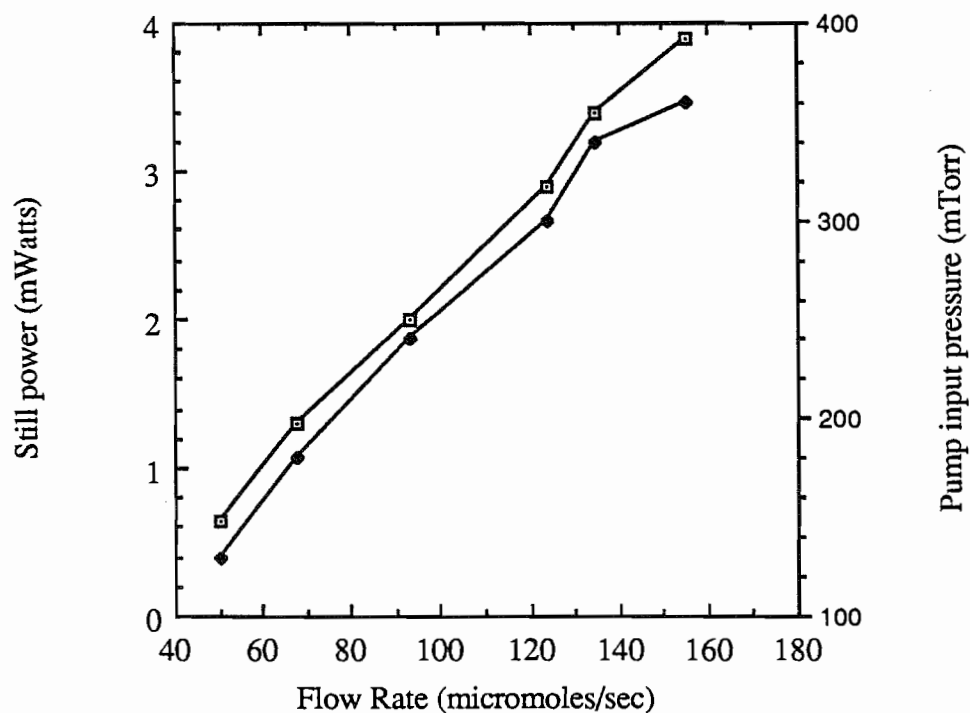


Figure 2.6: Helium flow rate as a function of still heating. The squares represent the flow rate for a given heating of the still. The diamonds represent corresponding pressure at the input to the mechanical pump.

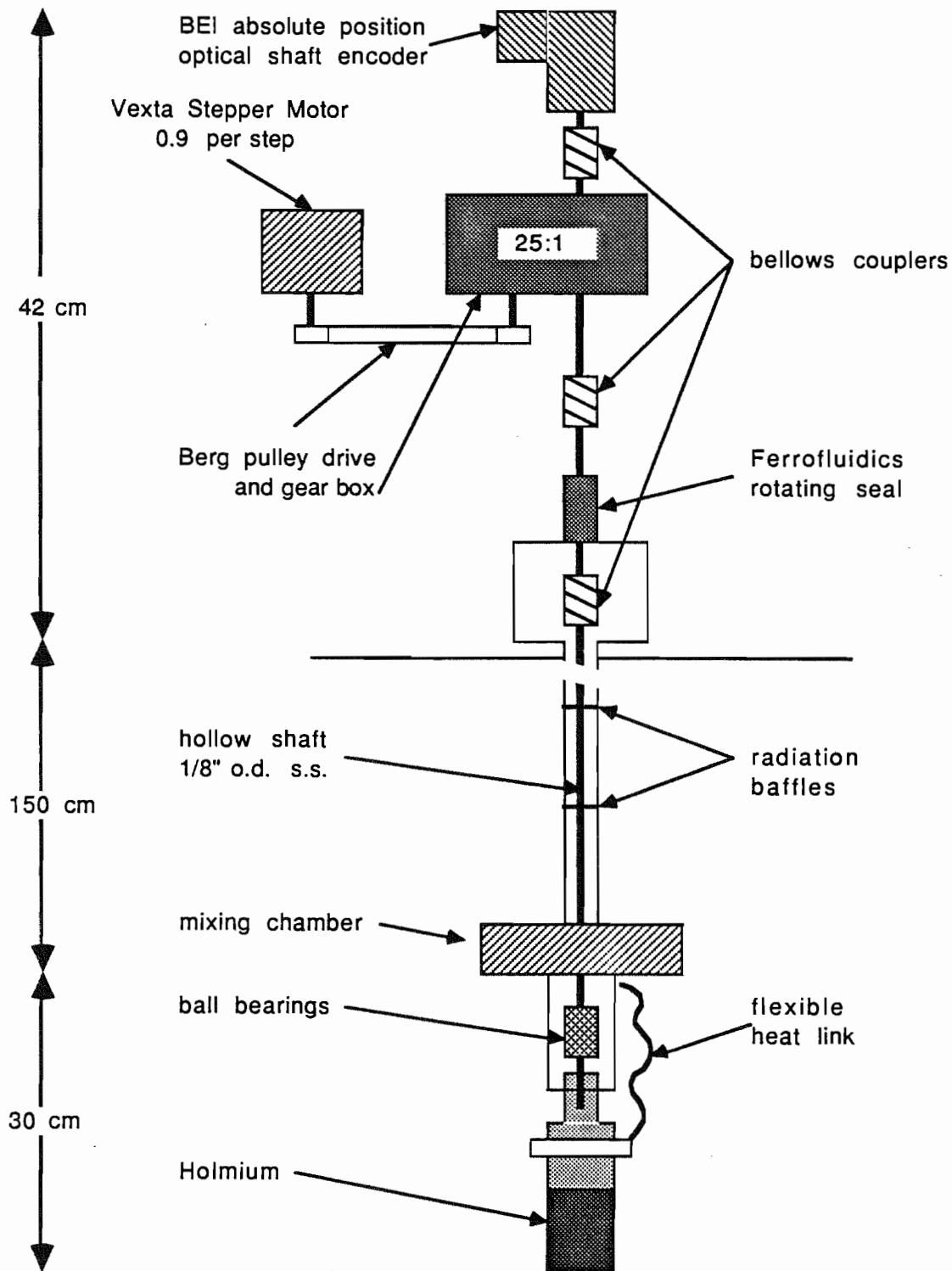


Figure 2.7: Rotation system.

is coupled to two greaseless precision bearings (Berg B2-11-U) which are on a copper boss bolted to the mixing chamber. These bearings maintain rotational alignment and stability. To the very end of the rotating axle is connected a hollow copper coldfinger, 0.85" *OD*, on which the cylindrical holmium target is soldered. Flexible copper links are utilized at three places within the vacuum can to thermally anchor the axle and target directly to the DR. These links were fabricated from the untinned copper shielding in coaxial cable of appropriate diameter. The shielding was flattened, its ends silver-soldered to copper tabs which were then screwed to the components to be linked. Two links were 3/8" wide and 2" long—one connecting the bottom of the 3/8" axle to the vacuum can flange and the other connecting the top of the 3/16" axle to the coldplate. The design temperatures at those respective points on the rotating axle were 4.7 K and 1.25 K. The temperature measured at the lower point during operation was in fact 1.5 K; this heat load through the lower link to the coldplate had no noticeable effect on the coldplate temperature nor on the liquid helium boil-off rate. Furthermore, the heat load this presented down the axle to the mixing chamber was calculated to be $0.8 \mu W$.

The final element in the rotation system is the third flexible link, which provided primary cooling of the holmium target. This link was constructed like the other two, but 4" long and only 3/16" wide. Moreover, three shielding braids are stacked, tripling the thickness. Each braid consists of 100 strands of 6.2 *mil* diameter (roughly #36 gauge) copper. The link is bolted to the mixing chamber boss and to a collar on the copper coldfinger. The cooling power of this link at 100 mK was calculated to be $\dot{Q}/\Delta T \approx 580 \mu W/K$. By applying a known amount of heat to the coldfinger and observing its temperature rise, this thermal conductivity was determined to be around $620 \mu W/K$ at 200 mK. Thus the link performs as expected. The link is kept close to the center axis (away from the 4 K sides of the vacuum can) with a stiff but poorly conductive computer punch card wrapped around the coldfinger collar. Altogether these links permit rotation of the target

through a 270° arc.

The end of the holmium cylinder was machined with an inset to align it to the center of the finger to within ± 15 microns. This also provided a cleaned surface for thermal contact, since holmium oxide is a barrier of poor thermal conductivity. To further reduce the oxide, the target was cleaned with acetone and then chemically polished (Roman 1965) under a helium atmosphere, followed by an ethyl alcohol rinse. Still under helium, the end surface was etched and rinsed, leaving it shiny. The target was immediately warmed on a hotplate to nominally 140° and tinned with Cd-Bi solder (Steyert 1967). The coldfinger end was also tinned, then joined to the holmium—heat being applied to the former. The assembly was rewarmed twice in order to straighten the joint. In case the solder joint failed after thermal cycling, a 0.025 mm thick copper foil was epoxied around the joint, extending $1/8$ " down the side of the holmium cylinder.

Several tests of the rotation system were performed at room temperature. The target returned to its original angular orientation to within $\pm 1/2^\circ$ after repeated rotations. The radial vibration of the target during rotation was about 0.024 "; when not rotating this reduced to 0.0001 ". The torque required to turn the target was measured to be about 5×10^{-2} $N \cdot m$ without the thermal links in place. This torque would produce at worst a 0.5° twist in the tubes connecting the target to room temperature and generate 40 mJ of heat at the contact points while rotating the target 45° . Indeed, this kind of torsional flexing (Roark 1954) was considered in the design of the rotating shaft. The thickness providing torsional stiffness was compromised by the thinness minimizing thermal conduction from room temperature.

2.3.3 HOLMIUM TARGET

The holmium target was a cylindrical single crystal, 99.8% holmium, 2.29 cm in diameter and 2.8 cm long, 101.6 g or 0.62 gram-moles of ^{165}Ho . It was grown by Ames Laboratory (Materials Preparation Center at Iowa State University) and

cut so that the c-axis was oriented radially. Its thickness was measured with a micrometer on five different axes at each of three different locations along the length of the cylinder, yielding a mean thickness 2.2887 cm and a relative deviation from circularity of less than 4 parts in 10,000. Thus the difference in transmission through this target due to different average thickness when the target was rotated was no more than 1×10^{-4} .

The nuclear heat capacity of the target is 4.25 J/K at 0.3 K and necessitates removing 2.3 J of heat to cool from 1 K to 0.3 K. The limitation in cooling the target is due largely to the thermal link and can be understood as follows. If T_{Ho} and T_{mc} are defined as the temperatures of the holmium and mixing chamber respectively then the heat flow to the mixing chamber is

$$\dot{Q} = \kappa(T_{Ho} - T_{mc}). \quad (2.17)$$

The conductance κ is a linear function of temperature

$$\kappa = (\lambda A/l)T \quad (2.18)$$

where A/l is the ratio of area to length of the link and $\lambda \sim 100 \text{ W/m} \cdot \text{K}$ for copper. Therefore

$$\dot{Q} = \lambda \frac{A}{l} \frac{T_{Ho} + T_{mc}}{2} (T_{Ho} - T_{mc}). \quad (2.19)$$

This heat must be removed by the ^3He circulation

$$\dot{Q}_{mc} = RT_{mc}^2 \quad (2.20)$$

where $R \approx 84\dot{n} \sim 6 \text{ mW/K}^2$ for this refrigerator (\dot{n} is the molar flow rate of the circulating ^3He .) Since $\dot{Q} = \dot{Q}_{mc}$ when the mixing chamber is in equilibrium, equations 2.19 and 2.20 can be solved for T_{mc}^2 which is then substituted into 2.19 to get cooling in terms of the holmium temperature

$$\dot{Q} = \frac{R}{1 + \frac{R}{\lambda A/l}} T_{Ho}^2 \quad (2.21)$$

Thus the effective cooling coefficient of the DR has been reduced to

$$R_{eff} = \frac{R}{1 + \frac{R}{\lambda A/2l}}. \quad (2.22)$$

For this link $(\lambda A/2l)$ is about 3 mW/K and so $R_{eff} \sim 2 \text{ mW/K}^2 = \frac{1}{3}R$. Because of this reduction, it takes three times longer to cool the holmium to the same base temperature compared to having the holmium bolted directly to the mixing chamber. Alternatively, to reach the same equilibrium holmium temperature only a third of any external heat leak can be tolerated.

2.3.4 THERMOMETRY

The operating temperatures of all the components in the rotating target cryostat are monitored with Speer 470Ω and 220Ω (Black 1964) and Dale $1K\Omega$ (Li 1986) resistors. Additionally, a calibrated germanium resistance thermometer (LakeShore Cryotronics GR-200A-50) was mounted on the mixing chamber. Most of the other resistors had been calibrated against this and/or against a CMN magnetic susceptibility thermometer or a superconducting fixed point device during trial runs of the cryostat. Indeed the cryostat was used to study home-built fixed point devices (Koster 1989). These methods of thermometry are reviewed in Anderson (1980). The liquid helium level in the dewar was monitored also with carbon resistors, as well as with a $L^4\text{He}$ level sensor (AMI Model 100).

Two resistors are mounted directly on the bottom of the holmium. These are the means by which we determine the degree of alignment. Care was therefore required in mounting the resistors, especially since holmium oxide might again present a thermal barrier. Thus the bottom surface was rubbed with crocus cloth and rinsed with acetone. A Speer 220Ω was epoxied to a copper foil tab and a Dale $1K\Omega$ was epoxied onto both. Hg-In solder (Krusius 1969) was used to attach this assembly to the holmium; another copper foil was epoxied over this mounting to provide bonding at room temperature. The conductance of one of

these thermometers was recorded at 15 minute intervals during one cooldown of the cryostat, yielding the cooling curve shown in figure 2.8. With the holmium approaching a temperature of around 270 mK, the temperature of the mixing chamber was normally approximately 100 mK. This behavior is consistent with a heat leak to the sample of $50\mu\text{W}$, of undetermined origin. A test of the cooling capacity of the mixing chamber produced the plot in figure 2.9. Measured values are shown as squares. The dotted line shows the theoretical best performance of a mixing chamber (Lounasmaa 1974) given by equation 2.20. The cooling power has the appropriate T^2 temperature dependence, but again with an additional heat input of tens of microwatts. Moreover, a similar pair of resistors mounted on the coldfinger indicated a temperature much closer to that of the holmium than of the mixing chamber. The behavior of the cryostat is therefore consistent with an acceptable thermal connection of holmium to coldfinger but an external heat input to the lowest temperature components—aside from the reduced cooling power on the holmium due to the coldfinger-mixing chamber thermal connection discussed in section 2.3.3.

2.3.5 ELECTRONICS

The electronics for the rotating target cryostat consists of two sets—that for the DR (chiefly thermometric) and that for microcomputer control of the target rotation. The former set employs shielded, twisted-pair wiring from a potentiometric conductance bridge (S.H.E.) at room temperature to a bread-board terminal strip inside the vacuum can. Constantan wiring is used throughout the vacuum can for its small thermal conductivity. The germanium thermometer uses four leads. An ohmmeter measures the resistance of the carbon level sensors while the level meter is used for the superconducting level sensor. The heaters are operated with a locally constructed power supply.

The latter set of electronics consists of the stepping motor, shaft encoder, and a Texas Instruments (TI) Model 525 Programmable Controller with Model 505

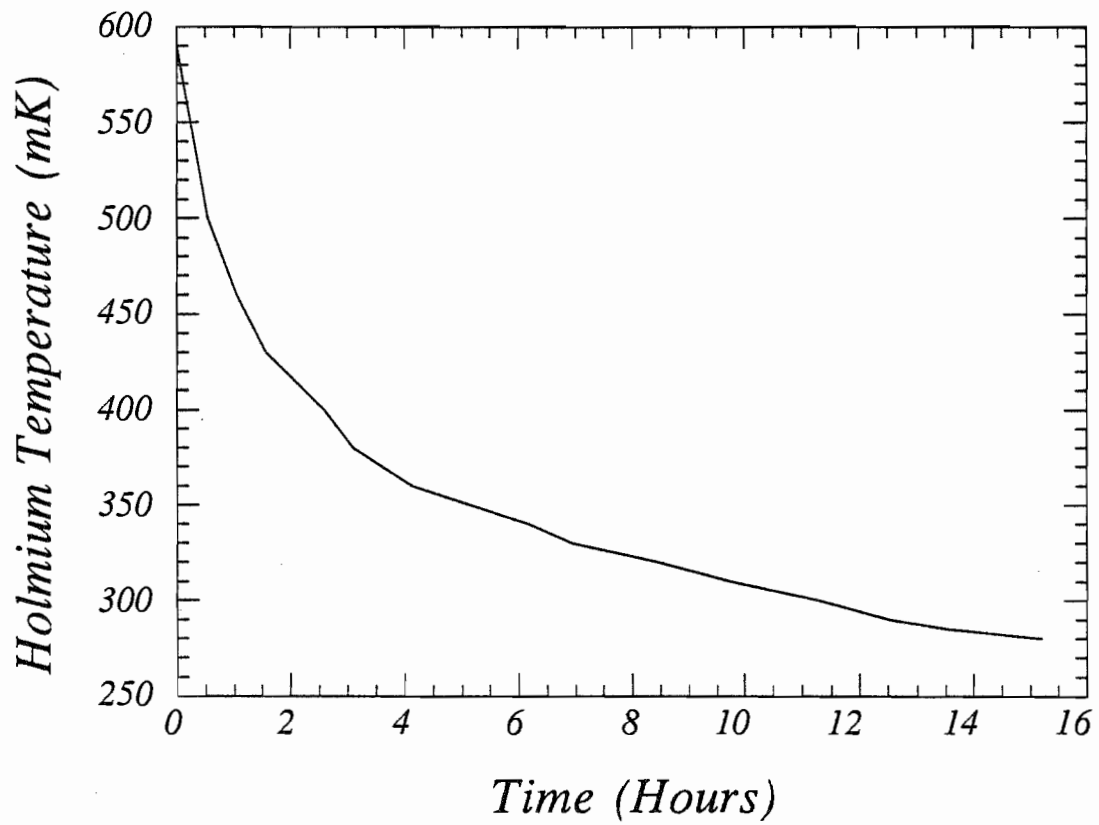


Figure 2.8: Cooling of the holmium target with time.

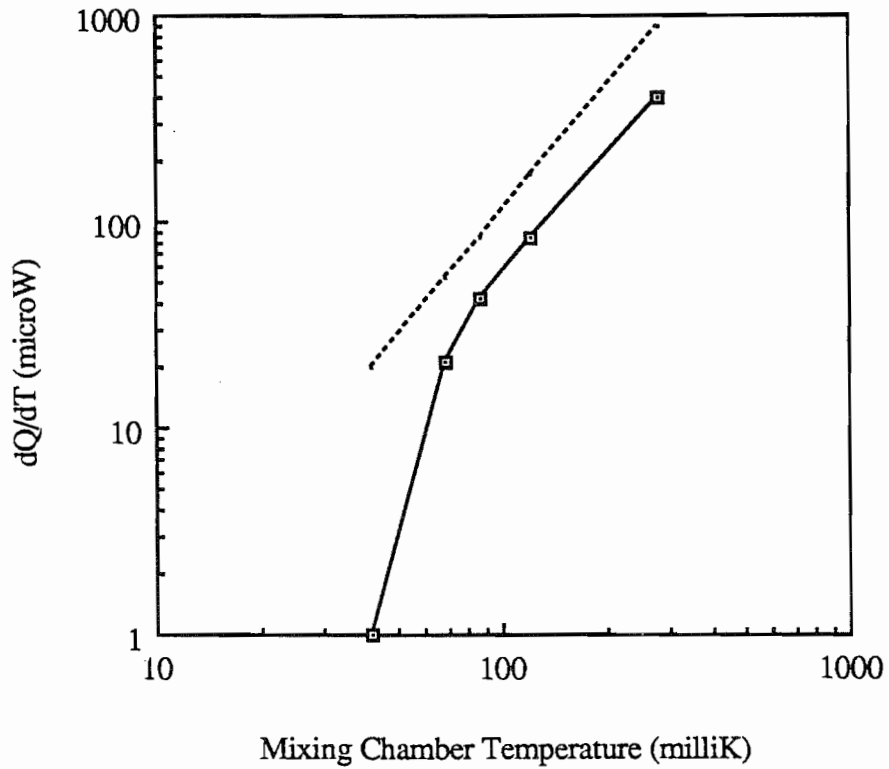


Figure 2.9: Mixing chamber temperature as a function of heat input. The squares plot the experimental data, interpolated by the solid line. The dotted line is the theoretical best performance (see text).

Input Module, operated with an IBM PC clone. The connections are shown in figure 2.10. The TI reads the angular position of the target from the shaft encoder, and sends appropriate control signals to the stepper motor. These signals are produced by a relay ladder logic (RLL) program run with TISOFT2. The program takes the current target angle and the input destination angle and deduces which direction to rotate the motor. The input comes externally (see Sec. 5.4) but can be forced with the PC. (In RLL these logic inputs and outputs are represented as electrical circuit switches.) When the target is at the destined angle, other logic outputs are set appropriately and sent to a remote location (the TUNL control room.) The exact angles which can be chosen according to the shaft encoder are set in the RLL program. Since the encoder utilizes 13 bits, 8092 angles are potentially available. This is nearly commensurate with the stepper motor-gear box positions. The motor has a 0.9° step or 400 steps per revolution. With a 25:1 gear ratio, the rotating shaft has 10,000 possible positions. This 0.04° resolution is well within the uncertainty in the target angle due to initial positioning, free play, and reproducibility discussed in section 2.3.2.

2.4 UNPOLARIZED NEUTRONS

The floor plan of the Laboratory is shown in figure 2.11. The neutron beam cannot be accelerated to MeV energies, of course. This beam must be secondary, resulting from a charged particle beam. An H^- beam is produced by the Direct Extraction Negative Ion Source (DENIS) and then accelerated with the TUNL FN Tandem Van de Graaff to several MeV. Deflection through 59° in an analyzing magnet determines the proton energy. Three sets of pickoff slits are used inside the 2 inch beamline to monitor or collimate beam position; any resultant current picked up on these is fed back to magnetic steerers upstream which keep the beam centered by minimizing or balancing the feedback currents. The placement of these and other components beyond the high energy end of the accelerator

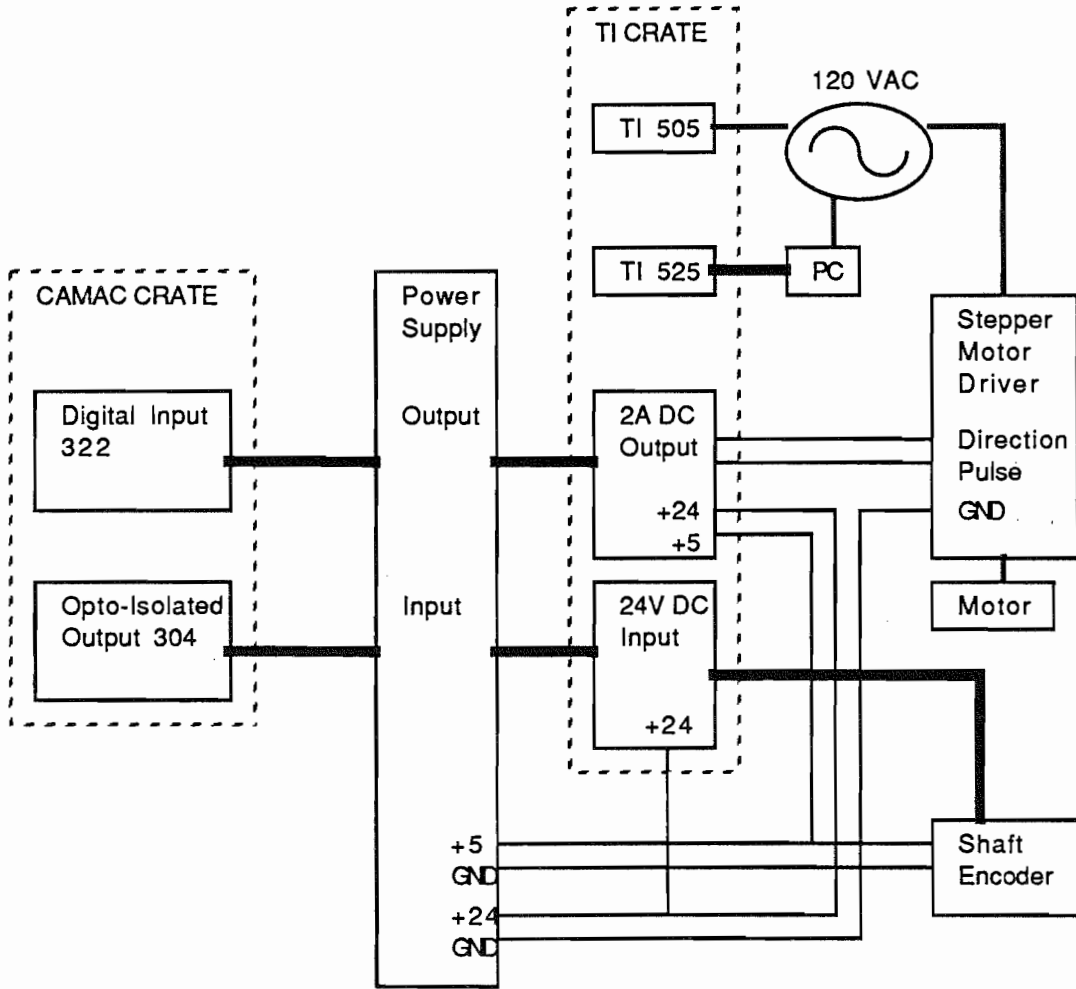


Figure 2.10: Computer control of the rotation drive.

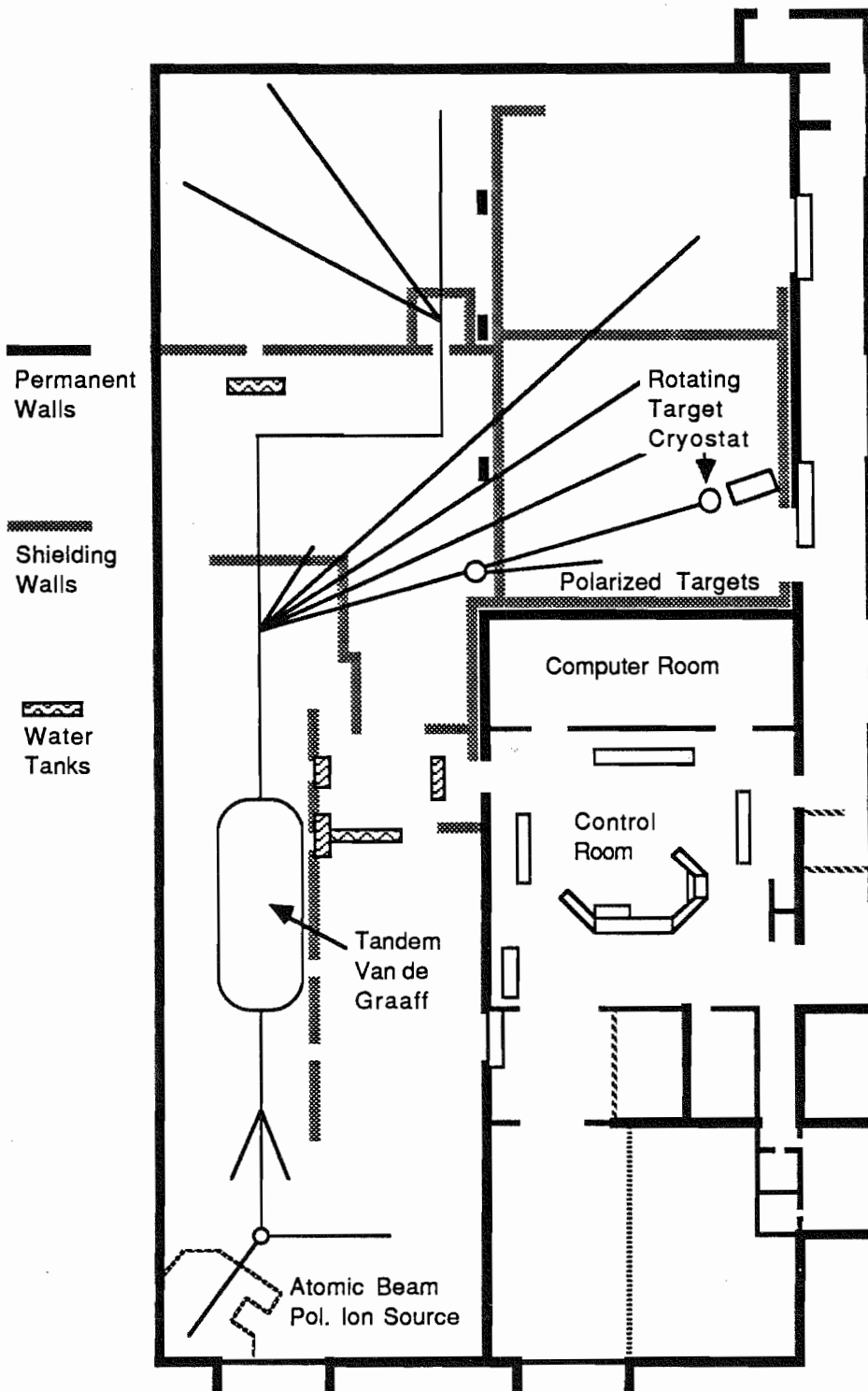


Figure 2.11: Floor plan of the Triangle Universities Nuclear Laboratory.

is shown in figure 2.12. Display of the beam position and shape in the pipe is obtained with beam scanners. During a run, the beam scan on the 59° line is displayed and stored in the computer, enabling us to monitor the focussing of the beam prior to neutron production. A final set of fixed slits is just upstream of the neutron production cell.

The $T(p,n)$ reaction at 0 degrees produces the neutrons. (The large polarization transfer will be important for polarized beam.) (Liskien 1973, Simmons 1973) A tritiated titanium foil (Safety Light Corp.), 1.07 mg/cm^2 , having a nominal concentration of 5 Ci/in^2 , was punched out as a $3/4$ " disk on a 0.010 inch thick OFHC copper backing and mounted in the proton beam. This thickness of titanium corresponds to an 80 keV energy loss in a 3.0 MeV proton beam. Only energies of below 5 MeV were chosen in order to avoid neutron production from the $\text{Cu}(p,n)$ reaction; however, the copper backing is thick enough to stop 10 MeV protons. A buffer gas cell of 1 atm helium precedes the TiT_2 foil, and is separated from beampipe vacuum by a 0.25 mil Havar foil. (See figure 2.13.) This cell design increases the cooling of the foil, eliminates pressure drops across it, and—most importantly—contains any liberated tritium or TiT_2 flakes (deRas 1989). In tests with a $1.1 \mu\text{a}$, 6.2 MeV proton beam, ^3H was detected afterwards in the buffer gas at levels about 10 times above the lab air background of 0–10 $\mu\text{Ci/m}^3$. The amount was more correlated with time in beam than with temperature (at least below 34°C), which was found to rise only 13°C above room temperature for a 7 Watt beam. Thus compressed air cooling of the copper backing is adequate to keep the titanium layer cool. The energy spread of the neutrons is due mostly to the finite thickness of the titanium layer; additionally a spread equal to 10% of the energy loss of the proton beam is assumed to occur. The energy losses of this cell are shown in table 2.1, yielding for example a 107 keV spread in a 1.5 MeV neutron beam (where the supposed energy is that of neutrons produced in the center of the titanium layer.) The gas cell – foil assembly was electrically isolated from the beampipe by a ceramic ring. The positive beam dumped here was picked

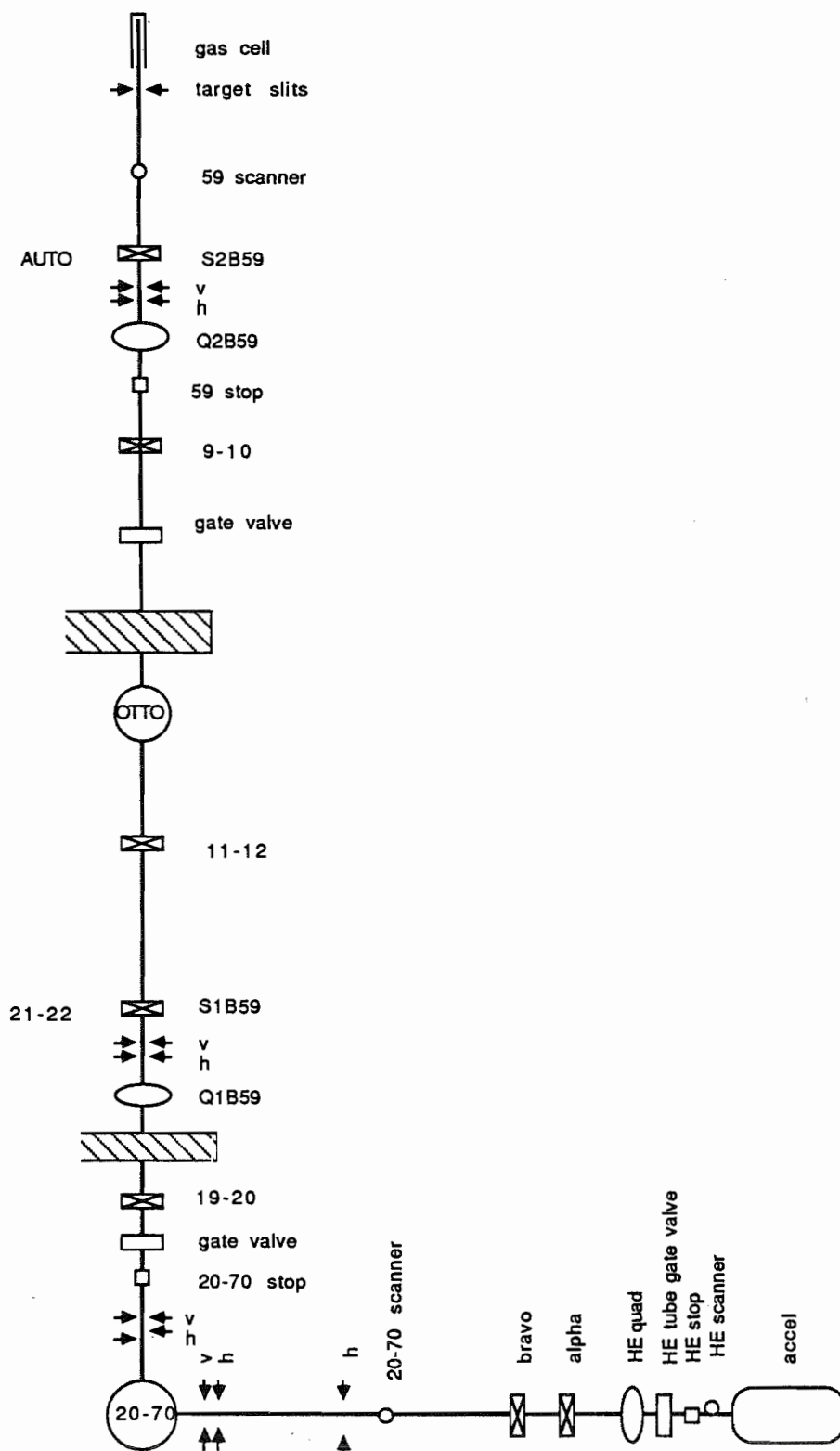


Figure 2.12: 59° beam line.

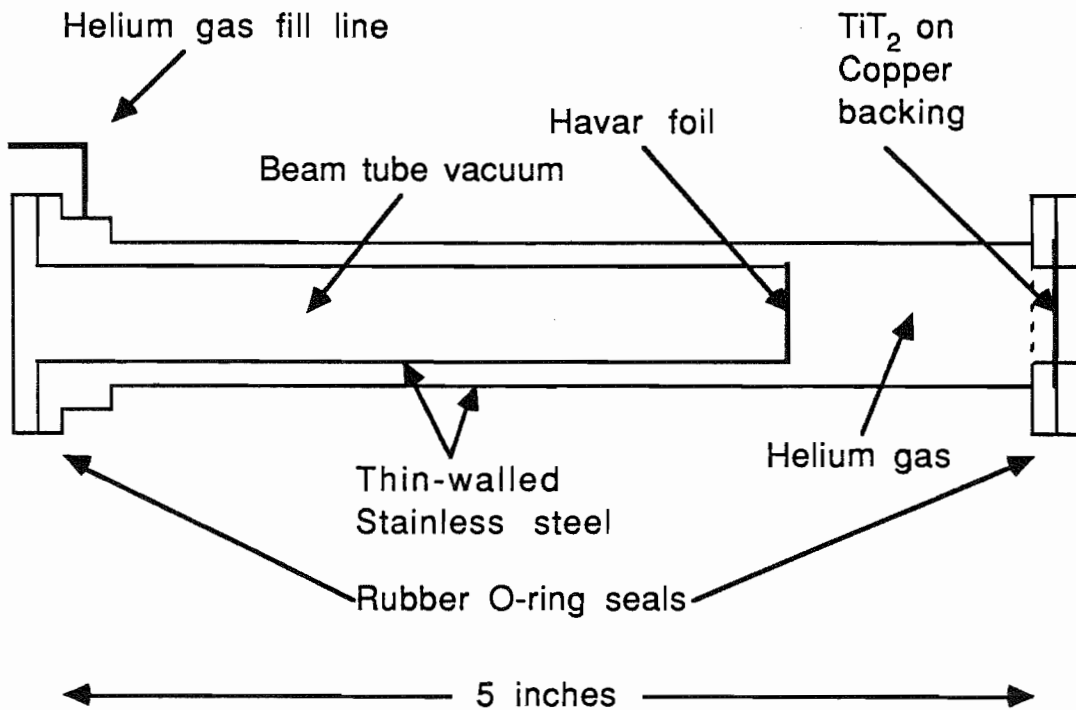


Figure 2.13: Neutron production cell.

Table 2.1: Energy losses in neutron production cell.

Incident Proton Energy (MeV)	Loss in Havar and Helium gas (keV)	Thickness of Titanium Layer (keV)	Energy of Neutrons at Center of Layer (MeV)	Neutron Energy Spread (keV)
2.780	470	96	1.47	107
3.105	432	87	1.84	97
3.175	425	85	1.92	95
4.985	303	58	3.88	65

off and sent to a current integrator.

The TiT_2 foil, holmium target, and neutron detector are arranged in an open geometry (figure 2.14) whereby only the detector is heavily shielded. The walls of the dewar tail enclosing the target amount to $3/16$ " of aluminum and $1/8$ " of stainless steel in the path of the neutrons. The target itself is 0.42 mean free paths thick for 1.5 MeV neutrons, corresponding to 66% transmission. The tapered neutron channel through the polyethylene collimator is designed to allow a solid angle corresponding to a $2\text{ cm} \times 2\text{ cm}$ window within the holmium cylinder. The collimator was aligned with the beampipe by sighting with a transit (after removal of the target and detector.) Cross-hair plates were fabricated to indicate the center of the various apertures: the center of the collimator at which the face of the detector was placed, the front of the collimator, and two ends of the beampipe. These centerpoints were set to be collinear to within 50 microns. The mounting of the holmium cylinder on the dilution refrigerator coldfinger was done as follows: A line was scribed on the bottom face of the holmium crystal parallel to its c -axis. A string was stretched taut between the center of the TiT_2 foil and the center of the front aperture of the collimator. The string permitted horizontal

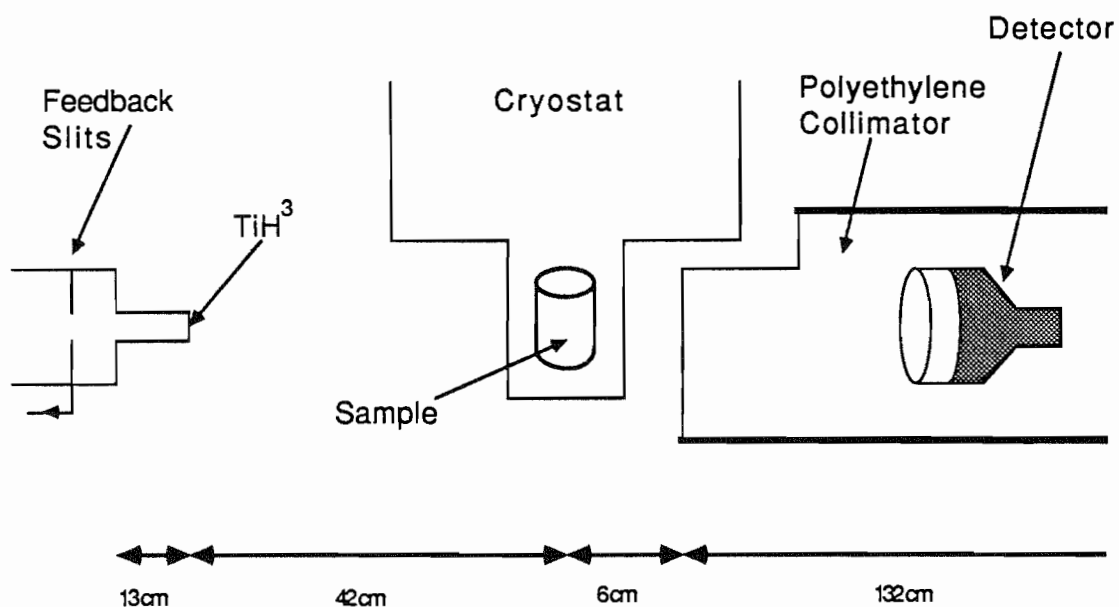


Figure 2.14: Neutron beam set-up.

placement of the whole cryostat transverse to the beam direction. The cylinder and coldfinger were mounted vertically on the rotating shaft so that a level string crossed the holmium 4 mm below its vertical center (thus allowing for thermal contraction of the cryostat.) This positioning was verified by sighting a transit through the collimator onto the holmium. Horizontal translation of the transit indicated the placement of the holmium with respect to the center axis of the collimator. Additionally, the c-axis was aligned with the beam in the following manner. The rotating shaft was held to what is defined as $\theta = 0^\circ$ by the stepper motor. With the set screws loosened, the target and coldfinger were turned on the rotating shaft until a scribe mark on the bottom face of the target was parallel with the string. This scribe mark denotes the direction of the c-axis. This put the c-axis to within $\pm 1^\circ$ of the beam direction.

The transmitted neutrons are detected with a 5 in \times 5 in organic liquid scintillator (Bicron BC-501) mounted on a 5 inch diameter Hamamatsu Photonics (R1250-03) photomultiplier tube (PMT). The scintillator provides protons which excite or ionize the atoms in the scintillator by proton recoil in (n,p) scattering. This is then followed by de-excitation through photon emission or by recombination. These photons eject photoelectrons from the photocathode of the PMT, which in turn are multiplied by a dynode chain. The resulting current pulse at the phototube anode represents the neutron event. Gamma rays similarly produce detector signals—however the intermediate ionizing radiation is compton-scattered electrons, leading to a different dependence on time of the current pulse at the anode. The fast-rising neutron pulses are distinguished from the slower-rising gamma-ray signals by pulse shape discrimination (PSD, Adams 1978) with a commercial module (Link Analytical PSD 5020) having very short dead-time. The module then functions as a single channel analyzer, whose output is scaled in the computer.

The detector-signal-processing-electronics is diagrammed in figure 2.15. A 50 Ω low loss cable runs directly from the PMT anode in the target room to the

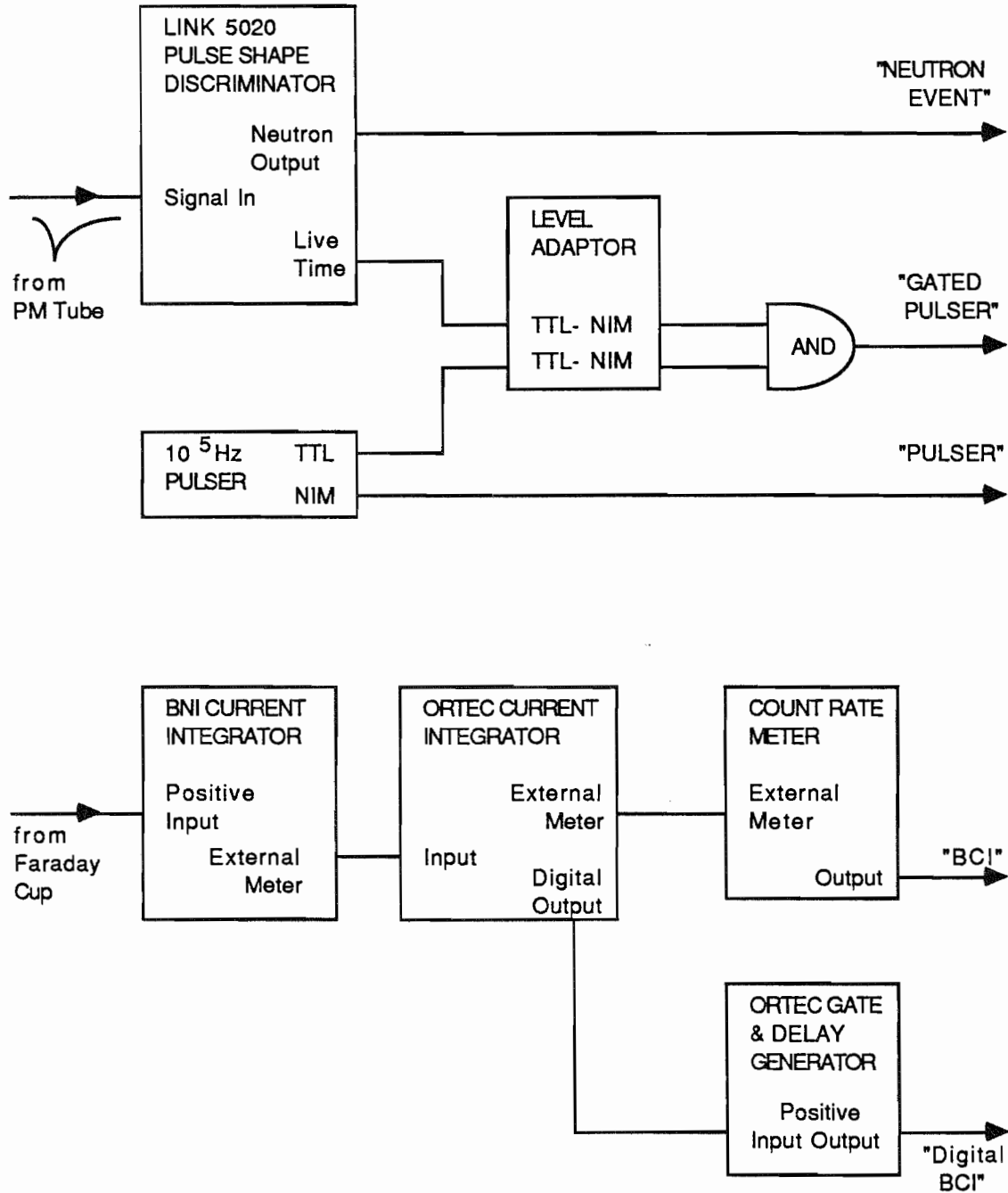


Figure 2.15: Block diagram of electronics for processing detector signals. Signals enter on the left from the target room. Signals on the right are sent to the computer interface.

PSD module in the control room. The PSD is tuned to select the neutrons properly, with an energy threshold set above any neutrons from $\text{Cu}(p,n)$ reactions in the TiT_2 backing. The lower level discriminator is then set above this threshold, and above any poor separation of neutrons and gamma rays. The upper level discriminator is set just beyond the neutrons. This tuning is done with an oscilloscope. The digital output signaling a neutron event is then sent to the computer interface.

There is always time when the electronics ignores an incoming signal because some module is processing a previous signal. In the processing used here, the PSD module has the longest "dead-time", with an amount that varies according to the settings of the module. Table 2.2 shows the values for the 5020 module and for the older 5010 module, illustrating that the module is dead chiefly while generating an output signal. The 5020 is run in the minimum dead-time configuration of

Table 2.2: Dead times in various PSD module configurations.

Model #	Timing Out pulse rate	Link Output Selection		
		Analog OFF	Analog ON	Display ON
		93 K/sec	68 K/sec	42 K/sec
5020	Specified dead time	300 ns	3 μs	12 μs
	DT observed with Timing Out	260 ns	4 μs	13 μs
	Analog output width	-	4 μs	13 μs
5010	Specified dead time	-	1.5 μs	5 μs
	DT observed with Timing Out	-	2 μs	6 μs
	Analog output width	-	900 ns	4.5 μs

260 nsec; this is assumed to be the dead-time of the whole system. The percentage of real time that the module is dead depends on the input rate so it is better to track the dead-time during an experiment in case any beam current fluctuation

occurs. This is accomplished with a 10^5 Hz pulser which samples the "live-time" of the PSD module. This live-time is inhibited when the module is busy, and so a coincidence between the live-time and the pulser is inhibited at such times. By scaling the pulser counts and the coincident counts, a dead-time correction is calculated as the ratio.

Previously dead-time calculations compared the number of events which got through the PSD module due to LED flashes onto the PMT, with the number of pulses synchronized to the LED flashing. Such a system measured the dead-time of the line between the PMT and the PSD module, inclusive. Furthermore, by stabilizing the LED peak that appeared in a pulse-height analysis of the analog output of the PSD module, gain drifts in the PMT and electronics were also minimized. However, table 2.2 shows that getting the analog output required of such a configuration increased the dead-time dramatically. Hence this method was rejected.

Figure 2.15 also shows the current integration from the neutron production cell that comprised a Faraday cup for the proton beam. A high impedance input Brookhaven Nuclear Instruments #1000 current integrator is used, whose analog output has high zero-point stability as an input to an Ortec #439 current integrator. Its analog output is in turn sent to a Count Rate Meter whose control settings place a gate on the acceptable beam current. This is latched to the computer crate, to inhibit taking data with unacceptable beam intensity. Also, the digitized output of the Ortec C.I. is scaled in the computer to provide normalization of the neutron detector yields. Wiring of the signals to the VAX 11/780 computer interface is identical to that used in the time reversal invariance experiment and is discussed in more detail in section 5.4.

Chapter 3

NUCLEAR DEFORMATION EFFECT MEASUREMENT

3.1 DATA ACQUISITION

Neutron counts are acquired and stored on-line with a Digital Equipment Corporation VAX-11/780 computer. The hardware interface between this and the signal-processing electronics is accomplished with CAMAC modules controlled by a Microprogrammed Branch Driver MBD-11. This hardware system has been used successfully at TUNL for many years (see Roberson 1981). The interface also directs the microprocessor which controls rotation of the holmium target (see Sec. 2.3.5). Online control of the MBD, the target position, data sorting, and calculation is effected with TUNL XSYSem software (Gould 1981). General purpose commands comprise the XSYS package, which is written in FORTRAN, containing system input/output commands. Particular sets of XSYS commands used in this experiment are incorporated in DEC Command Language programs. Execution of the latter provides for automatic data acquisition.

For the deformation measurements, neutron counts were collected typically for periods of approximately 820 seconds. In between these periods, the aligned

holmium target was rotated by 30° or 45°. A digitized signal from the beam current integrator was accumulated during each period. The neutron counts were normalized with this. Dead-time corrections were estimated as discussed in Sec. 2.4 and applied to the detector-to-BCI ratio. (Actually, all this was sorted into two spin states—see the discussion of the five-fold correlation measurement in section 5.4—but here the two resultant ratios were averaged.) This ratio is plotted in figure 3.1 for 1.8 MeV neutrons.

3.2 DATA REDUCTION AND ANALYSIS

The predicted form of the neutron transmission as a function of target alignment position is derived with the formalism of Gould, et. al. (1990). For an oriented beam and an oriented target, the total cross-section is decomposed as

$$\sigma_T = \sum \sigma_{kK}. \quad (3.1)$$

Here k is the order of beam orientation, $k \leq 2s + 1$, where s is the spin of an incident nucleus; K is the order of target orientation, $K \leq 2I + 1$, with I the spin of the target. Now

$$\begin{aligned} \sigma_{kK} = & \operatorname{Re} \left\{ 2\pi \lambda^2 \sum_{\Lambda q} \hat{\Lambda} \langle \Lambda k 0 q | K q \rangle t_{kq}(s) t_{Kq}^*(I) \sum_J g_J \times \right. \\ & \left. \sum_{l'l'j'j} T_{Kk\Lambda}(l'j'lj) [\delta_{ll'} \delta_{jj'} - S_J(lj \rightarrow l'j')] \right\} \end{aligned} \quad (3.2)$$

where

$$g_J = \frac{(2J + 1)}{(2s + 1)(2I + 1)} \quad (3.3)$$

is the spin multiplicity, $T_{Kk\Lambda}$ contains the angular momentum couplings, and $S_J(lj \rightarrow l'j')$ is the S-matrix element for the transition from incoming channel (lj) to outgoing channel ($l'j'$). Spin-orbit coupling is used: the total projectile spin is $\vec{j} = \vec{l} + \vec{s}$, the total spin of the system is $\vec{J} = \vec{j} + \vec{I}$, and Λ is defined by the couplings $\vec{\Lambda} = \vec{l} + \vec{l}'$ and $\vec{\Lambda} = \vec{k} + \vec{K}$.

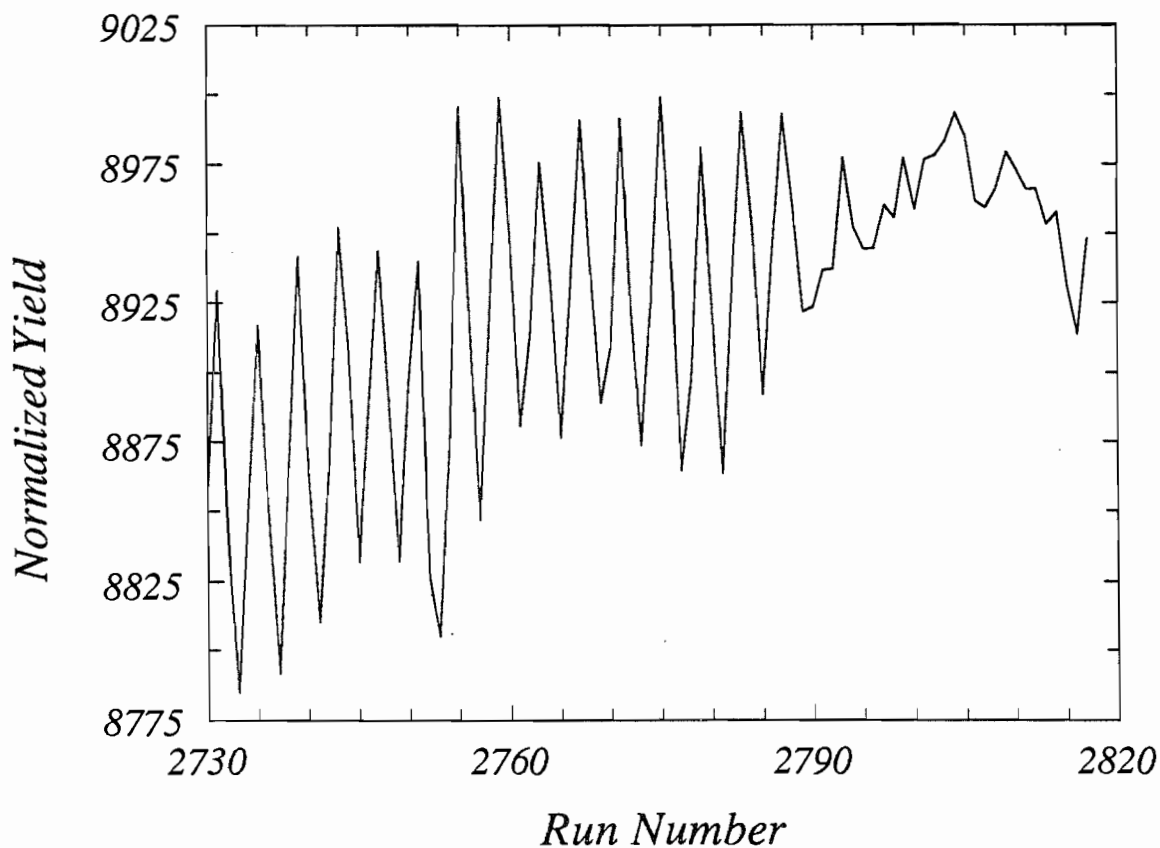


Figure 3.1: Ratio of neutron detector yield to beam current, with dead-time correction, at 1.8 MeV. The oscillation with a period of four runs is due to changes in the direction of alignment of the deformed target. This oscillation disappears after run 2788 because the target was warmed. Also evident is a long-term drift in the average yield due to phototube gain drift. (See text.)

For the deformation measurements the beam is unpolarized ($k = 0$) and the target aligned (odd $K = 0$). In this case 3.2 reduces to

$$\sigma_{0K} = \text{Re}\{2\pi\lambda^2 \hat{K} t_{K0}^*(I) \sum_J g_J \sum_{l'j'lj} T_{K0K}(l'j'lj) [\delta_{ll'} \delta_{jj'} - S_J(lj \rightarrow l'j')]\} \quad (3.4)$$

so that

$$\sigma_T = t_{00}\sigma_0 + t_{20}\sigma_2 + t_{40}\sigma_4 + \dots \quad (3.5)$$

where

$$\sigma_K \equiv \sigma_{0K}/t_{K0} \quad (3.6)$$

is a cross-section independent of the degree of orientation t_{K0} and of the angle θ between the target c-axis and the beam direction. For $K = 2$, t_{20} , the alignment with respect to the beam direction, is given in terms of \hat{t}_{20} by equation 2.11,

$$t_{20} = P_2(\cos \theta) \hat{t}_{20}. \quad (3.7)$$

The alignment with respect to the crystalline c-axis \hat{t}_{20} is given by equation 2.16, and the Legendre polynomial is

$$P_2(\cos \theta) = \frac{3 \cos^2 \theta - 1}{2}. \quad (3.8)$$

If the temperature of the target is low enough, alignments of higher order may occur. The temperatures reached with the holmium target ($T \geq 270 \text{ mK}$) all but precluded this sensitivity to higher order σ_K . Nevertheless, the presence of σ_4 was tested in the data for completeness. The angle dependence of this follows from equation 2.11,

$$t_{40} = P_4(\cos \theta) P_4(\cos 80^\circ) t_{40}^{\text{planar}} \quad (3.9)$$

where t_{40}^{planar} is the temperature-dependent $K = 4$ order of orientation with respect to a basal plane.

Three other major considerations can affect the form of equation 3.5. The first is the possibility of an offset in the direction of the alignment axis of the holmium target, from where the c-axis is believed to be. The other two considerations

involve a change in time of the neutron yield unrelated to target position. One such effect may be present due to fluctuations in the target temperature and thus its alignment. The other, more pervasive, effect is due to drifts in the gain of the photomultiplier tube. This effect is quite visible in figure 3.1. As discussed previously, the PMT was not gain-stabilized. This was so not only to keep the dead time small, but also because the thrust of these measurements was the FC test with polarized beam. The time-scale for stabilizing detector gain was longer than the time scale on which the neutron spin cycled (8 spin states per second.) However, for a total yield this drift has an appreciable effect. The normalized yield has the following general form,

$$N(\theta, \phi, t) = N_0(t)e^{-n\sigma_T(\theta, \phi, t)}, \quad (3.10)$$

$$\begin{aligned} \sigma_T(\theta, \phi, t) = & \sigma_0 + P_2(\cos(\theta + \phi))P_2(\cos 80^\circ)\hat{t}_{20}(t)\sigma_2 \\ & + P_4(\cos(\theta + \phi))P_4(\cos 80^\circ)\hat{t}_{40}(t)\sigma_4. \end{aligned} \quad (3.11)$$

Here $N_0(t)$ is the time-dependent drift in the apparent detector count per unit beam current, n is the mean target thickness, ϕ is the offset angle of the alignment axis, and $\hat{t}_{K0}(t)$ is the time-dependent degree of alignment with respect to the alignment axis. The second relation is just 3.5 made explicit. The importance of the form of 3.11 is that the constant parameters σ_K can be extracted, independent of the alignment. These parameters differ from previous parameters found in the literature. The common one was $\Delta\sigma_{def}$ (see e.g., Marshak 1970), where

$$\Delta\sigma_{def} = t_{20}\sigma_2 + t_{40}\sigma_4 + \dots \quad (3.12)$$

Its dependence on the statistical tensors had to be investigated through the latter's temperature dependence. Past experiments were done with ^3He cryostats in which the holmium targets were never cold enough to have an appreciable $K = 4$ alignment. At 260 mK our target is somewhat colder, and the angular dependence in our measurement provides another important means of separating the various terms in 3.12. Data was also taken for a "warm" target ($T > 2.8$ K) in which the alignment was usually much less than 2% of maximum.

It is difficult to fit the data to the form 3.10 with its free parameters (ϕ , σ_K) and functional dependences on t and P_K . Instead we have investigated each dependence separately. The most significant is the drift in detector gain, which can be removed in two ways.

- A) A truncated Fourier transform is performed on the data.
- B) Each data set is fit with a line or quadratic (as a function of time)—this time-dependent slow drift is then subtracted off.

The first option is possible because of the angular dependence. Previous deformation effect measurements were made by comparing transmission through a cold (oriented) stationary target and through a warm (unoriented) target. The thermal cycling time is much longer, and indeed, detector drift could be more of a problem. The usefulness of our modulation by rotation—rather than by temperature—is made explicit by looking at the frequency spectrum. The deformation effect due to rotation is evinced by a peak in the transform. The transform is set to zero for frequencies far from the rotation, then the data are transformed back to time. This is equivalent to electronically filtering the data with a band-pass around the appropriate frequency. (The result for the data in figure 3.1 is plotted in figure 3.2. The cold and warm sets have been fit separately with a $\cos^2 \theta$ distribution as described later in this section; the fits are graphed as a dashed line. The warm data show random fluctuations of smaller amplitude than the deformation effect evident in the cold data and lacking any coherence with rotation.) It is possible in principle to deduce the errors in the yield introduced by fourier filtering. However, the choice of the range of accepted frequencies is ambiguous. The second option is perhaps more intuitive. It is feasible also because of the angular dependence—the slow drift in time of the yield is incoherent with target angle. However, the error introduced in this type of correction is unknown. In using both methods, rather similar results for the deformation cross-sections are ultimately produced because finally a fit is made using the angular dependence of the data. Hence for the final extraction we use the second method as it is the more

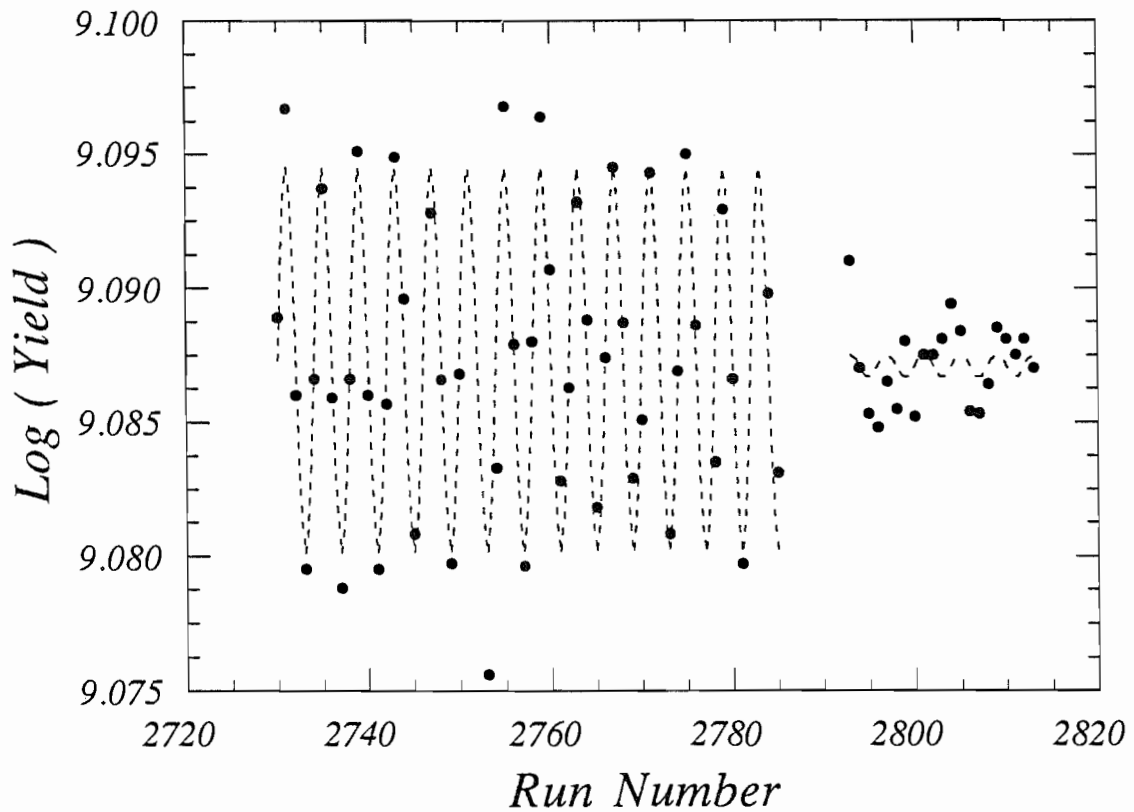


Figure 3.2: Transmission yield after slow time drift is removed. Only Fourier components of the signal around the appropriate frequency have been accepted. The dashed line represents a fit to each of the cold and warm data. The warm fit is statistically consistent with zero; its phase is determined by the fit to the cold set.

familiar “background” subtraction in nuclear measurements and does not suffer from the ambiguity in truncating the Fourier transform. Even so, it is instructive to plot the Fourier transform of a data set to see the presence of a signal with the correct angle dependence. This is important after data cuts are taken, because throwing away too much data was observed to destroy the signal.

In accord with the previous discussion, the raw normalized yield is plotted in figure 3.3, taken at 1.8 MeV with an aligned target. This is just the portion of figure 3.1 where the target was cold—however, data points where the beam current fluctuated greatly or dropped low, or where the detector did not track the beam well have been cut. The Fourier transform of the normalized yield is graphed in figure 3.4. If a component of the signal has a period of T runs, then the transform has a local maximum centered at $\omega_0 = 2\pi/T$. Because the angle sequence in figure 3.3 is $\theta = 0^\circ, 45^\circ, 90^\circ, 45^\circ, 0^\circ, -45^\circ, \dots$, the counts as given by equation 3.11 have a period of 4 runs (among other possible periods.) This explains the peak at $\pi/2$ in figure 3.4. The normalized yield after the target was warmed is plotted in figure 3.5. Its Fourier transform is graphed in figure 3.6. Clearly the signal with the correct θ dependence has vanished. The 1.5 MeV data, in contrast, was taken in the angle sequence $-90^\circ, -60^\circ, -30^\circ, 0^\circ, 30^\circ, 60^\circ, 90^\circ, 60^\circ, \dots$. The yield-to-beam current ratio for this data set (where suitable cuts have again been made) is plotted in figure 3.7. Here the data repeat every six runs, and so a peak in the power spectrum is predicted at $\omega_0 = \pi/3$. This is indeed the case in figure 3.8.

The quantity N^* is the detector to beam current ratio left after a time-drift subtraction is made.

$$N^*(\theta, \phi) = N_0^* e^{-n\sigma_T(\theta, \phi, t)}, \quad (3.13)$$

where N_0^* is now presumably constant in time. Taking the logarithm of 3.10,

$$\begin{aligned} \ln N^*(\theta, \phi, t) &= \ln(N_0^* e^{-n\sigma_0}) - P_2(\cos(\theta + \phi))P_2(\cos 80^\circ)\hat{t}_{20}(t)n\sigma_2 \\ &\quad - P_4(\cos(\theta + \phi))P_4(\cos 80^\circ)\hat{t}_{40}(t)n\sigma_4 \end{aligned} \quad (3.14)$$

or

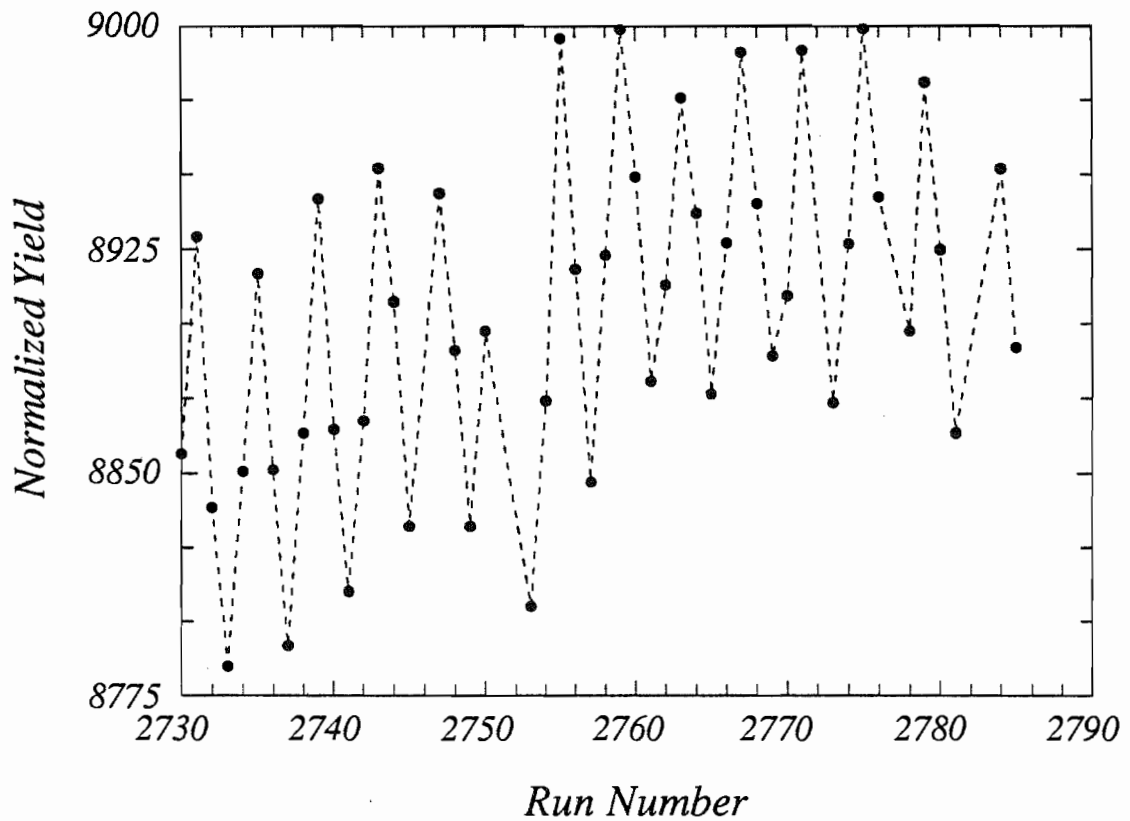


Figure 3.3: Normalized detector yield for 1.8 MeV neutrons and an aligned target. Data cuts have been made based on stability of the proton beam and the detector during each run. The dashed line serves only to guide the eye.

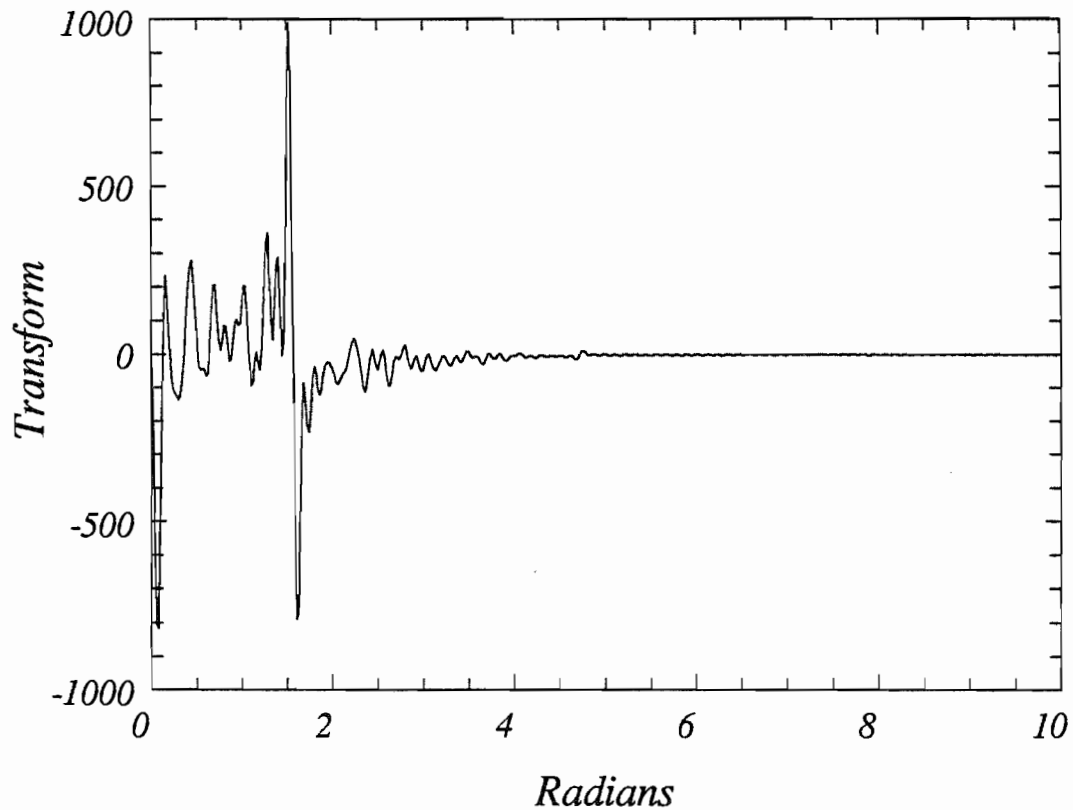


Figure 3.4: Fourier transform of transmission through an aligned target. The extrema at $\pi/2$ indicate the proper periodicity of the raw yield vs. run number.

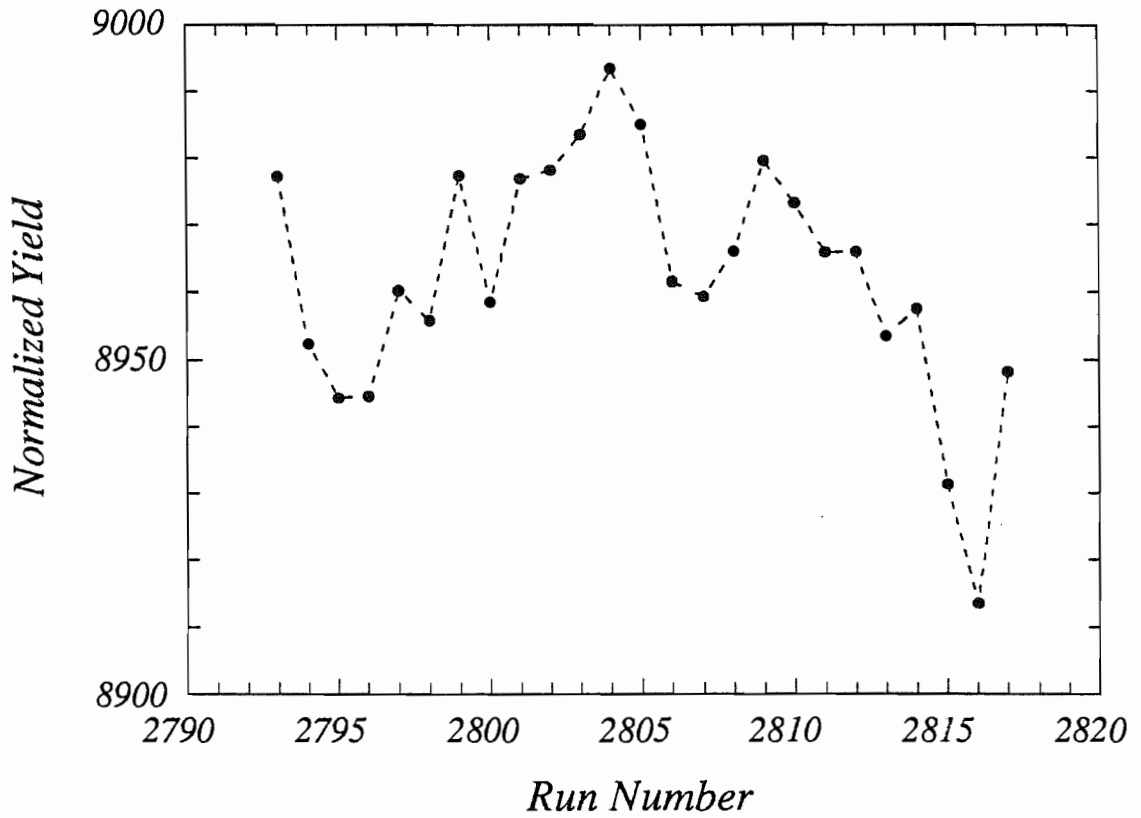


Figure 3.5: Normalized detector yield for 1.8 MeV neutrons and an unaligned target. The dashed line is an eye guide. The periodicity evident in figure 3.2 has vanished.

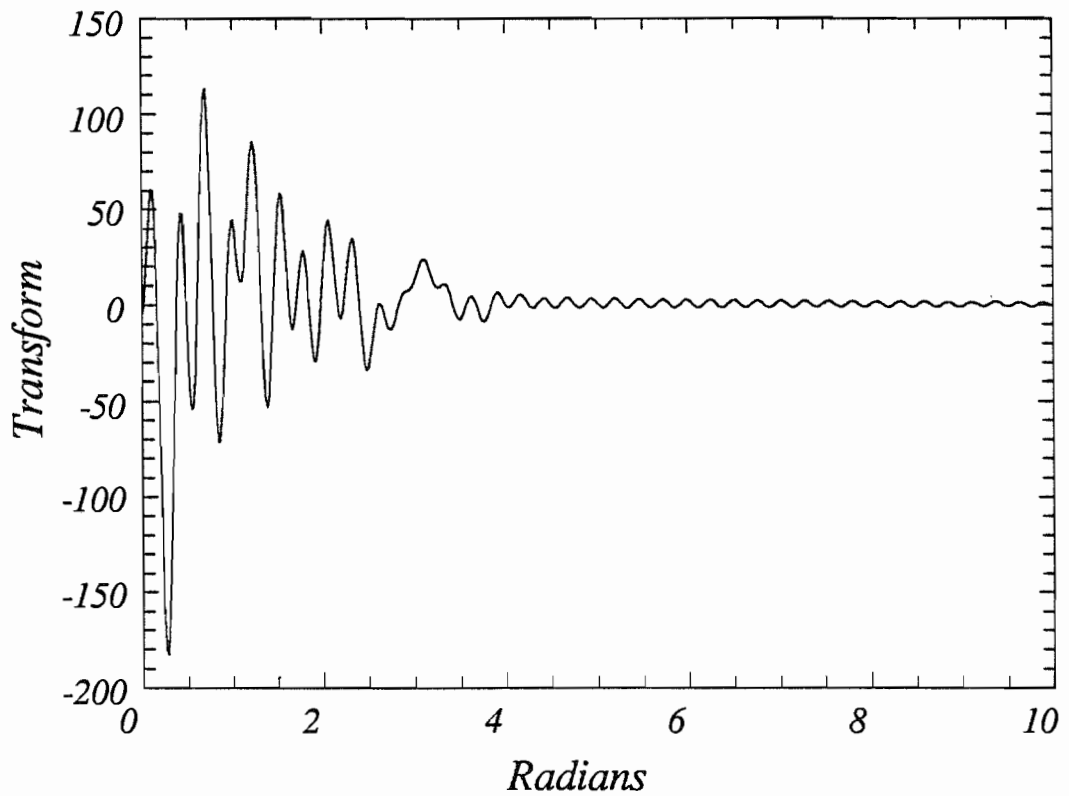


Figure 3.6: Fourier transform of transmission through an unaligned target. There is no peak above background evident at $\pi/2$. Note the expanded vertical scale compared to figure 3.4.

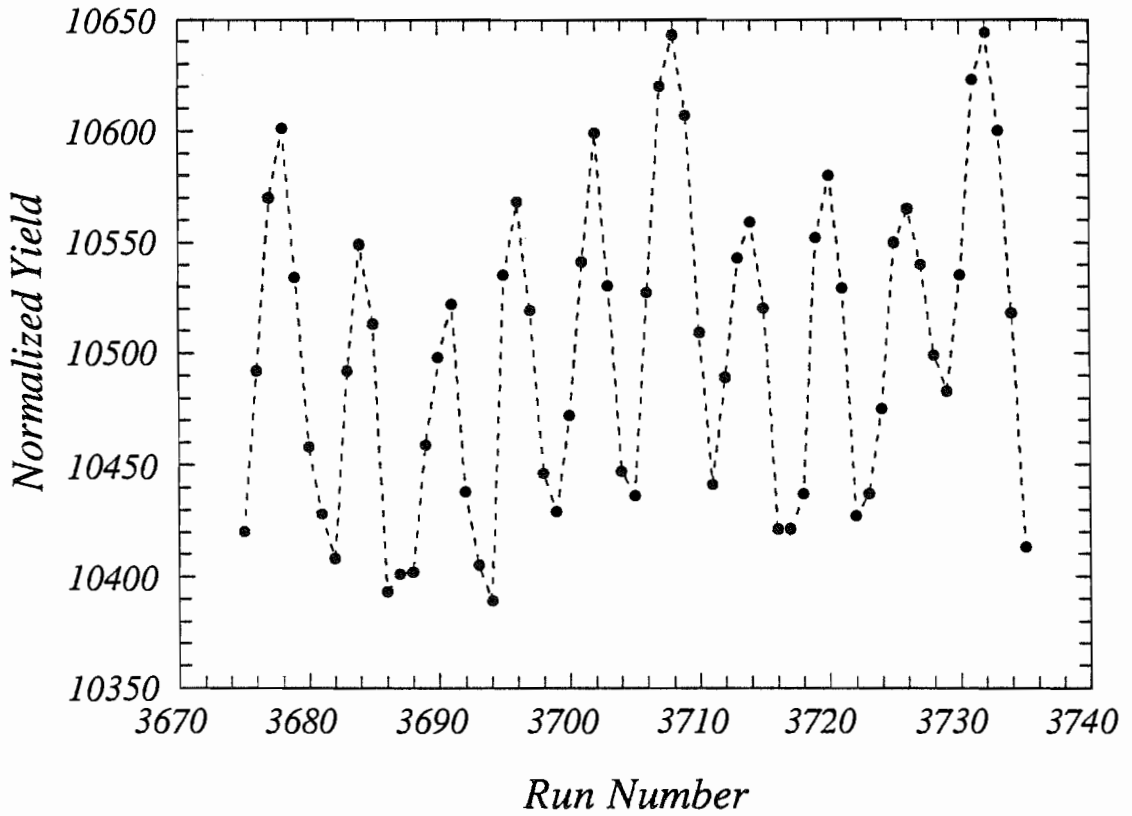


Figure 3.7: Normalized detector yield for 1.5 MeV neutrons and an aligned target. The angles θ used here differ from those for the 1.8 MeV data.

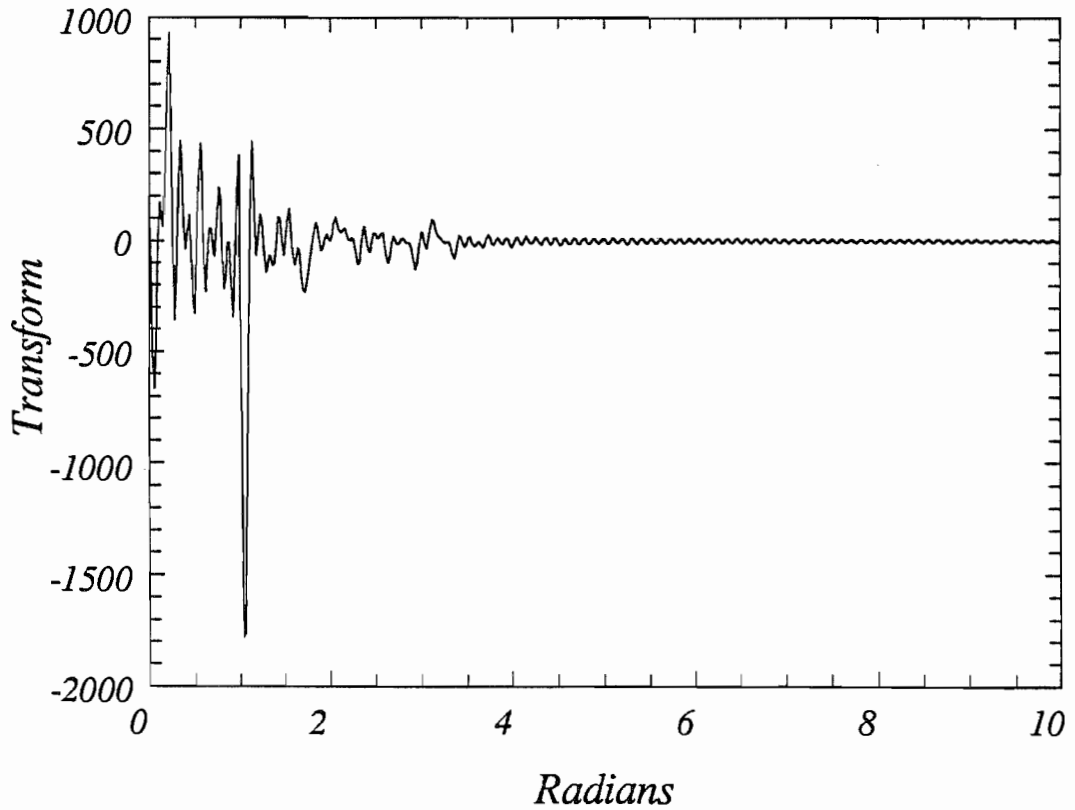


Figure 3.8: Fourier transform of the 1.5 MeV data. Note that the peak due to $P_2(\cos \theta)$ signal has shifted appropriately.

$$Y_\phi(\theta_i) = A + X_\phi(\theta_i)\sigma_2 + Z_\phi(\theta_i)\sigma_4. \quad (3.15)$$

Here Y is a *multiple* function of θ , so Y is parametrized by run number i , as are the angle θ and target alignment t_{K0} . The latter depends on i since so far it has not been assumed constant. Indeed t_{K0} may change in time coherently or incoherently—however, no evidence for temperature changes cohering with target angle has been observed.

Equations 3.10 and 3.11 have been reduced to equation 3.15 by removing time-dependent changes in the yield which are incoherent with target rotation. The latter equation can be simplified again through either of two ways.

- A) The t_{K0} may be taken constant in time. Then 3.15 has only angular dependence. The data $Y_\phi(\theta)$ are fit with a Legendre polynomial expansion.
- B) The $K \geq 4$ components are assumed negligible. An explicit set of $P_2 \times \hat{t}_{20}$ is taken as the abscissa, X_ϕ , for a particular value of ϕ . Equation 3.15 is then a linear equation in X , on which a least square fit is performed. The offset angle ϕ is varied in small increments about zero. Its value is chosen to minimize the χ^2 of the resultant fits.

Each of these simplifications was tried individually. To do so, one is made; then results are compared for whether the other is made.

Fluctuations in t_{K0} are indicated only by the resistance thermometers mounted on the target. For a target that has been cold for some time, it is reasonable to ascribe the fluctuations to electronics rather than real changes in the alignment of the holmium. Hence for such data sets assumption (A) is a good one. Indeed it was tested by comparison of the extracted σ_2 's with and without the assumption (the approximation (B) was made in such tests.) However, one data set began with a cooling target. The first half of that data set has to be discarded in making assumption (A) because a correction cannot be applied to those yields taken during the cooldown to make them correspond to a cold target, without

knowledge of N_0^* or σ_0 . Again, the σ_2 extracted from an analysis of the second half of the set assuming constant alignment was compared with the σ_2 from the full set. However, in either case no data were used where $t_{20} < 50\%$ because the target was cooling quickly then.

To test the approximation (B), those “cold” data sets where the target temperature (i.e., resistance thermometry) was reasonably constant were fit with even-order Legendre polynomials up to 2nd order and up to 4th order. The σ_4 extracted in every instance was consistent with zero, while the σ_2 extracted with and without σ_4 were consistent. Moreover, the additional $K = 4$ term did not improve the fits—i.e., reduce the χ^2 . It is also interesting to note the lack of any peak at π in the Fourier transform of the data in figure 3.4 that would be indicative of a $P_4(\cos \theta)$ signal. Thus this approximation was always taken following the subtraction of the time-dependent drift. The result at 1.8 MeV is illustrated in figure 3.9. Here $X_\phi(\theta_i)$ is plotted vs $Y_\phi(\theta_i)$ as indicated by equation 3.15 (where $\phi = 0$; see below.) The solid line is the linear least squares fit. Its slope yields σ_2 directly. The spread in the abscissa for each of the clusters of points is due to the fluctuations in temperature. For a constant temperature target these clusters collapse to three loci at $\cos^2 \theta = 0, 1/2$, and 1. The spread in the ordinate for each of the clusters is random fluctuation in repeated sampling of those values. The spread probably also still reflects a remnant time-dependent variation due to detector gain drifts.

The error bars associated with the data points in figure 3.9 are undetermined because of the slow-drift subtraction discussed above. The data are weighted with the appropriate values W_i which provide a reduced chi-square χ_ν^2 equal to one (Bevington 1969). The proper one-sigma errors in $\ln N^*$ are then $\delta = 1/\sqrt{W_i}$. These error bars are not directly of interest—however, χ_ν^2 must equal 1 in order to extract the uncertainty in the fitting coefficients such as σ_2 . This is applied explicitly first in searching on ϕ , the c-axis offset. The χ^2 of the fit is plotted for different values of ϕ near zero in figure 3.10, for the 3.9 MeV data. The weighting

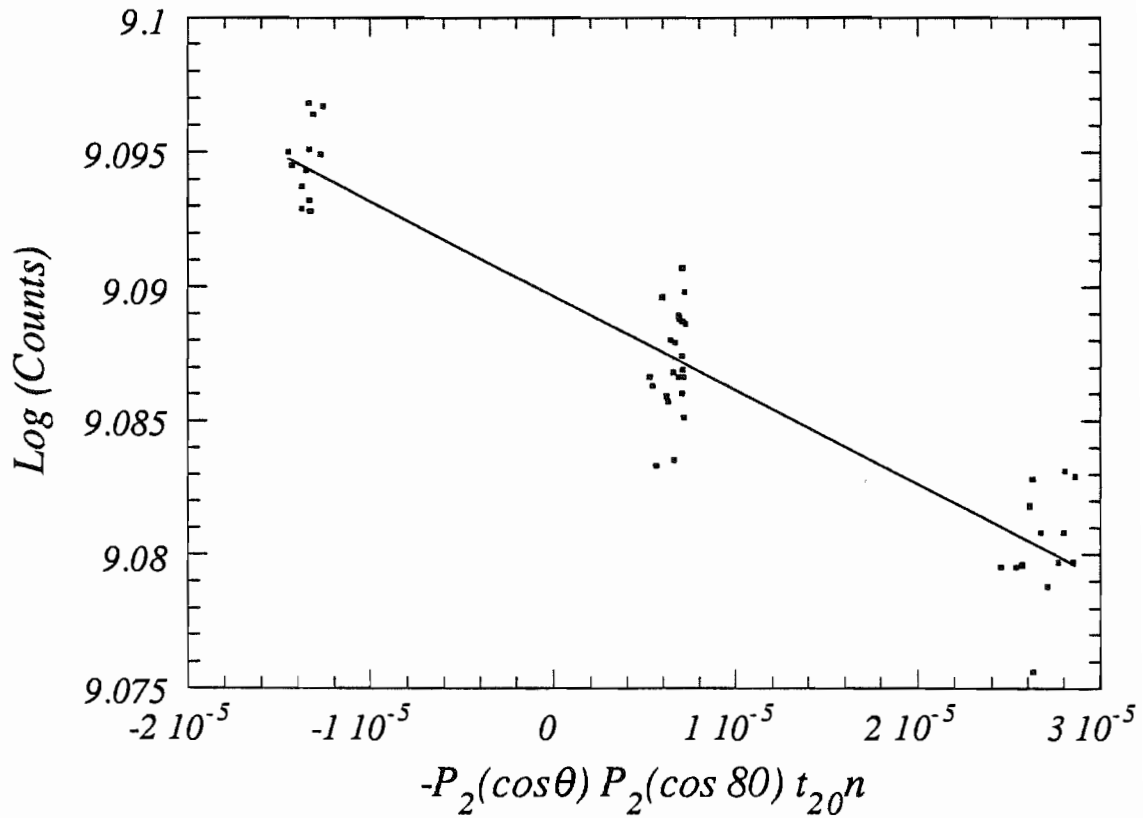


Figure 3.9: Logarithm of yield as a function of angle, with variations in degree of alignment. The solid line is the linear least squares fit to the points. The abscissa is chosen so that the slope of the line is given exactly by σ_2 .

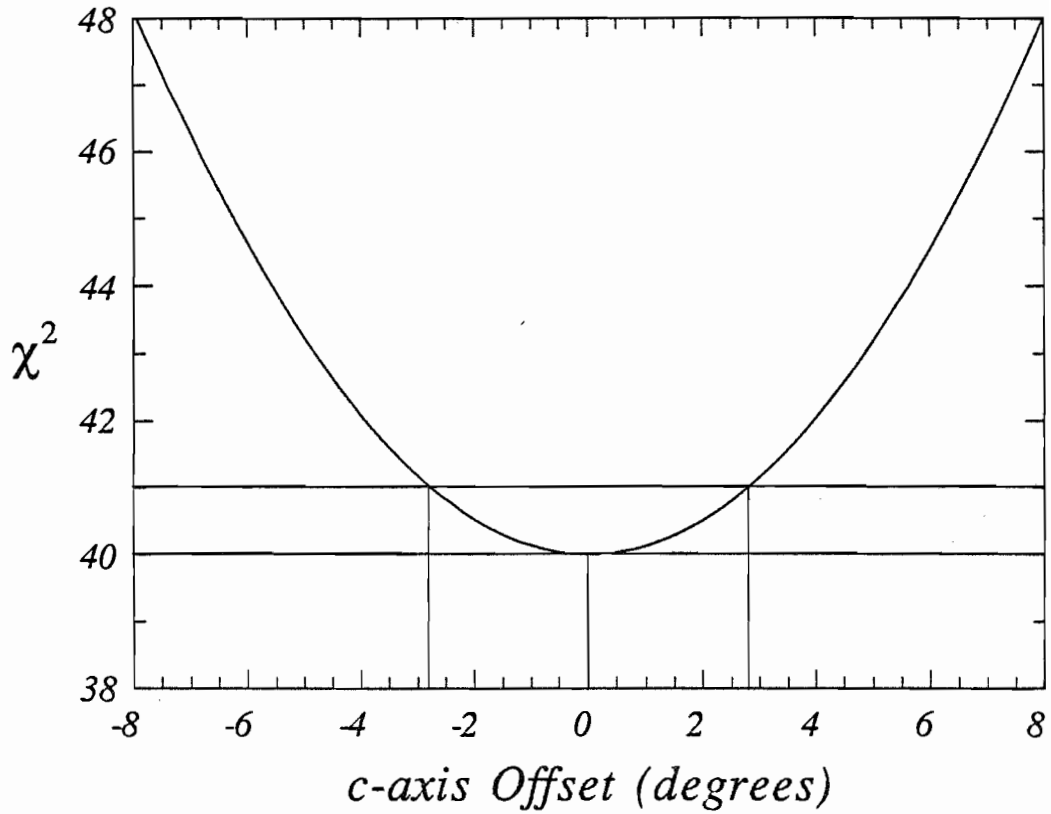


Figure 3.10: Chi-square fit of logarithm of yield as a function of *c-axis* offset. The minimum determines ϕ . The uncertainty in ϕ is that increment in angle which increases the χ^2 by one.

of $\ln N^*$ has been taken so that the minimum χ^2 is equal to the number of degrees of freedom. Then the uncertainty in the minimizing ϕ is given by the value where χ^2 has increased by one over its minimum,

$$\chi^2(\phi + \Delta\phi) = \chi^2(\phi) + 1. \quad (3.16)$$

This determination of ϕ was done for the 1.8 and 3.9 MeV cold data sets. The resulting ϕ and its uncertainty was found from the two sets combined to be -1.5 ± 3.1 . Because this is consistent with zero, ϕ was taken to be zero thereafter.

The uncertainty $\Delta\sigma_2$ in the coefficient σ_2 is then found in the same manner. This is illustrated in figure 3.11 for the 1.8 MeV data. This method of deducing uncertainties is based on repeated sampling and so incorporates any unknown random errors in addition to statistical errors.

3.3 DEFORMATION EFFECT RESULTS

Important quantities for the four measurements are summarized in table 3.1. The number of runs comprising each energy datum is the number that survive cutting the data on intense, stable beam and stable detector as discussed previously. The angle sequence for the 1.9 MeV measurement was chosen with regard to a simultaneous measurement of the FC. Although the deformation effect is very small at $\pm 135^\circ$, the FC amplitude is at a maximum there. The angle sequence for the 1.5 MeV data was chosen to increase the resolution between the two possible signal components $P_2(\cos\theta)$ and $P_4(\cos\theta)$. The former has a zero near 60° , while the latter has a zero near 30° . However, as is indicated by the degree of alignment relative to maximum t_{20} and implicitly by the holmium temperature, the target was not cold enough in this run to produce significant t_{40} alignment—and none was detected.

The results for the nuclear deformation effect σ_2 are summarized in table 3.2. Energies were chosen to permit measuring $\sigma_2(E)$ of differing magnitude and

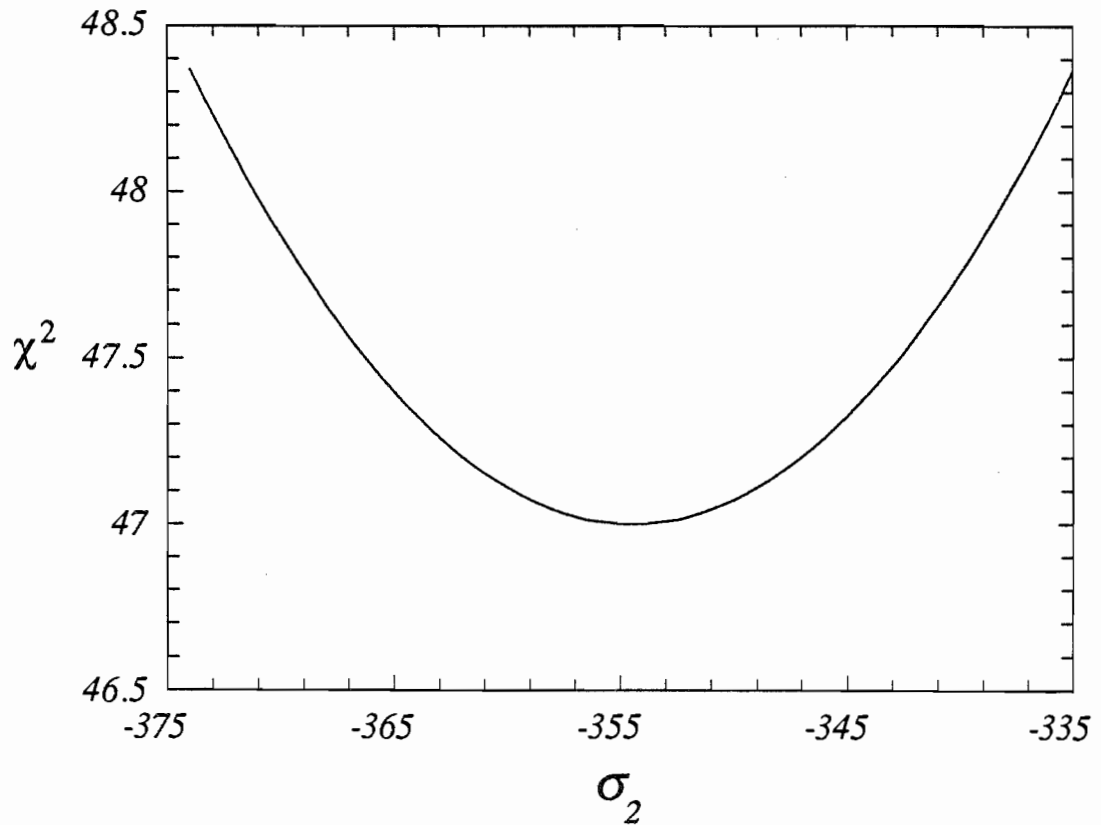


Figure 3.11: The dependence of the goodness of fit, χ^2 , on the coefficient σ_2 . The determination of σ_2 and its uncertainty follows that for extracting ϕ .

Table 3.1: Experimental parameters for the four measurements of $\sigma_2(E)$.

Incident Neutron Energy (MeV)	Degree of Alignment	Number of Runs Used	Angle Sequence	
			Limits	Increment
1.47	47%	61	$\pm 90^\circ$	30°
1.84	67%	49	$\pm 90^\circ$	45°
1.92	65%	132	$\pm 135^\circ$	45°
3.88	60%	42	$\pm 90^\circ$	45°

Table 3.2: Results of σ_2 measured as a function of incident neutron energy. The geometric σ_2 are seen to be consistent with zero and are not incorporated in σ_2 .

Neutron Energy (MeV)	σ_2 (millibarns)	geometric σ_2 (millibarns)
1.47	-548 ± 42	4 ± 21
1.84	-354 ± 17	14 ± 13
1.92	-283 ± 23	—
3.88	$+248 \pm 23$	-1 ± 10

sign as evident in the table. The mean thickness of the cylindrical target was $5.78 \times 10^{-5} \text{ mb}^{-1}$ from the discussion in appendix 8.1. In each case a σ_2 was extracted from the corresponding set of data for an unaligned target (no such set was accumulated for the 1.9 MeV FC measurement.) These “warm” σ_2 may be non-zero due to geometric effects such as wobble in rotating the target or deviations from a cylindrical shape. Such effects would add a systematic error to the true σ_2 . However, as per the previous discussion of the holmium target, geometric effects were predicted to be negligible. Indeed, the warm σ_2 are well within one sigma of zero in two out of three cases. Therefore, geometric effects are taken to be zero, and are *not* incorporated in the tabulated values of σ_2 . The uncertainties in the table represent one-sigma errors. The statistical errors in these four points are actually quite small. It is the random error contributed by variations in yield with repeated sampling caused by phototube gain drifts that prevents these uncertainties from being smaller.

The deformation effect in ^{165}Ho has been measured previously, but only by comparing neutron transmission through an oriented and an unoriented target (Fasoli 1973, Marshak 1970, McCarthy 1968, Fisher 1967, Marshak 1966, and Wagner 1965). Use of a rotating aligned target permits us to view the mass deformation of the holmium nucleus through different axes. Such use also permits testing for higher order alignment through positional dependence rather than temperature dependence. We report the effect in terms of a quantity σ_2 independent of the degree of alignment. Previous measurements must be renormalized to compare to the present values. Such renormalization means dividing out the percentage of orientation attained. It also requires a factor of $-1/2$ depending on whether the mass deformation was parallel to or perpendicular to the incident neutron beam. (Some experiments used a polarized target, where a small magnetic field is applied in the crystalline a - b plane. In these cases the semi-major axis of the mass deformation was in the a - b plane—perpendicular to the c -axis.) The present results are plotted against past measurements in figure 3.12. Two

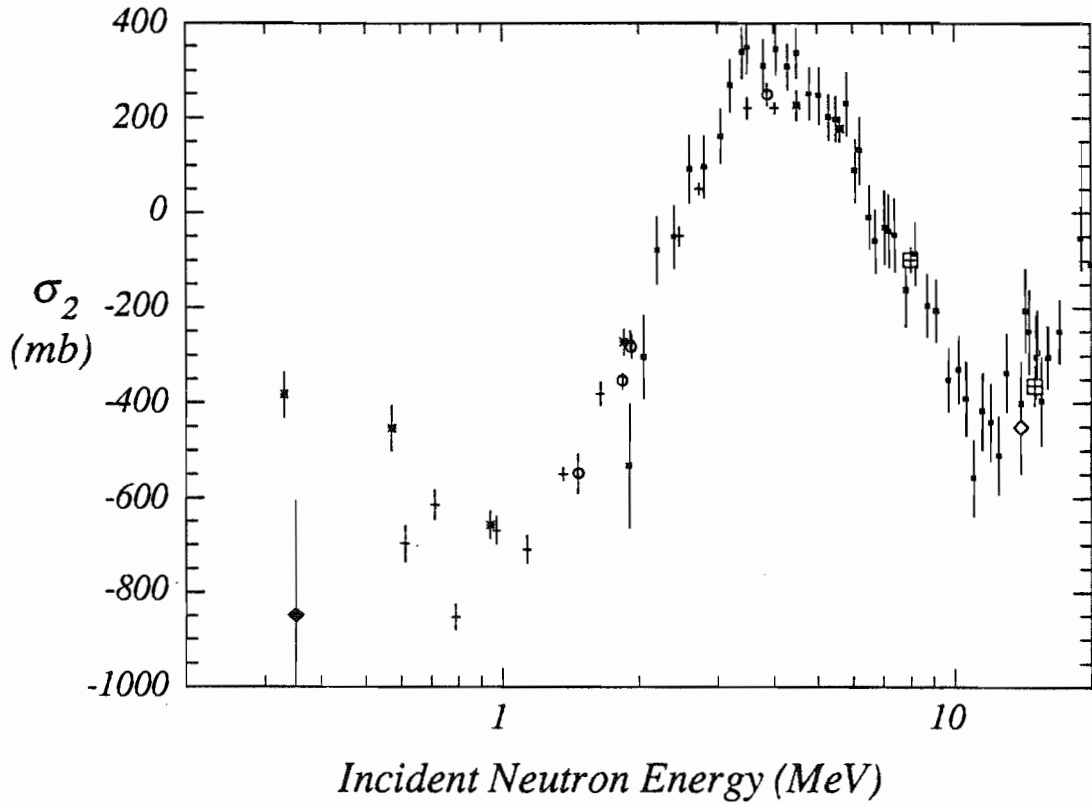


Figure 3.12: Different sets of $\sigma_2(E)$. Key: open circles-present data; crosses-Fasoli 1973; closed squares-Marshak 1970; asterisks-McCarthy 1968; crossed-box-Fisher 1967; open diamond-Marshak 1966; closed diamond-Wagner 1965.

other data sets extensively overlap the energy range covered here. The present data is systematically greater in amplitude than the data of Fasoli, et. al. (1973), although the difference may not be statistically significant. Our data is smaller in amplitude than that of Marshak, et. al. (1970). Indeed, the latter set is the largest in magnitude of all sets, below 6 MeV.

Overall, the agreement between this data and previous data is excellent. This is true even though the present measurement utilized a novel rotating target. These results imply that suppositions made about the holmium target alignment—its direction and reproducibility and its magnitude—and target thickness are quite appropriate. Such independent characterization is essential in interpreting the five-fold correlation measurement that follows.

Chapter 4

COUPLED CHANNELS CALCULATION OF DEFORMATION EFFECT

The nuclear deformation effect in the neutron total cross section (chapter 3) can be understood from the non-spherical shape of a ^{165}Ho nucleus. This effect can be calculated with the deformed optical model (DOM), where deformed potentials reflect the non-spherical density distribution within the nucleus. The calculation is presented in this chapter using statistical tensor formalism. The procedure is laid out in section 4.1. Results of the calculations are presented in section 4.2. Lastly, the deformation parameters which reproduce the deformation effect are compared to parameters in the research literature.

4.1 FORMALISM

The deformation effect cross section σ_2 is a term accounting for varying diameters in a deformed nucleus which is added to the σ_{00} cross section for an unoriented

target (chapter 3). From equations 3.4 and 3.6, σ_2 is given by

$$\sigma_K = \text{Re}\{2\pi\lambda^2 \hat{K} t_{K0}^*(I) \sum_J g_J \sum_{l'l_j} T_{K0K}(l'j'l_j) [\delta_{ll'} \delta_{jj'} - S_J(lj \rightarrow l'j')]\} / t_{K0} \quad (4.1)$$

with $K = 2$. Here T_{K0K} is given by equation 6.3 (with $k = 0$):

$$T_{K0K}(l'j'l_j) = (-1)^{j-j'} \hat{l}_j \hat{l}_{j'} \langle lK00 | l'0 \rangle W(JjIK; Ij') W(j'l'jl; sK) \quad (4.2)$$

Previous calculations (Fasoli 1978, Marshak 1970) compared σ_T in the two cases of nuclear orientation in a particular direction and random orientation. A deformed optical model calculation yields the s-matrix elements S_J , with the coupled channels (Tamura 1965) code ECIS (Raynal 1970). Young, et. al. (1983) have found deformed optical model parameters for ^{165}Ho and ^{169}Tm which reproduce s- and p-wave neutron strength functions, total cross sections, and angular distributions. The local parameter set for neutrons on holmium (similar to Set I in Young (1983)) is used (table 4.1). The first two excited states in ^{165}Ho are coupled explicitly to

Table 4.1: Parameters for the deformed optical model calculation. Potentials are volume, surface imaginary, volume imaginary, and spin-orbit. Wood-Saxon form factors are used.

Potential strength (MeV)	Radius (fm)	Diffuseness (fm)
$V = 49.8 - 16 \frac{N-Z}{A} - 0.325E$	1.26	0.63
$W_D(E \leq 6.5) = 5.0 - 8 \frac{N-Z}{A} + 0.51E$	1.26	0.48
$W_D(E > 6.5) = 8.3 - 8 \frac{N-Z}{A} - 0.09(E - 6.5)$	1.26	0.48
$W_V(E \leq 9.0) = 0.$	1.26	0.63
$W_V(E > 9.0) = -1.8 + 0.2E$	1.26	0.63
$V_{SO} = 6.0$	1.26	0.63

the ground state. Imaginary potentials account for coupling to all other states. Some practical details on the computer codes are given in appendix 8.2.

The shape deformation is characterized by the radius

$$R(\theta) = r_0 A^{1/3} \left(1 + \sum_{\lambda=2,4,6,\dots} \beta_\lambda Y_{\lambda 0}(\theta) \right). \quad (4.3)$$

Here $Y_{\lambda 0}$ are spherical harmonics. The deformation parameters β_λ are equivalent to the β'_λ defined in Löbner (1970), who review the common definitions for shape deformation. As in Bengtsson (1989) the odd order β_λ are assumed to be zero and the nuclear shape is reflection symmetric with respect to the plane perpendicular to the axis of symmetry. The assumption of axial symmetry is common in this mass region (Nazarewicz 1990).

Deformation parameters are of current interest in the study of neutron vs. proton distributions within nuclei. For example, Knudson, et. al. (1990) have determined that the quadrupole deformation of the neutron density is 84% of the proton quadrupole deformation—deformed Hartree-Fock calculations yield neutron and proton distributions in much better (96%) agreement (Bartel 1989). Systematic deformations for the even-even rare earth nuclei are calculated with so-called macroscopic-microscopic methods which combine liquid-drop models and shell model corrections (e.g. Nazarewicz 1990). A very recent review of such activity is provided by Jain (1990).

Following Glendenning (1968), the optical model parameters are fixed in the present calculation and the deformation parameters are varied; the final β_λ are those which result in the best fit to the experimental $\sigma_2(E)$. Moreover the calculations are constrained by simultaneously fitting the total cross section σ_0 .

4.2 RESULTS

The quadrupole and hexadecapole deformations $\beta_2 = 0.30$ and $\beta_4 = -0.02$ in Young's parameter set were the starting points of the calculation. The dependence $\sigma_2(\beta_2)$ was determined at 3.9 MeV (figure 4.1). For small β_2 ($|\beta_2| \leq 0.1$) the dependence is linear. However, for the large β_2 of holmium, σ_2 is quite non-linear,

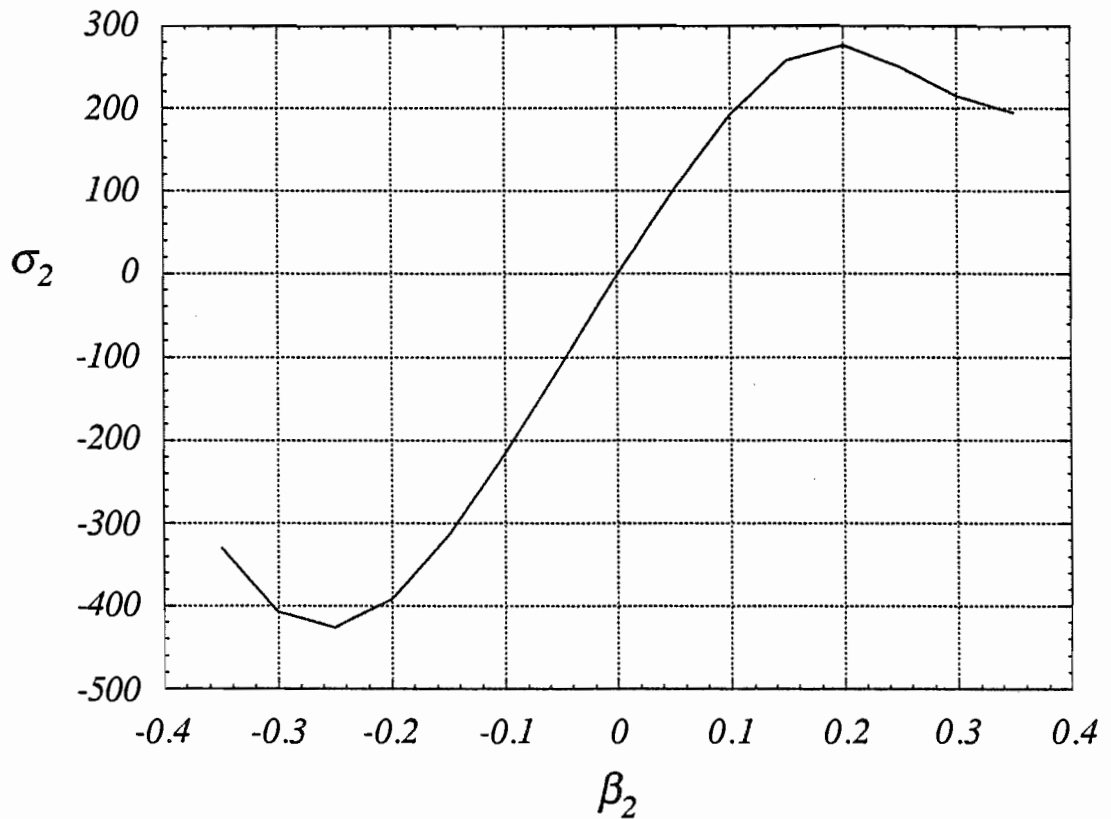


Figure 4.1: The dependence of σ_2 on β_2 at 3.9 MeV. Here $\beta_4 = -0.02$. The cross section is proportional in magnitude and sign to β_2 only from $|\beta_2| \leq 0.1$.

turning toward zero as β_2 increases. Moreover for large β_2 , changing the sign does not simply change the sign of σ_2 .

Table 4.2 summarizes the results of the calculations at 3 and 5 MeV. The

Table 4.2: Lowest order cross section terms as a function of individual deformations. Neutron energy is in MeV. All cross sections are in millibarns.

Energy	σ_K	All $\beta_K = 0$	$\beta_2 = 0.1$	$\beta_4 = 0.1$	$\beta_6 = 0.1$
3.0	σ_0	6952	6825	6953	6978
	σ_2	0	112	-5	1
	σ_4	0	-2	81	1
	σ_6	0	0	0	0
5.0	σ_0	5230	5300	5282	5299
	σ_2	0	159	-14	2
	σ_4	0	9	47	0
	σ_6	0	0	0	-6

σ_K are tabulated for each unique deformation β_λ . While σ_K is seen to be most sensitive to $\beta_{\lambda=K}$, it can also be affected by other β_λ through two-step coupling—the correspondence $K \leftrightarrow \lambda$ is not one-to-one. For example, β_4 contributes 9% to σ_2 at 5 MeV. Previous experiments did not include a hexacontatetrapole deformation β_6 although a small value was found helpful in reproducing α -scattering data (Hendrie 1968) on even-even rare earth nuclei and neutron scattering on tungsten isotopes (Delaroche 1982). The present calculations include β_6 ; it is seen to have little more than a percent effect on the tabulated cross sections.

The calculations are fit to both total cross section σ_0 and deformation cross section σ_2 , in the energy range 1–20 MeV, using steps of 1 or 2 MeV. Young, et. al. (1983) fitted the total cross section down to 0.1 MeV, but the σ_2 data are very scattered below 1 MeV (figure 3.12). The experimental total cross sections are

taken from McLane (1988); the experimental σ_2 are referenced in chapter 3 and include the TUNL data. The reduced chi-square is calculated,

$$\chi_\nu^2 = \frac{1}{N(E) - 2} \sum_{N(E)} \left(\frac{\sigma_K^{calc}(E) - \sigma_K^{exp}(E)}{\delta_K^{exp}(E)} \right)^2, \quad (4.4)$$

separately for σ_0 and σ_2 , and for them combined. The weightings δ_0^{exp} of the total cross section are taken to be uniformly 50 mbarn— thus the value of χ_ν^2 is important only relative to that from another β_λ set.

The calculation of the form of $\sigma_2(E)$ with a quadrupole deformation alone is rather good (figure 4.2). The discrepancy is a shift to higher energy at 2–4 MeV. Using a hexadecapole deformation in the calculation improves the agreement with σ_2 somewhat but worsens the agreement with the total cross section (figure 4.3). Addition of a hexacontatetrapole deformation improves the calculated σ_2 even more and provides a fit to σ_0 as good as the original fit for β_2 alone. The total reduced chi-square is cut almost in half compared to using β_2 alone. The minimizing β_4 is unaffected by β_6 but β_2 is reduced. If the calculated σ_2 was forced to shift toward lower energy (to improve the fit), the calculation did not reproduce the total cross section well. This behavior is reminiscent of the adiabatic coupled channels calculation presented by Marshak, et. al. (1970), in which σ_2 is shifted to lower energies (beyond even the data) and the total cross section is too large in the energy region 6 to 20 MeV. The present calculation better agrees overall with the data.

The final set of deformation parameters determined from σ_2 and σ_0 and the coupled channels calculation is $\beta_2 = 0.29$, $\beta_4 = -0.02$, and $\beta_6 = 0.08$. The reduced radius in the optical model parameter set is 1.26 fm. The deduced shape $R(\theta)$ (equation 4.3) of the holmium nucleus is plotted in figure 4.4 using these values.

The uncertainties in the best-fit set β_λ are the amounts of shift in β_λ which double the reduced chi-square fit. This determination is equivalent to equation 3.16. The results are tabulated in 4.3. The fit of the calculated σ_2 and σ_0 is unfortu-

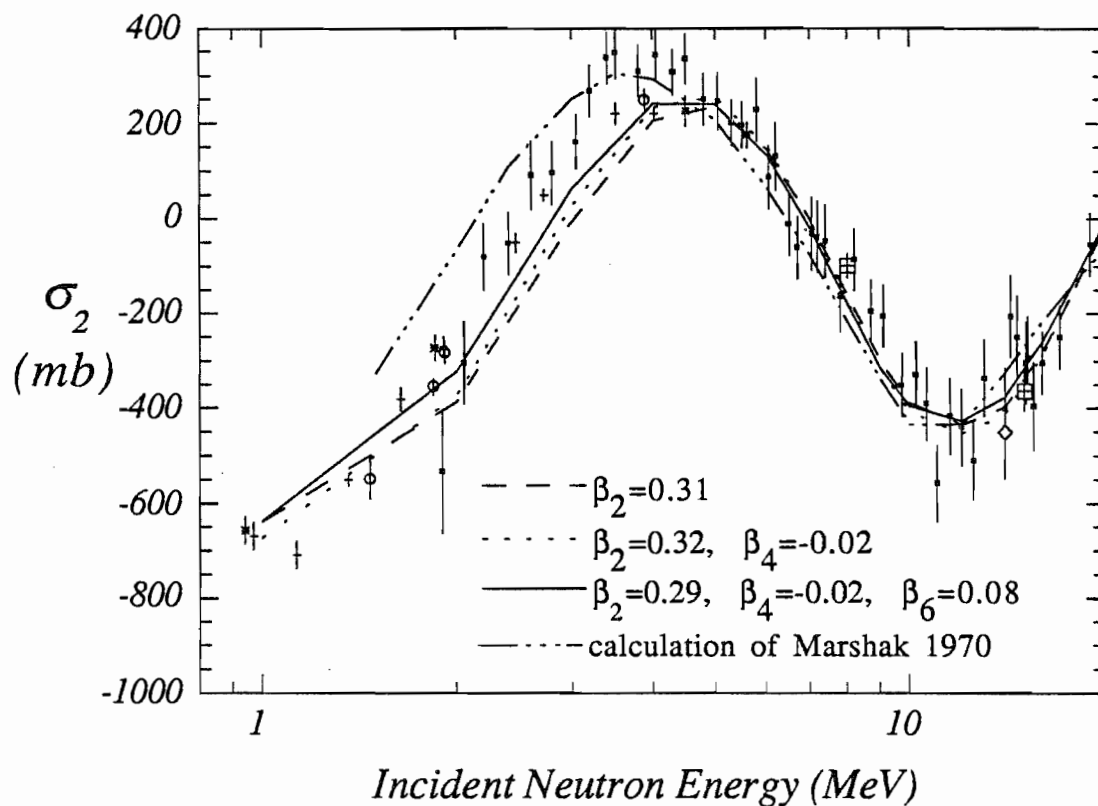


Figure 4.2: The calculated energy dependent σ_2 and experimental data. The data key is identical to figure 3.12. For comparison, the calculation in Marshak (1970) is also shown.

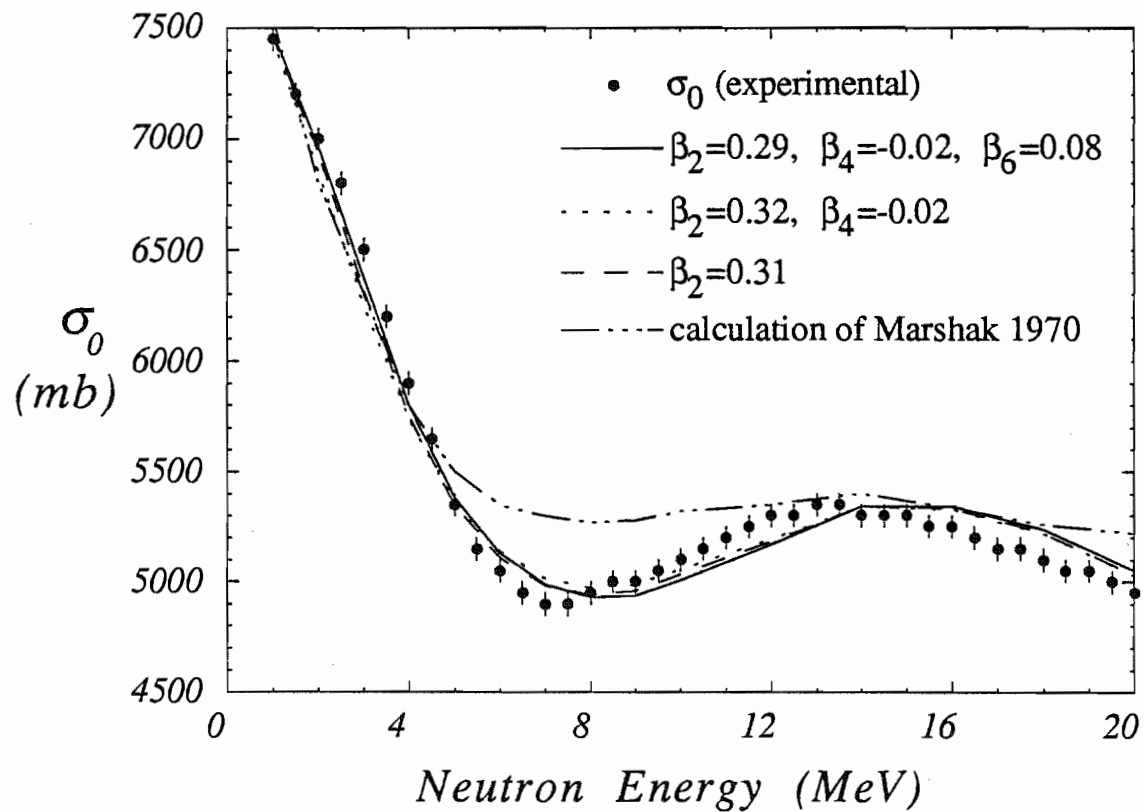


Figure 4.3: The calculated energy dependent σ_0 and experimental data.

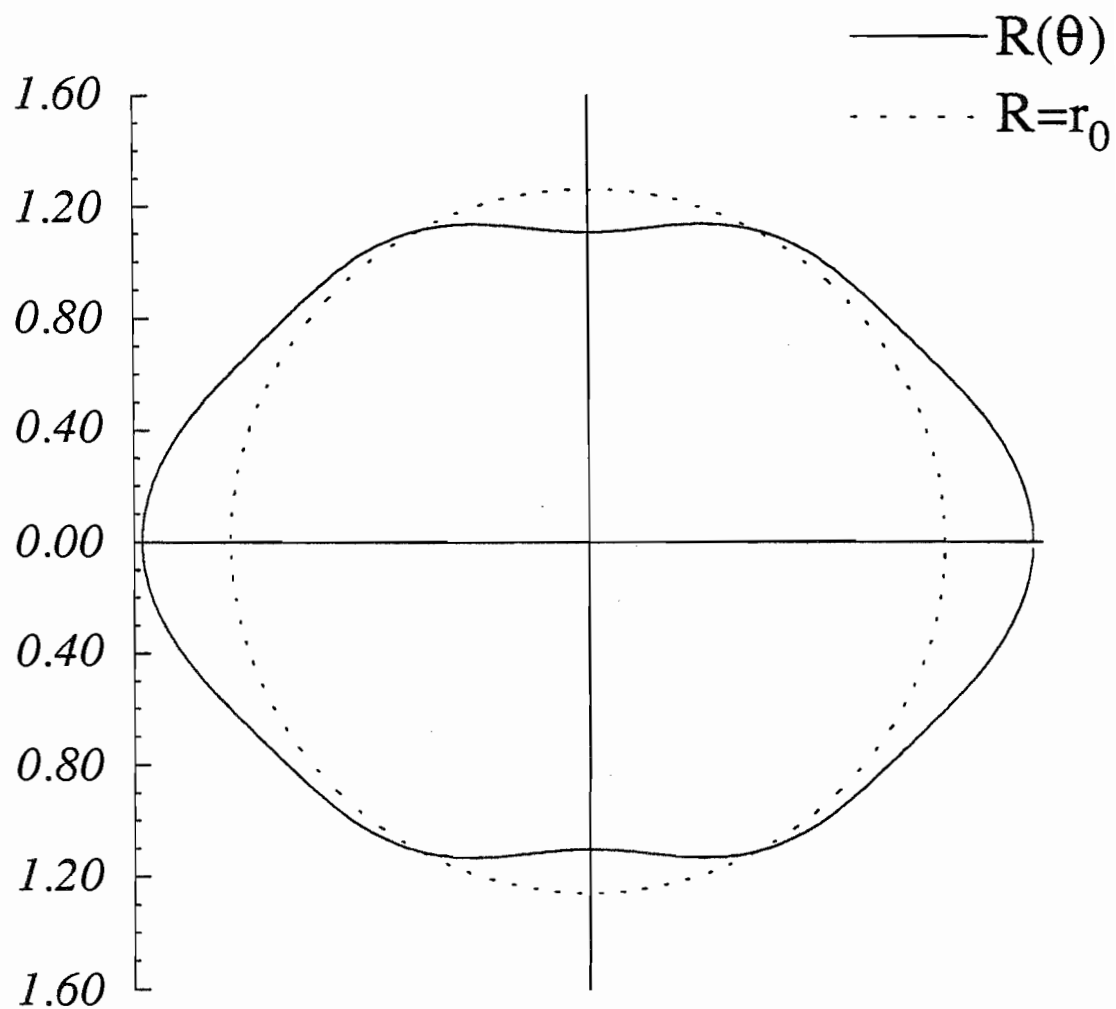


Figure 4.4: Deduced shape of a ^{165}Ho nucleus. The scale is given on the left in fm . The deformed radius is with the deformation parameters extracted in the present calculation. For comparison, a spherical nucleus with identical r_0 is drawn with a dotted line.

Table 4.3: Deformation parameters extracted from experimental σ_2 in the present calculation. The associated reduced radius is 1.26 *fm*.

β_2	$0.29^{+0.055}_{-0.050}$
β_4	$-0.02^{+0.050}_{-0.055}$
β_6	$0.08^{+0.15}_{-0.09}$

nately not very sensitive to the deformation parameters. Measurement of $\sigma_4(E)$ is feasible with a colder holmium target; the corresponding calculations of σ_4 within the present framework might help reduce the uncertainties in the extracted deformation parameters.

4.3 COMPARISON TO OTHER DEFORMATION PARAMETERS

The deformations considered in this chapter occur in the optical model potential and reflect mass deformation or nucleon density distribution in the ^{165}Ho nucleus. This is what the neutron projectile probes in the present experiment (chapter 3). Parameters deduced in other experiments often arise from electromagnetic interaction experiments sensitive to the nuclear charge distribution (or proton distribution and a proton's charge distribution.) However, the relation of the mass deformation to the charge deformation is model-dependent and so mass deformation parameters inferred from such experiments are less certain. We also note that cross sections scale with the deformation *lengths* $\beta_\lambda r_0$, so that relative values of the reduced radius r_0 must also be considered when comparing deformation parameter sets. The different results for $\beta_\lambda r_0$ are tabulated (table 4.4) for holmium, along with results in neighboring nuclei from nuclear scattering. After searching on β_λ in the present calculation, β_2 and β_4 are almost identical to

Table 4.4: Sets of deformation parameters for $A \approx 165$. The source key is: n - nuclear scattering, em - electromagnetic experiment, c - calculation. Knudson's (1990) conversion factor from charge to matter deformation has been applied; the other *em* values are uncorrected. The two sets of Bartel (1989) arise from different interaction models.

nucleus	$\beta_2 r_0$	$\beta_4 r_0$	$\beta_6 r_0$	source	reference
^{165}Ho	0.37	-0.025	0.101	n	present experiment
	0.30			em	Knudson 1990
	0.38	-0.025		n	Young 1983
	0.36	0.04		em	Powers 1975
	0.400			n	Marshak 1970
	$0.324r_0$			em	Löbner 1970
	0.377	0.011		c	Nazarewicz 1990
	0.376	0.026		c	Bartel 1989
	0.356	0.024		c	Bartel 1989
^{162}Dy	0.33	0-0.02		n	Trautner 1973
^{166}Er	0.343	0.0	-0.007	n	Aponick 1970
	0.331	0.0	-0.022	n	Hendrie 1968

the values of Young (1983). Another experimental β_2 (Powers 1975) is also very close. The recent value of Knudson (1990) is much lower, but the discrepancy is introduced by their small ratio of mass to charge deformation. Model calculations use values of β_2 that are very similar to ours. The values of β_4 are more dispersed, perhaps because mass systematics indicate that β_4 passes through zero at mass $A = 165$. The other values of β_4 are small and positive—although the experimental value (Powers 1975) has an uncertainty of 50%. Moreover, all the systematic studies have been done on even-even nuclei, but Delaroche (1981) has found that β_4 for the odd- A ^{183}W is 40% larger than those for the even- A tungsten isotopes. It is not clear how the odd- A ^{165}Ho is expected to follow even- A systematics. Therefore β_4 is not well-known and the present negative value is not in striking disagreement. When considered, β_6 has been small and negative (see also Delaroche 1982) and has never been applied to ^{165}Ho . The uncertainty in the value of Aponick, et. al. is 100%. The value extracted here is positive and comparatively large but its uncertainty is also large so that it is not significantly different statistically from previous values. Moreover β_6 may differ systematically between odd- and even- mass nuclei as suggested for β_4 , so comparisons among different β_6 are difficult.

4.4 DISCUSSION

The present calculation extends previous work by consideration of experimentally determined σ_2 using deformations up through hexacontatetrapole. The calculation is performed with the degrees of orientation of the target expressly removed. Deformation parameters were extracted as free parameters by fitting the calculated cross-sections to experimental data. The resulting fits are improved over previous calculations of σ_0 and σ_2 (Marshak 1970). We expect to produce better fits by varying the other optical model parameters. The deformation parameter β_2 deduced is in good agreement with previous measurements. Inclusion of β_4

and β_6 improved the fits. The value for β_4 disagrees mildly with previous values, but the uncertainty is large. It is difficult to draw a conclusion on β_6 , where the uncertainty is large and no previous value for ^{165}Ho is available. The present calculation appears to provide an accurate determination of deformation parameters, but with less precision than fits to differential cross sections. The use of β_6 may be sensitive to the number of states explicitly coupled. Such sensitivity can be explored, but the particular codes used here become inefficient for such large angular momentum couplings to the high-spin holmium ground state. At present, the effects due to β_6 are found to be unimportant, so future computations will instead explore the influence of other optical model parameters.

Chapter 5

POLARIZED BEAM APPARATUS

Much of the equipment necessary for a measurement of the five-fold correlation is also used in the deformation effect measurements and is described in chapter 2. The apparatus unique to the FC experiment is described in this chapter. The new features relate to the production and monitoring of the polarized neutron beam. A more detailed description of data acquisition on the VAX 11/780 is also given.

5.1 PREPARATION OF POLARIZED BEAM

The time-reversal experiment requires a polarized neutron beam which is produced by polarization transfer in the $T(\vec{p}, \vec{n})$ reaction. The polarization transfer coefficient at 0° is 0.62 (Simmons 1973) for 3.2 MeV protons (with 1.9 MeV neutrons in the forward direction.) The polarized proton beam is obtained from the TUNL Atomic Beam Polarized Ion Source (ABPIS, figure 5.1). The ABPIS was brought on-line in 1989; the FC measurement was the first experiment to utilize it and a brief summary of its operation is given here. For a more complete description see Clegg (1989) or recent TUNL Annual Reports.

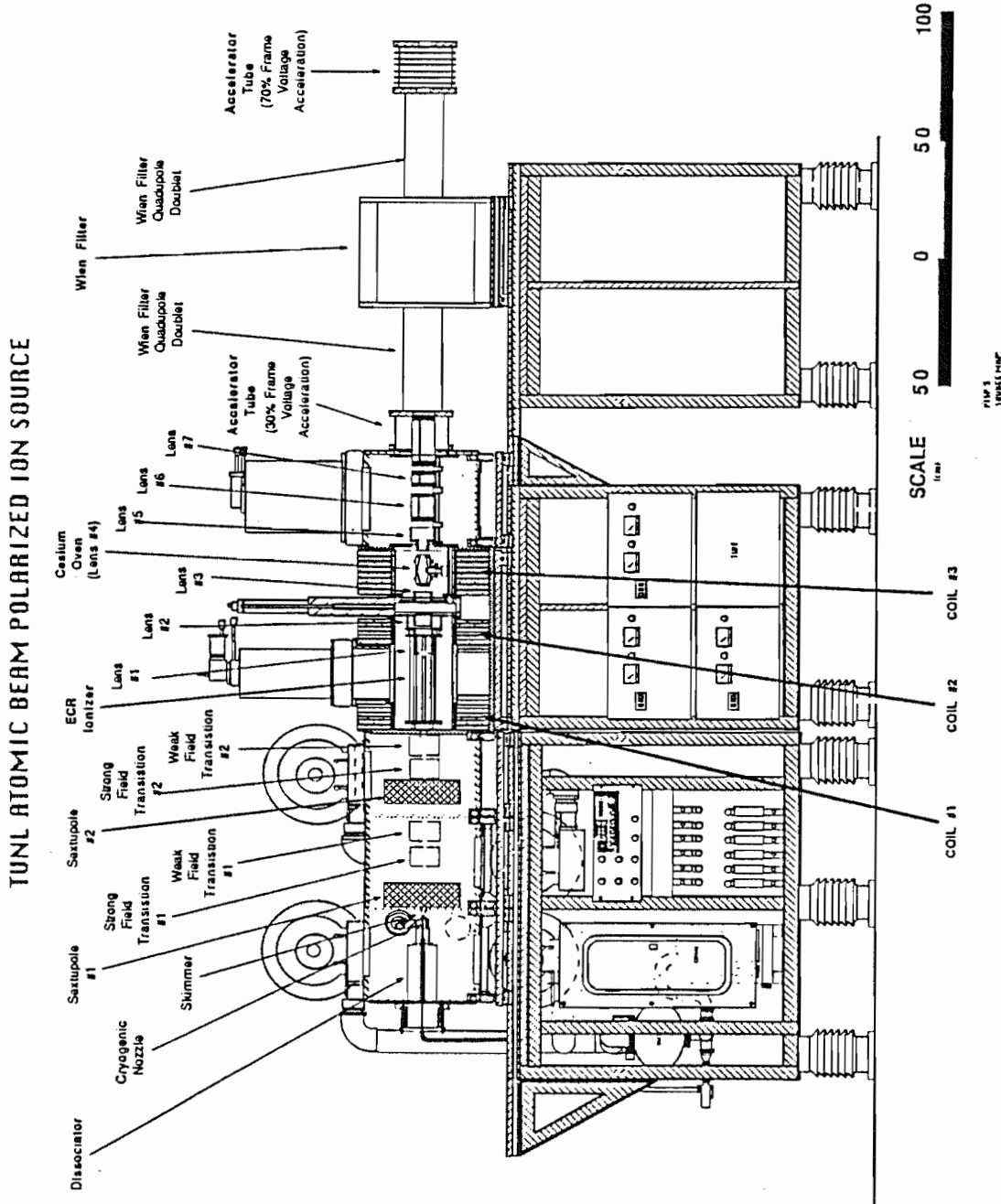


Figure 5.1: TUNL Atomic Beam Polarized Ion Source.

The atomic beam source consists of a gas dissociator and a system of magnets and radio-frequency cavities. Gaseous H_2 is injected into a water-cooled pyrex tube where the gas is dissociated by a 200W discharge. Emerging atoms are slowed upon drifting through a 30 K copper nozzle. An aperture defines the beam prior to its entrance axially into a tapered sextupole magnet. The sextupole field focuses atoms in one atomic spin state while defocusing atoms in the other. The induced electronic polarization of the beam is transferred to the nuclei in the subsequent radio-frequency (RF) transition units. For hydrogen source gas there are two of these cavities. Each cavity contains an oscillating magnetic field within a static external field. One cavity has RF fields chosen to drive one atomic transition; the other cavity produces a complementary transition. The resultant nuclear polarization can be either parallel or antiparallel to the beam axis depending on which RF cavity is energized.

The next function of the ABPIS is to turn the atomic beam into an ion beam. The electron is stripped away from each H atom in an electron-cyclotron resonance (ECR) ionizer. The ECR ionizer holds a magnetically contained plasma of electrons in a nitrogen buffer gas. An electrode extracts the subsequent polarized hydrogen ions. As discussed in section 2.4, a negatively charged beam must be supplied to the tandem Van de Graaff. The necessary two-electron transfer to the protons is accomplished by collisions with cesium vapor in a cesium oven. The oven is carefully designed to minimize escape of the cesium vapor into the vacuum cavity. The oven is also biased to aid in extracting the ion beam.

The emerging H^- beam is polarized longitudinally—that is, along the beam momentum. The final function of the ABPIS is to precess this polarization to the direction required by the experiment. The Wien-filter spin precessor rotates the quantization axis to the desired position with an electromagnet, while electrostatic plates keep the beam undeflected. The FC experiment is performed with the holmium target alignment axis in the horizontal plane (as for the deformation effect measurements.) Therefore sensitivity to an FC is maximized by a vertically

polarized beam. The proton beam is so polarized by precessing the proton spins 90° out of the horizontal plane using the Wien filter. The spins thereafter are not precessed by the subsequent bendings of the beam in the horizontal plane. Before reaching the tandem, the polarized beam proceeds through a 30° bending magnet which deflects other ionic species out of the beam.

The polarized H^- beam is accelerated to 50 keV upon leaving the high-voltage deck of the ABPIS, then enters the Van de Graaff. The emerging proton beam bends through the 59° analyzing magnet and then impinges on the tritiated foil.

5.2 MONITORING OF POLARIZED BEAM

Vertically polarized protons incident on tritium will produce neutrons unequally at an angle Θ to the left and to the right of the beam axis. The analyzing power A_y is defined as this relative difference in intensity,

$$A_y(\Theta) \equiv \frac{I(-\Theta) - I(\Theta)}{I(-\Theta) + I(\Theta)} \frac{1}{p_y}, \quad (5.1)$$

where p_y is the vertical component of the proton polarization. A_y has a maximum at $\Theta \sim 40^\circ$ lab angle for 2.26 MeV protons (Donoghue 1976). Inverting A_y and p_y in this definition permits continuous proton polarization monitoring in the following manner.

Adapting the notation of Haight (1972), the number of neutrons counted in a detector at angle Θ with respect to the incident beam is given by

$$N_j(\Theta_j) = I_0(\Theta_j)[1 + p_y A_y(\Theta_j)] \epsilon_j \quad (5.2)$$

where I_0 is the neutron intensity at angle Θ_j for an unpolarized incident proton beam and ϵ_j is the product of the detector efficiency and solid angle. A detector mounted on the "left" of the beam is represented by $j = L$. A detector placed beam-right is denoted by $j = R$. The counts N_j must be normalized to the amount of proton beam current on the T_1T_2 foil. The quantities ϵ_L and ϵ_R need

not be equal—the proper p_y can still be extracted by reference to an unpolarized beam. The left detector records counts per unit beam current $N_L^0 = I_0(\Theta_L)\epsilon_L$ for an unpolarized beam. Define

$$L \equiv N_L/N_L^0 = 1 + p_y A_y(\Theta_L), \quad (5.3)$$

and define R similarly for the right detector. Then

$$\frac{L - R}{L + R} = \frac{p_y[A_y(\Theta_L) - A_y(\Theta_R)]}{2 + p_y[A_y(\Theta_L) + A_y(\Theta_R)]}. \quad (5.4)$$

If $\Theta_L = \Theta_R$ then $A_y(\Theta_L) = -A_y(\Theta_R) \equiv A_y$ and

$$\frac{L - R}{L + R} = p_y A_y. \quad (5.5)$$

If $\Theta_L \simeq \Theta_R$ only so that $A_y(\Theta_L) = -A_y(\Theta_R) - 2\Delta A_y \equiv A_y$, then

$$\frac{L - R}{L + R} = \frac{p_y(A_y + \Delta A_y)}{1 - p_y \Delta A_y} \simeq p_y(A_y + \Delta A_y). \quad (5.6)$$

This is the more realistic case—however Θ_L and Θ_R are within a couple of degrees of each other and the resultant difference ΔA_y is well within the experimental error of several percent, δA_y . Then from equation 5.5,

$$p_y = \frac{L - R}{L + R} \frac{1}{A_y}, \quad (5.7)$$

with error propagation dictating an uncertainty in p_y given by

$$(\delta p_y)^2 = \left[\frac{2}{(L + R)^2} \right]^2 [(R\delta L)^2 + (L\delta R)^2] + \left(\frac{p_y}{A_y} \delta A_y \right)^2. \quad (5.8)$$

The uncertainties δL and δR can be taken from statistical errors in the respective $N_j^{[0]}$.

To carry out this program of measuring p_y , two neutron detectors are mounted in the horizontal plane at $\pm 45^\circ$ with respect to the beam (Figure 5.2). The detectors are 2 inch diameter by 2 inch long liquid scintillators (Bicron BC-501) mounted on Hamamatsu PMT's. Pulse shape discrimination is used as for the 0° detector to distinguish neutron triggers from gamma ray events. The detectors are unshielded. No change was observed in the neutron count rate when the aligned target was rotated.

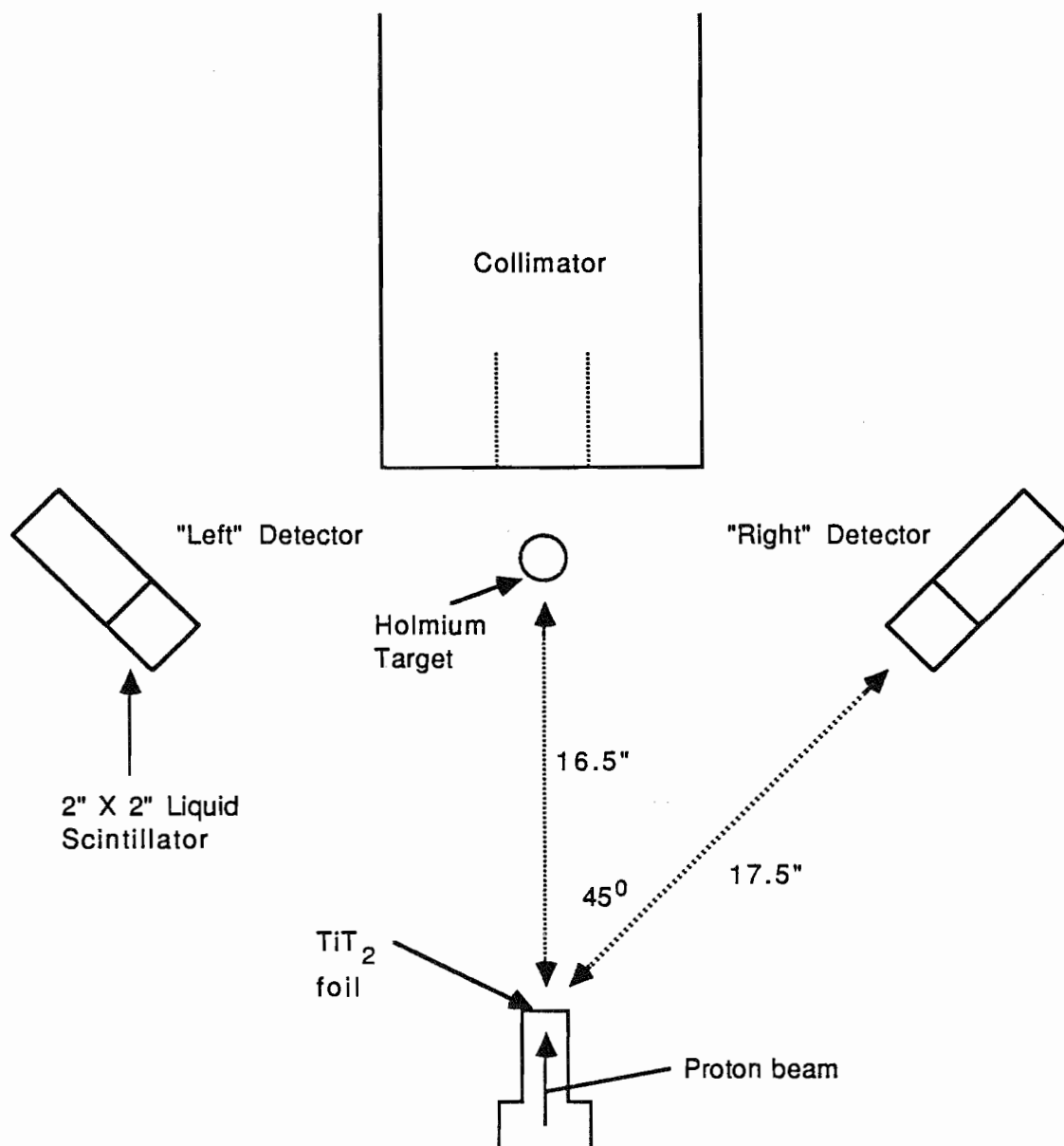


Figure 5.2: Polarimeter for continuous monitoring of proton polarization. The non-zero analyzing power of $T(\vec{p}, \vec{n})$ is used to infer p_y . The view here is from above.

5.3 FAST SPIN-FLIP

The RF transition cavities discussed in section 5.1 can be turned off and on at rates of up to ~ 1 kHz. Toggling between the weak magnetic field (WF) and strong field (SF) units produces beam with polarization alternating between *up* and *down*. The toggling rate is selected with a pulser in the control room. A practical limit on the spin flipping rate is determined by the finite amount of time between setting an RF cavity and delivering the resultant beam to the holmium target. This time delay is due largely to the slow drift of the ~ 35 K atomic beam from the transition units to the end of the ABPIS high voltage deck. The total transit time is conservatively calculated to be ≈ 4 msec. Too much time is spent waiting for a new spin state if the flipping frequency is of order 100 Hz or more. Thus a 10 Hz pulser is used and the beam spin is therefore *up* for 100 milliseconds and then *down* for 100 msec.

Systematic errors may be present due to changing yields, independent of the spin-flip rate. These are reduced by the choice of spin state sequencing. For example, suppose the normalized yield is monotonically decreasing (perhaps due to a slow gain drift, or a decaying beam current coupled with poor dead-time correction.) An equal number of + or *up* and - or *down* spin states must be used. But each - state has fewer counts than the + spin state that precedes it, resulting in a false spin asymmetry. To avoid this type of error, the +- sequence is repeated, but inverted: + - - +. In fact, to cancel the error to second order the inverted four spin state cycle is also repeated. Consider the yield $N(t)$ as a function of time in figure 5.3. A raw asymmetry ϵ_i is formed from the span of eight spin states between times t_i and t_{i+1} . Each spin state is of duration Δ . The raw asymmetry is the relative difference between the total number of counts accumulated for spin *up* and spin *down*. Assuming the eight intervals correspond to + - - + - + + -,

$$\epsilon_i \equiv \frac{\int_{t_i}^{t_i+\Delta} N dt + \int_{t_i+3\Delta}^{t_i+4\Delta} N dt + \int_{t_i+5\Delta}^{t_i+7\Delta} N dt - \int_{t_i+\Delta}^{t_i+3\Delta} N dt - \int_{t_i+4\Delta}^{t_i+5\Delta} N dt - \int_{t_i+7\Delta}^{t_i+8\Delta} N dt}{\int_{t_i}^{t_i+\Delta} N dt + \int_{t_i+3\Delta}^{t_i+4\Delta} N dt + \int_{t_i+5\Delta}^{t_i+7\Delta} N dt + \int_{t_i+\Delta}^{t_i+3\Delta} N dt + \int_{t_i+4\Delta}^{t_i+5\Delta} N dt + \int_{t_i+7\Delta}^{t_i+8\Delta} N dt} \quad (5.9)$$

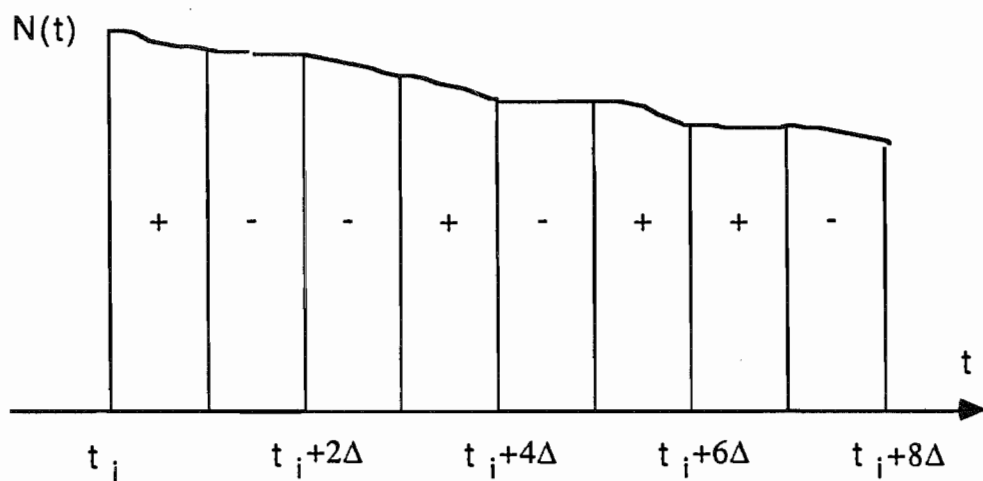


Figure 5.3: The effect of monotonic change in detector yield with time.

Inverting the negative terms and reordering,

$$\epsilon_i = \frac{\int_{t_i}^{t_i+\Delta} N dt + \int_{t_i+3\Delta}^{t_i+\Delta} N dt + \int_{t_i+3\Delta}^{t_i+4\Delta} N dt + \int_{t_i+5\Delta}^{t_i+4\Delta} N dt + \int_{t_i+5\Delta}^{t_i+7\Delta} N dt + \int_{t_i+8\Delta}^{t_i+7\Delta} N dt}{\int_{t_i}^{t_i+8\Delta} N dt} \quad (5.10)$$

A Taylor series expansion is used,

$$F(t_i + \Delta) \equiv \int_{t_i}^{t_i+\Delta} N(t) dt = \sum_{j=0} \frac{\Delta^j}{j!} F^{(j)}(t = t_i) \quad (5.11)$$

where $F^{(j)}(t = t_i)$ is the j th derivative of F evaluated at t_i . Then

$$\begin{aligned} \epsilon_i = & [2F(t_i + \Delta) + 2F(t_i + 4\Delta) + 2F(t_i + 7\Delta) - F(t_i) - 2F(t_i + 3\Delta) \\ & - 2F(t_i + 5\Delta) - F(t_i + 8\Delta)]/[F(t_i + 8\Delta) - F(t_i)]. \end{aligned} \quad (5.12)$$

Evaluated to lowest order in Δ ,

$$\begin{aligned} \epsilon_i = & \frac{-4\Delta^4 F^{(4)}(t_i)}{4\Delta F^{(1)} + 16\Delta^2 F^{(2)} + \frac{128}{3}\Delta^3 F^{(3)} + \frac{256}{3}\Delta^4 F^{(4)}} \\ = & \frac{-\Delta^3 N^{(3)}(t_i)}{N + 4\Delta N^{(1)} + \frac{32}{3}\Delta^2 N^{(2)} + \frac{64}{3}\Delta^3 N^{(3)}} \end{aligned} \quad (5.13)$$

For example, if the yield $N(t)$ is well represented by a quadratic polynomial, the spin asymmetry in this scheme is zero. Thus the beam polarization is set in an eight-spin-state sequence $+ - - + - + + -$.

5.4 VAX INTERFACE AND DATA ACQUISITION

The 8-step sequence is sent to the ABPIS (on fiber-optic cables) by a Spin State Controller (SSC) module located at the VAX computer interface. The SSC module was designed and built at TUNL. It is driven by the 10 Hz clock input which sets the spin-flip rate. The SSC has other functions as well. Neutron events occurring within several milliseconds of a spin-flip must be ignored because of the finite

beam transit time to the target. The SSC permits this since its clock input is passed to an output which triggers a veto signal. The veto is applied to a Phillips #706 sixteen channel discriminator (PS706), through which almost all signals are sent. The circuit is illustrated in figure 5.4. The veto signal disables the PS706 outputs during a 7 msec window around the spin-flip. Five milliseconds of this window occur after the flip. The logic timing is sketched in figure 5.5.

The SSC module has other functions related to the data acquisition and the CAMAC-VAX computer interface. Two such functions are signalling the end of a run and initiating the transfer of data from scalars to VAX storage. A trigger comes 900 μ sec after the end of each complete 8-step sequence. The trigger fires a count-down scaler which is set to a specified number of sequences per run. Each spin-flip is preceded by a pulse that triggers an Analog-to-Digital Converter (ADC). The pulse is produced when the veto of the PS706 is applied. The ADC samples a signal derived from the spin state signals put out by the SSC module. The ADC then triggers the VAX 11/780 to read and flush all scalars. The level of the ADC input tags the spin state of the data read from the scalars.

The SSC turns off when the CAMAC crate is shut down (inhibited) by software. This action stops the spin-flipping of the beam. Low beam current also disables the SSC since the crate inhibit is latched to an electronic gate on the proton beam current. After reenabling, the next clock pulse input to the SSC triggers the resumption of the 8-step sequence at the appropriate state. Optionally, the SSC can be reset to restart at the beginning of a sequence.

The signals stored in the computer include the neutron counts in each of the three detectors, their respective dead-time correction pulses, and the digitized beam current. A run consists of 1024 eight step sequences; the counts in each sequence put into 1024 channel XSYS data areas corresponding to spin *up* or *down*. A final value for, e.g., the total counts for spin up beam in the central detector for any given run is the total of the 1024 values stored in that data area. This data acquisition method permits comparing signals—such as *up* and *down* counts or

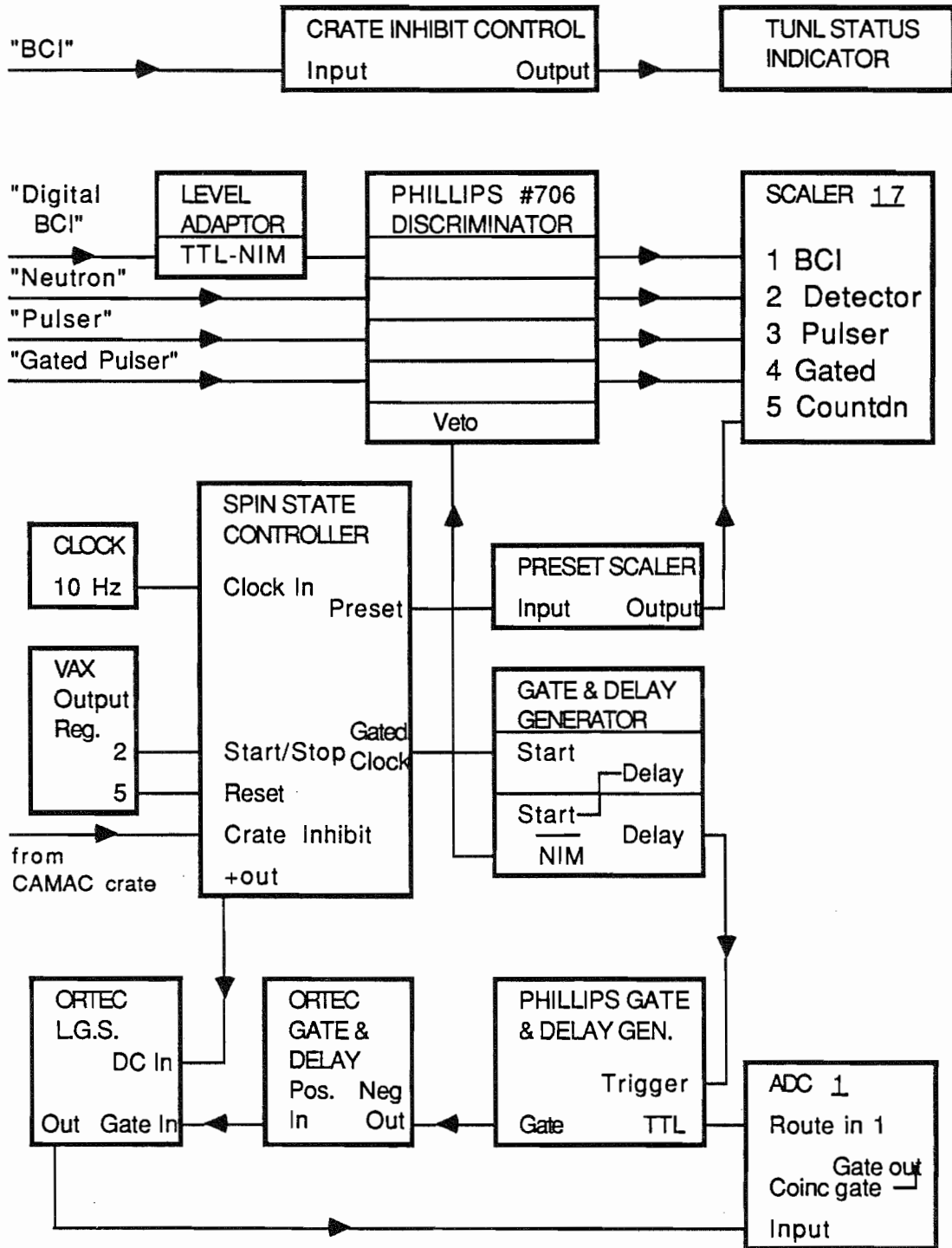


Figure 5.4: Block diagram of electronics at computer interface. Signals enter on the left from the signal processing modules (figure 2.15.) Not shown is the +/- fiber-optic cables from the SSC to the ABPIS.

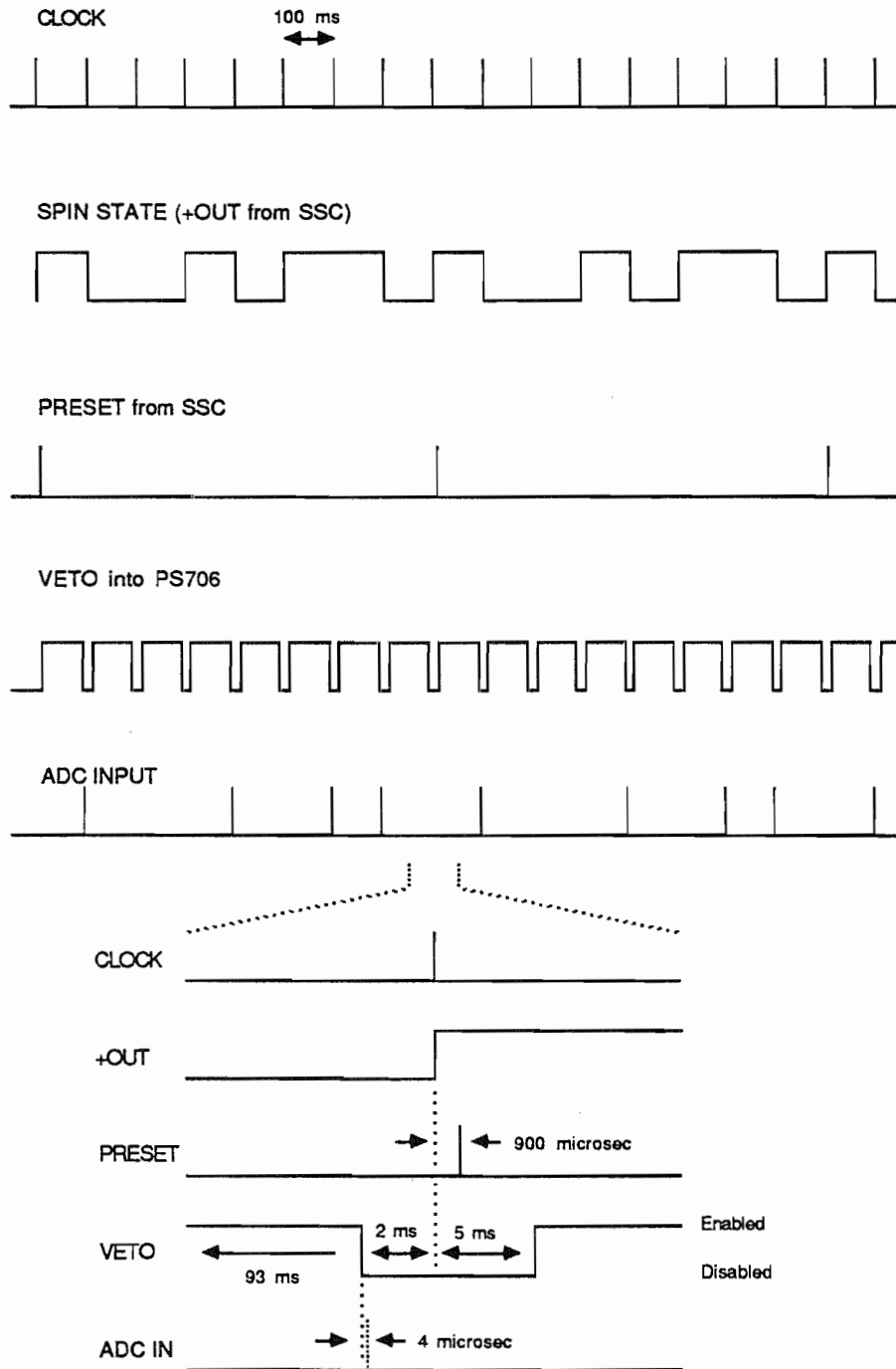


Figure 5.5: Logic diagram of the timing signals used for spin-flipping. The time scale is expanded at the bottom to show the detail of the 7 ms period during which data input is disabled.

beam current and detector yield—at finer intervals of time (8 tenths of a second for 10 Hz spin-flip) than simply on a run-by-run basis. Indeed, normalization of the detector yields to beam current, dead-time corrections, and formation of the spin asymmetry are all done on a channel-by-channel basis. (The data collecting described above applies also to the unpolarized beam measurements of the deformation effect. For these there is no distinction between spin *up* and *down* beam; the corresponding yields are simply added together.) Most quantities are monitored on a computer video terminal via the BOX feature of XSYS.

When a run ends as signalled by the countdown scaler, various quantities such as the spin asymmetry and error are calculated. Additionally, the target is rotated by automatic execution of a DCL command file. The amount and direction of rotation is set in accordance with user-defined global variables. With these the angle sequence is determined by the experimenter. Three bits representing the destination angle of the holmium target are sent to the TI Controller in the target room (see section 2.3.5.) Before a new run is automatically started, the VAX checks the TI to ensure that the destination angle has been reached.

Chapter 6

FIVE-FOLD CORRELATION MEASUREMENT

The five-fold correlation measurement performed at TUNL is described in this chapter. The TRNI quantity to be extracted is shown explicitly in the first section. The next section discusses TRI spin asymmetries—those with an angle θ dependence differing from the FC and those with the same dependence. The experimental results are limned in the third section. Finally, some statement is made as to comparing the bound on TRNI deduced here with that of other experiments.

6.1 ANALYSIS

The FC is manifested as a contribution to the total cross-section (equation 3.1),

$$\sigma_T = \sum \sigma_{kK}, \quad (6.1)$$

in which

$$\begin{aligned} \sigma_{kK} = & \operatorname{Re} \left\{ 2\pi\lambda^2 \sum_{\Lambda q} \hat{\Lambda} \langle \Lambda k 0 q | K q \rangle t_{kq}(s) t_{Kq}^*(I) \sum_J g_J \times \right. \\ & \left. \sum_{l'j'lj} T_{Kk\Lambda}(l'j'lj) [\delta_{ll'} \delta_{jj'} - S_J(lj \rightarrow l'j')] \right\}. \end{aligned} \quad (6.2)$$

The statistical tensor describing the spin state of the beam has rank k ; that for the target has rank K . Only $k = 0, 1$ exists for the spin-1/2 neutrons, while $K \leq 2I + 1 = 8$ for the spin-7/2 holmium target. The σ_{kK} include angular momentum coupling coefficients in $T_{Kk\Lambda}$,

$$T_{Kk\Lambda}(l'j'ljJ) = (-1)^K \hat{s} \hat{l} \hat{j} \hat{k} \hat{\Lambda} \hat{I} \hat{j}' \langle l\Lambda 00 | l'0 \rangle W(JjIK; Ij') \left\{ \begin{array}{ccc} j' & l' & s \\ j & l & s \\ K & \Lambda & k \end{array} \right\}. \quad (6.3)$$

W is a Racah coefficient and the last factor is a 9- j symbol. From the 9- j symbol it is clear that Λ is limited by k and K : $|K - k| \leq \Lambda \leq |K + k|$. Gould, et. al. (1990) have noted that under exchange of initial and final states (time reversal)

$$T_{Kk\Lambda}(l'j'ljJ) = (-1)^{K+k+\Lambda} T_{Kk\Lambda}(lj'l'j'J) \quad (6.4)$$

and therefore time reversal non-invariant terms correspond to $K + k + \Lambda$ odd. Thus a polarized-beam aligned-target experiment involving the term σ_{12} includes a contribution ($\Lambda = 2$) which violates time reversal invariance. Other spin correlations arise in σ_{12} which correspond to $\Lambda = 1, 3$ and are TRI—these, however, are parity nonconserving.

Assignments of σ_{kK} to scalar products are listed in table 6.1 for $K \leq 2$. (The relevant target temperature implies $t_{40} \sim 6 \times 10^{-4}$ and so the $K > 2$ terms in σ_T are negligible. Indeed from measurements of the deformation effect in chapter 3, no orientation with $K \geq 4$ is evident.) The number of occurrences of the wavevector \vec{k} is given by Λ . The T-odd five-fold correlation corresponds to $\sigma_{12}(\Lambda = 2)$.

In chapter 1 we discussed the signature of the FC by its unique dependence on the angle θ between \vec{l} and \vec{k} , with \vec{s} perpendicular to $(\vec{l} \times \vec{k})$. This will now be seen quantitatively. The geometric direction and rank of the spin orientations are selected to maximize $\sigma_{12}(\Lambda = 2)$. Explicitly $\sigma_{12}(\Lambda = 2) =$

$$\sigma_{FC} = \text{Re} \left\{ 2\pi \lambda^2 \sum_{q=\pm 1} \hat{2} \langle 210q | 2q \rangle t_{1q}(1/2) t_{2q}^*(7/2) \sum_J g_J \times \sum_{ll'jj'} T_{212}(l'j'ljJ) [\delta_{ll'} \delta_{jj'} - S_J(lj \rightarrow l'j')] \right\}. \quad (6.5)$$

Table 6.1: Spin correlations and their associated beam and target statistical tensor ranks. The vector \vec{k} represents the neutron beam momentum and is unrelated to the scalar rank k .

k	K	Λ	Spin Correlations
1	0	1	$\vec{s} \cdot \vec{k}$
0	1	1	$\vec{I} \cdot \vec{k}$
1	1	0	$\vec{s} \cdot \vec{I}$
1	1	1	$(\vec{I} \times \vec{k}) \cdot \vec{s}$
1	1	2	$(\vec{s} \cdot \vec{k})(\vec{I} \cdot \vec{k})$
0	2	2	$(\vec{I} \cdot \vec{k})^2$
1	2	1	$(\vec{s} \cdot \vec{I})(\vec{I} \cdot \vec{k})$
1	2	2	$\vec{s} \cdot (\vec{I} \times \vec{k})(\vec{I} \cdot \vec{k})$
1	2	3	$(\vec{s} \cdot \vec{k})(\vec{I} \cdot \vec{k})^2$

The statistical tensors here refer to the neutron beam direction. This reference frame is rotated with respect to the beam and target symmetry axes to which the respective \hat{t} refer. The vertical neutron spin tensor

$$t_{1\pm 1}(1/2) = \frac{-i}{\sqrt{2}} \hat{t}_{10} \quad (6.6)$$

from equation 2.11 or directly from Simonius (1974). The target tensor is described by

$$t_{2\pm 1}^*(7/2) = t_{2\pm 1}(7/2) = \mp \sqrt{\frac{3}{2}} \sin \theta \cos \theta \hat{t}_{20}(7/2). \quad (6.7)$$

(Note that the deformation effect depended on t_{20} with its different θ -dependence.)

Inserting these into equation 6.5 with $\langle 210 -1 | 2 -1 \rangle = -\langle 2101 | 21 \rangle = 1/2\sqrt{2}$,

$$\begin{aligned} \sigma_{FC} = & \sqrt{\frac{15}{8}} \sin \theta \cos \theta \hat{t}_{10}(1/2) \hat{t}_{20}(7/2) \text{Re}\{2\pi i \lambda^2 \times \\ & \sum_J g_J \sum_{ll'jj'} T_{212}(l'j'ljJ) [\delta_{ll'} \delta_{jj'} - S_J(lj \rightarrow l'j')]\}. \end{aligned} \quad (6.8)$$

The other terms in σ_T are dominated by the unpolarized term σ_{00} . The odd- K terms are negligible because the target is unpolarized. Indeed $t_{10} \simeq 2 \times 10^{-7}$ for the target at 0.3 K in an ambient magnetic field of ~ 1 Gauss due to the earth. Then

$$\sigma_T = \sigma_{00} + \sigma_{FC}. \quad (6.9)$$

We further define an FC analyzing power A_{FC} through

$$\frac{\sigma_{FC}}{\sigma_{00}} = \sqrt{\frac{15}{8}} \sin \theta \cos \theta \hat{t}_{10} \hat{t}_{20} A_{FC} \quad (6.10)$$

wherein the particular factors involving $K = 2, k = 1, \Lambda = 2$ and the degrees of spin orientation t have been removed from A_{FC} . Then

$$\sigma_T = \sigma_{00} \left(1 + \sqrt{\frac{15}{8}} \sin \theta \cos \theta \hat{t}_{10} (1/2) \hat{t}_{20} (7/2) A_{FC} \right). \quad (6.11)$$

The expression 6.11 for σ_T enters into the neutron transmission according to equation 3.10. The initial reduction of the polarized-beam aligned-target data involves the extraction of a neutron spin asymmetry from the polarized neutron transmission yields. The yields for neutron spin *up* and *down* are normalized to the proton beam current; a correction factor is applied representing lost neutron counts due to the dead-time of the electronics. The asymmetry ϵ is formed for each run,

$$\epsilon_i(\theta_i) = \frac{N^+(\theta_i) - N^-(\theta_i)}{N^+(\theta_i) + N^-(\theta_i)} \quad (6.12)$$

The superscript on N denotes the neutron spin state. The asymmetry and angle (and yield N implicitly) are parametrized by the run number i . (No subtraction of detector gain drift from the yield is made since the neutron spin is flipped every 100 msec.) Then

$$\epsilon(\theta) = \sqrt{\frac{15}{8}} \sin \theta \cos \theta \left[\frac{\hat{t}_{10}^+(1/2) - \hat{t}_{10}^-(1/2)}{2} \right] \hat{t}_{20}(7/2) n \sigma_{00} A_{FC}. \quad (6.13)$$

As before, n is the mean target thickness; $\epsilon(\theta)$, θ , and \hat{t} are implicit functions of i . The $+[-]$ superscript on \hat{t}_{10} denotes polarization for neutrons with spin *up* [*down*].

The second step in the data reduction is to exploit the θ -dependence to extract A_{FC} . The average asymmetry $\bar{\epsilon}(\theta)$ at each angle θ is formed. The asymmetry can be fit with a $\sin \theta \cos \theta$ function, or the angles which maximize the amplitude σ_{FC} can be exploited in forming

$$\epsilon_{FC} \equiv \frac{\bar{\epsilon}(45^\circ) + \bar{\epsilon}(-135^\circ)}{2} - \frac{\bar{\epsilon}(-45^\circ) + \bar{\epsilon}(135^\circ)}{2} \quad (6.14)$$

so that finally

$$\epsilon_{FC} = \sqrt{\frac{15}{8}} \left[\frac{\hat{t}_{10}^+(1/2) - \hat{t}_{10}^-(1/2)}{2} \right] \hat{t}_{20}(7/2) n \sigma_T A_{FC}. \quad (6.15)$$

(In this expression σ_{00} has been replaced with σ_T with negligible error introduced in ϵ_{FC} .) The latter method of extraction is useful if data is taken only at $\theta = \pm 45^\circ, \pm 135^\circ$.

6.2 TRI CONTRIBUTIONS TO SPIN ASYMMETRY

A non-zero spin asymmetry $\epsilon(\theta)$ may arise from effects other than the FC. The largest by far of these additional terms in equation 6.13 is the false asymmetry due to a detector whose center is off the beam axis, and the $T(\vec{p}, n)$ analyzing power. The term is due to a misalignment of the detector; it is a constant added to equation 6.13. According to equation 5.2, the count rate I of neutrons produced at angle Θ with respect to the incident proton beam is

$$I(\Theta) = I_0(\Theta)[1 + p_y A_y(\Theta)]. \quad (6.16)$$

At small angles Θ , A_y is linear. Consider the 0° detector to be off-axis by some angle δ , with a solid angle of half-angle α . Then the count rate N^\pm for neutrons across the detector face with spin *up/down* is

$$N^\pm = \int_{\delta-\alpha}^{\delta+\alpha} I^\pm(\Theta) d\Theta = \int_{\delta-\alpha}^{\delta+\alpha} I_0^\pm [1 + p_y^\pm A_y(\Theta)] d\Theta, \quad (6.17)$$

assuming perfect detector efficiency and α small enough such that the distance between neutron source and detector face is constant in Θ . Then the analyzing power has the form $A_y = m\Theta$. Assume I_0^\pm is isotropic within the detector's solid angle: $I_0^\pm(\Theta) = I_0^\pm$. Then

$$N^\pm = I_0^\pm \int_{\delta-\alpha}^{\delta+\alpha} (1 + p_y^\pm m\Theta) d\Theta = 2\alpha I_0^\pm + 2\alpha\delta m I_0^\pm p_y^\pm. \quad (6.18)$$

Define a false asymmetry signal

$$\Delta\epsilon \equiv \frac{N^+ - N^-}{N^+ + N^-}. \quad (6.19)$$

Assuming $I_0^+ = I_0^-$,

$$\Delta\epsilon = \frac{m\delta \Delta p_y}{2 + m\delta(p_y^+ + p_y^-)} \quad (6.20)$$

where $\Delta p_y \equiv p_y^+ - p_y^-$. (Recall that $p_y^- \approx -p_y^+$.) At proton energy 2.7 MeV, $A_y(\Theta = 20^\circ) = 0.23$ (Tornow 1981). Therefore $m = 0.66$. Thus for example, if $\Delta p_y \sim 1.0$ and the detector is misaligned by merely $\delta = \frac{1^\circ}{2}$, $\Delta\epsilon \sim 3 \times 10^{-3}$.

Another potential constant term will arise if the beam intensity systematically differs for spin *up* and spin *down*, $I_0^+ \neq I_0^-$. This effect will be removed by use of equation 6.13 or 6.14.

An apparent transmission asymmetry might arise also from multiple scattering. If one of the scattering events occurs in the holmium, the resulting asymmetry might have the θ -dependence of the FC. However, any contribution is below the sensitivity of the present experiment. For double scattering within the solid angle of the detector collimation (direct scattering), the count rate in the detector is 10^{-3} times the single scattering rate (following the procedure of Bratenahl 1958.) The deformation effect is of order 10^{-2} , and analyzing powers describing asymmetric scattering of the polarized beam are of order 10^{-1} . Therefore a transmission asymmetry due to spin-dependent multiple scattering is less than 10^{-6} . Rescattering of the neutrons in which one of the scattering events occurs in material other than the holmium will contribute even less to the detector count rate because of attenuation in the collimator.

Equation 6.13 may contain other terms with various dependences on θ arising from the spin correlations in table 6.1. These terms affect $\epsilon(\theta)$ by attenuating the beam preferentially with neutron spin; they are minimized by preparing the neutron spin \vec{s} in the vertical direction. However, precession of the neutron spin into the horizontal plane by a sequential spin correlation—or simply by a misalignment—can bring these terms back into play. The first correlation listed is the parity nonconserving $\vec{s} \cdot \vec{k}$ interaction. The strength of this interaction in holmium is, however, known to be small (Soderstrum 1988). Preparing the neutron spin to within, for example, 6° of vertical reduces the interaction another order of magnitude.

The next terms, where $K = 1$, are excluded by the lack of target polarization. The $\vec{I} \cdot \vec{k}$ interaction is PNC and so is expected to be small but regardless of size it is independent of neutron polarization and is eliminated in 6.12. The central and tensor spin-spin interactions $\vec{s} \cdot \vec{I}$ and $(\vec{s} \cdot \vec{k})(\vec{I} \cdot \vec{k})$ are essentially zero in holmium at a few MeV (Fasoli 1978). And again, the vertically polarized neutrons must be either misaligned or precessed into the I - k plane. Lastly, the three-fold correlation $\vec{s} \cdot \vec{I} \times \vec{k}$ is both P-odd and T-odd. For a polarized holmium target, it was measured to be less than 2×10^{-3} at 7.1 MeV (Soderstrum 1988).

The $(\vec{I} \cdot \vec{k})^2$ interaction is independent of neutron spin. The other $K = 2$ terms are linear in s , however, they require a component in the horizontal plane either through neutron spin misalignment or by precession due to an additional interaction. The latter possibility of two sequential TRI interactions has been analyzed by Bowman, et. al. (1990b) in terms of neutron optics. The pair of PNC interactions are the $(\vec{s} \cdot \vec{I})(\vec{I} \cdot \vec{k})$ and the helicity $\vec{s} \cdot \vec{k}$. They enter as terms in the forward scattering amplitude as discussed in chapter 1. The real part of the former term will precess \vec{s} about \vec{I} or the real part of the latter amplitude precesses \vec{s} about \hat{k} . The end result is a component s_h of \vec{s} in the horizontal plane. The imaginary part of the other amplitude then produces absorption of the neutron beam, preferential with neutron spin. We extend this treatment by

exploring the angular dependence of the resulting signal to see if it mimics the FC. Consider s_h to be at an arbitrary angle ϕ with respect to the beam direction \hat{k} (figure 6.1). Then

$$(\vec{s} \cdot \vec{I})(\vec{I} \cdot \vec{k}) \propto V_{sIIk} \cos(\phi - \theta) \cos \theta = V_{sIIk} \cos \phi \cos^2 \theta + V_{sIIk} \sin \phi \sin \theta \cos \theta. \quad (6.21)$$

Although this has not an identical θ -dependence as the FC, the two cannot be resolved by a careful mapping of $\epsilon(\theta)$ because of the other $K = 2$ interaction, $(\vec{s} \cdot \vec{k})(\vec{I} \cdot \vec{k})^2$, whose angular dependence is similarly determined to be $V_{skIk2} \cos \phi \cos^2 \theta$. Therefore with V_{FC} representing the A_{FC} term, equation 6.13 becomes

$$\epsilon(\theta) = (V_{skIk2} + V_{sIIk}) \cos \phi \cos^2 \theta + (V_{sIIk} \sin \phi + V_{FC}) \sin \theta \cos \theta. \quad (6.22)$$

Note that equation 6.22 is the complete set of interactions in σ_{12} (table 6.1). Thus rotation of the target is insufficient to distinguish V_{FC} from V_{skIk2} and V_{sIIk} . However, the FC-mimicking interactions are (to all orders K) parity non-conserving. Hence the false TRNI signal consists of two sequential PNC interactions, *each* at around 10^{-7} the strength of the parity conserving, time reversal invariant nucleon-nucleon interaction.

The occurrence of false TRNI terms in the present experiment is checked by direct measurement. It has already been mentioned that $\vec{s} \cdot \vec{k}$ was determined to be small (actually $\leq 3 \times 10^{-4}$ at 7.4 MeV.) The two TRI terms in σ_{12} were measured here. The neutron spin \vec{s} was prepared in the horizontal plane and the resulting false asymmetry, or ϵ_{TRI} , determined.

There are other ways to remove the false TRNI terms. One method provides a true reciprocity test by adding a neutron spin analyzer after the target (Stodolsky 1986) which permits rejection of spin-precessing events. An equivalent method is the comparison of the transmission asymmetry $\epsilon(\theta = 45^\circ)$ with induced polarization (Kabir 1988b). The FC measurement proposed for the Los Alamos Neutron Scattering Center (LANSCE) will modulate the target thickness n rather than θ .

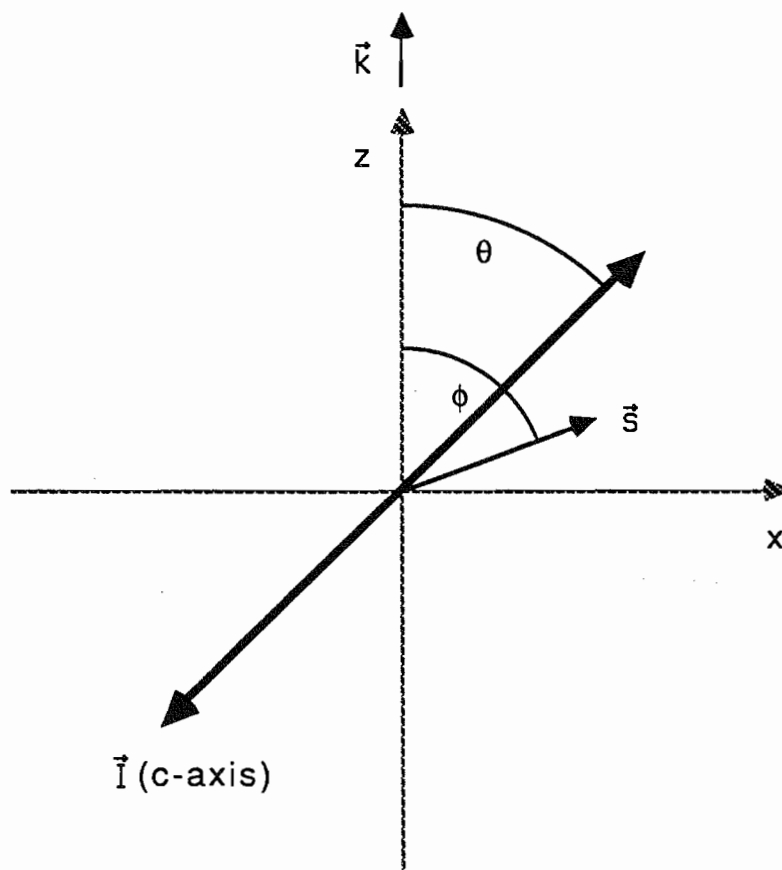


Figure 6.1: Angular dependence of $(\vec{s} \cdot \vec{I})(\vec{I} \cdot \vec{k})$ for coplanar vectors.

The result expected is

$$\epsilon(\theta = 45^\circ) = V_0 + V'_{FC}n + V_{false}n^2 \quad (6.23)$$

in which V'_{FC} contains no TRI components.

6.3 RESULTS

The raw data consists of neutron transmission yields with neutron spin set every 100 msec according to the eight-step sequence. The target alignment was positioned at various θ (table 6.3). The yields are normalized to proton beam current. No electronic dead-time correction is applied, since the correction differed between spin *up* and spin *down* by less than 2×10^{-5} . This reflects that no difference in beam intensity for the two spin states is observed.

The data are split into four blocks (I-IV) because interruptions in the polarized ion source operation led to slightly different beam tuning and polarization. The quantities common to all blocks are tabulated in table 6.2, while specific results are listed in table 6.3. The target thickness n is discussed in appendix 8.1. The

Table 6.2: Experimental constant parameters for the FC measurement.

Neutron Energy	1.92 MeV
Target thickness n	5.78×10^{-2} barn $^{-1}$
Target thickness $n\sigma_T$	0.41 m.f.p.
Target statistical tensor	0.45
Amount of maximum alignment	65%
Polarization transfer $K_y^y(0^\circ)$	0.62
Detected neutron flux	7000 sec $^{-1}$

thickness in *mean free paths* assumes a total cross-section for neutrons on ^{165}Ho of

Table 6.3: Experimental variable parameters for the FC measurement.

Data Block	Number of Runs	Angle Sequence		p_y	ϵ_{FC} ($\times 10^{-4}$)
		Limits	Increment		
I	94	± 135	45	0.37	$-0.37 \pm 1.13 \pm 1.12$
II	145	± 135	45	0.36	$0.33 \pm 0.78 \pm 0.96$
III	73	± 135	45	0.36	$0.21 \pm 0.91 \pm 1.02$
IV	41	± 135	90	0.40	$0.22 \pm 1.20 \pm 1.61$

7.04 barns (McLane 1988). The holmium target temperature fluctuated about a constant value (285 mK) the entire experiment. Within a block of runs, the proton polarization is seen to be very stable (figure 6.2). The quantity p_y in table 6.3 is the average neutron polarization for both spin states:

$$p_y = \frac{1}{2}[t_{10}^+(1/2) - t_{10}^-(1/2)], \quad (6.24)$$

in which the statistical tensor depends on the proton polarization $t_{10}^\pm(p)$ through

$$t_{10}^\pm(1/2) = K_y^y(0^\circ)t_{10}^\pm(p). \quad (6.25)$$

The factor $K_y^y(0^\circ)$ is the polarization transfer coefficient (chapter 5). The spin asymmetry ϵ_{FC} is calculated using equation 6.14; the FC analyzing power A_{FC} is calculated via equation 6.15.

The extraction of A_{FC} from ϵ_{FC} may be ambiguous if the PNC components of σ_{12} are present as discussed in the preceding section. Therefore their strengths were tested in the middle of the FC experiment by placing the neutron spin in the horizontal plane. This orientation (figure 6.1) maximizes sensitivity to $(\vec{s} \cdot \vec{I})(\vec{I} \cdot \vec{k})$ and $(\vec{s} \cdot \vec{k})(\vec{I} \cdot \vec{k})^2$ while minimizing sensitivity to the FC. The actual orientation of \vec{s} was $\phi = -140^\circ$ for spin *up* and $\phi = 40^\circ$ for spin *down*. The resulting false TRNI asymmetry for 31 runs is $\epsilon_{TRI} = (-1.08 \pm 1.43) \times 10^{-4}$. This bound is not inconsistent with an expected strength of two sequential PNC interactions.

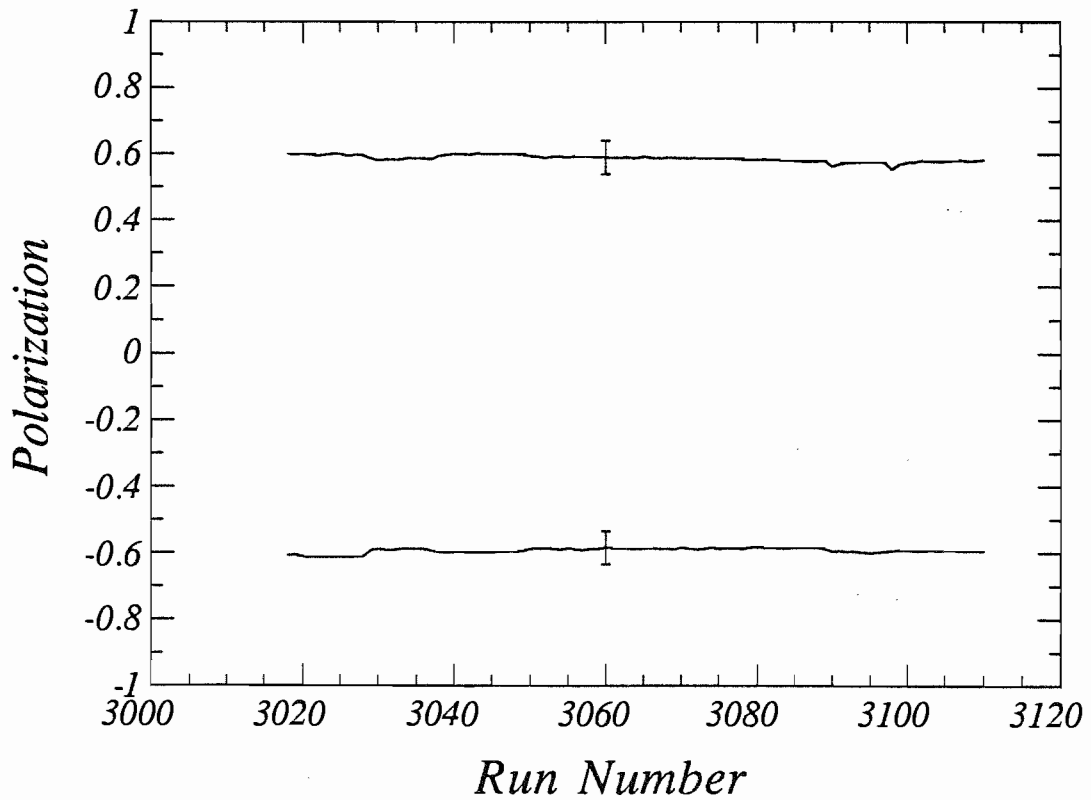


Figure 6.2: Proton polarization during one block of runs. The error bars denote the experimental uncertainty, due largely to the uncertainty in the analyzing power.

During the FC measurement when the neutron spin is vertical, this false TRNI asymmetry is reduced at least an order of magnitude. Hence any extra term surviving in equation 6.15 which is TRI is

$$\epsilon_{TRI} \leq 1.5 \times 10^{-5}. \quad (6.26)$$

The deduced analyzing power of the TRNI five-fold correlation $(\vec{s} \cdot \vec{l} \times \vec{k})(\vec{l} \cdot \vec{k})$ is tabulated in table 6.4. The average analyzing power for the four blocks of data

Table 6.4: Deduced analyzing powers for the FC measurement.

Data Block	A_{FC} ($\times 10^{-4}$)
I	$-3.96 \pm 12.09 \pm 11.98$
II	$3.63 \pm 8.58 \pm 10.56$
III	$2.31 \pm 10.01 \pm 11.22$
IV	$2.18 \pm 11.88 \pm 15.94$
Average	$1.04 \pm 5.37 \pm 6.30$

is

$$A_{FC} = (1.04 \pm 5.37 \pm 6.30) \times 10^{-4}. \quad (6.27)$$

The first uncertainty given in A_{FC} (and the tables) is due to counting statistics. The second error is the reduced standard deviation in $\epsilon_i(\theta)$ about $\bar{\epsilon}(\theta)$, from run to run at a particular θ :

$$\sigma \simeq \sqrt{\frac{1}{N-1} \sum_{i=1}^{N \text{ runs}} [\epsilon_i(\theta) - \bar{\epsilon}(\theta)]^2 / \sqrt{N}}. \quad (6.28)$$

The latter error incorporates all sources of random fluctuation about $\bar{\epsilon}(\theta)$, and so is more general. An important observation however, is that this error is due largely to the statistical uncertainty.

In order to inspect $\bar{\epsilon}(\theta)$ visually for a $\sin \theta \cos \theta$ form, 132 runs have been chosen from block II which illustrate the nuclear deformation effect. The total neutron yield is averaged over these runs at each angle θ . An angle asymmetry $\epsilon(\theta)$ is calculated relative to the yield averaged over all angles:

$$\epsilon(\theta) = \frac{\bar{N}(\theta) - \overline{N(\theta)}}{2\overline{N(\theta)}}. \quad (6.29)$$

(See figure 6.3.) The form of $\epsilon(\theta)$ is the familiar $P_2(\cos \theta)$ (equation 3.11). The spin asymmetry $\bar{\epsilon}(\theta)$ is plotted for comparison. No significant dependence on θ is observed. (The probability that every $\bar{\epsilon}(\theta)$ is within one sigma of zero as shown is a non-negligible 7%.)

A systematic error entered $\epsilon(\theta)$ in data set III. The spin asymmetry $\overline{\epsilon(\theta)}$ averaged over all angles is consistent with zero in sets I and II. But for set III, $\overline{\epsilon(\theta)} = (3.30 \pm 0.50) \times 10^{-4}$. This shift is explained by the off-axis false asymmetry described in section 6.2. The centroid of the horizontal profile of the proton beam is plotted as a function of run for the relevant blocks of runs in figure 6.4. The change in position of the beam between sets II and III corresponds to a shift of 743 μm . Given that the centroid of the beam in the scanner, the beam quad collimator at the neutron production cell, and the detector center were originally collinear, the shifted beam—still centered in the quad collimator—now effectively places the detector off-axis of the beam. The 125 cm separation of the scanner and the quad collimator implies the detector is off-axis by 0.034° . Invoking equation 6.20 with $\Delta p_y = 1.15$ and $m = 0.66$, $\Delta\epsilon = 2.3 \times 10^{-4}$. This systematic error in $\epsilon(\theta)$ is within two sigma of the value of $\overline{\epsilon(\theta)}$ for set III.

6.4 DISCUSSION OF RESULTS

The present bound (equation 6.27) on TRNI interactions is obtained from a novel system compared to other deduced bounds. The analyzing power can not be compared directly to other bounds without reduction to a more fundamental quantity.

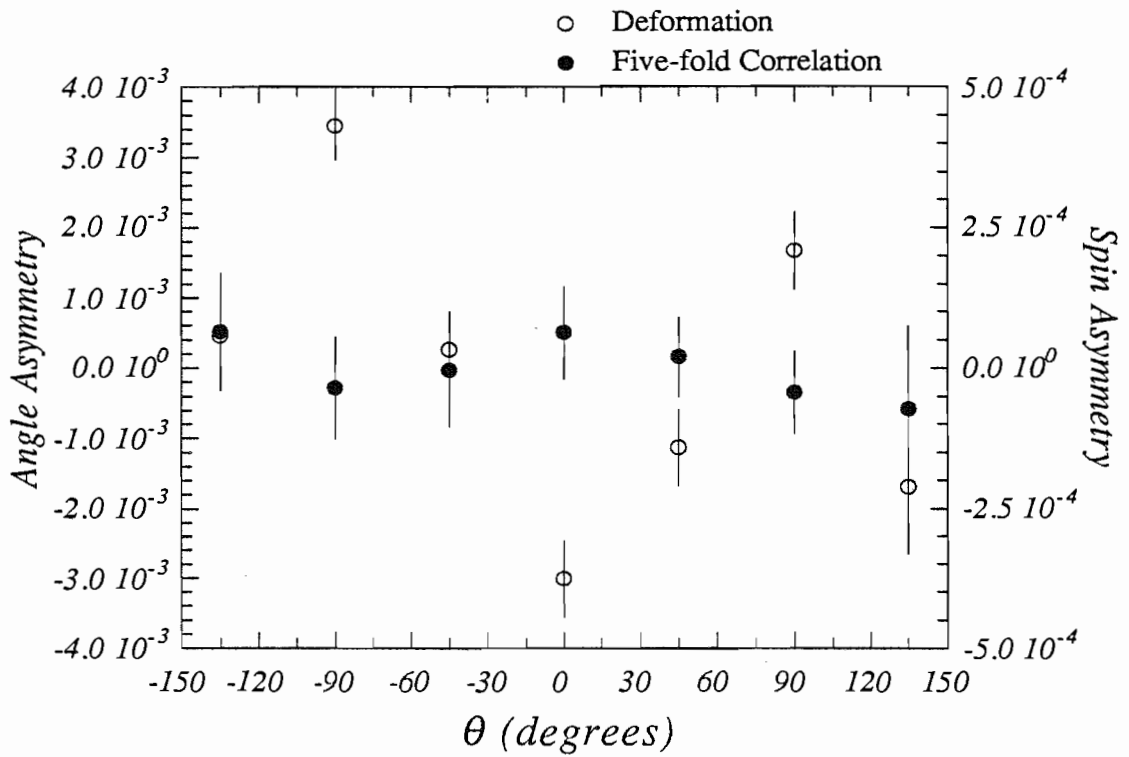


Figure 6.3: Angle and spin asymmetries in neutron transmission as a function of θ . The angle asymmetry is due to the nuclear deformation effect. Its angular dependence is $P_2(\cos\theta)$. The FC asymmetry is proportional to the $\sin\theta \cos\theta$ component of the spin asymmetry, but no significant θ dependence is observed.

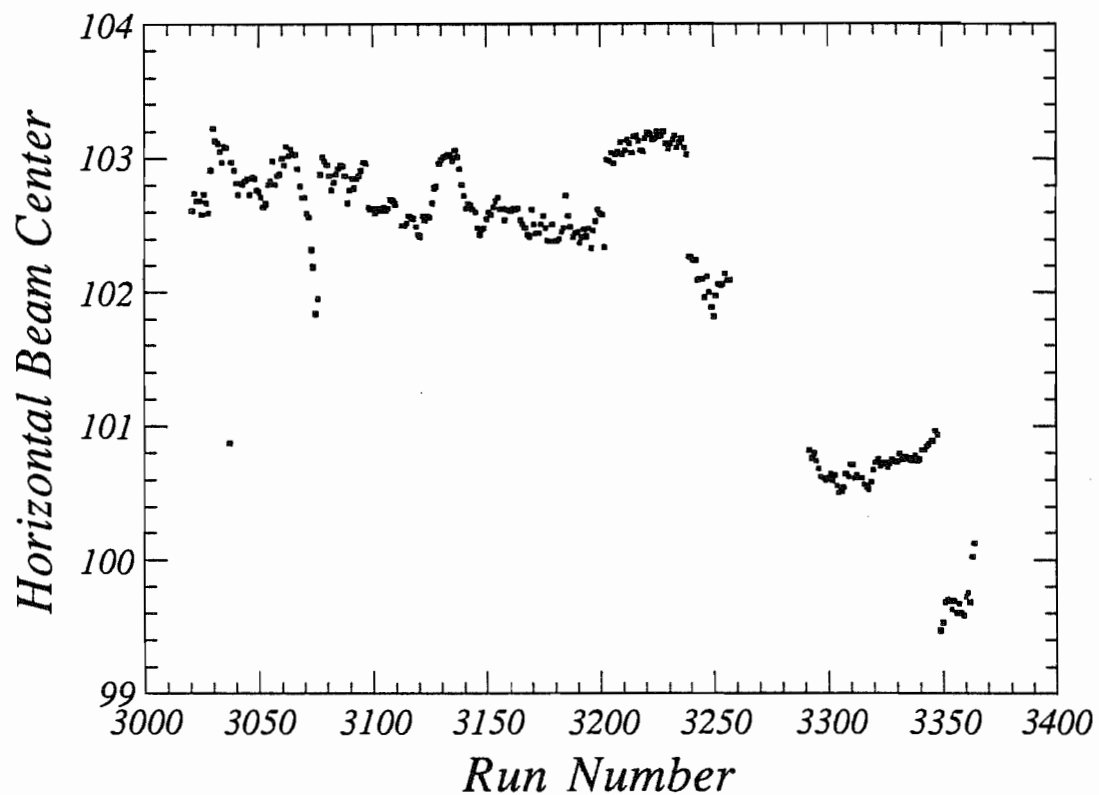


Figure 6.4: Proton beam position in the horizontal plane as a function of run number. The ordinate is the centroid of the intensity peak in the horizontal scan across the proton beam. Its units are factors of $347 \mu\text{meters}$.

The present experiment compares most naturally to the other parity conserving TRNI test in the hadronic sector, the unpolarized detailed-balance test of Blanke (1983) or Driller (1979) and collaborators described in the first chapter. The bound on a ratio of the TRNI scattering amplitude to the TRI amplitude was 5×10^{-4} , very similar to our A_{FC} . The reanalysis of Harney produced a bound on α_T of 2.6×10^{-4} . The FC experiment is done at too high an excitation energy (with not enough energy resolution) to yield a stringent bound on α_T through a compound nuclear analysis. A bound on α_T through manifestation in a direct reaction is more relevant—exactly because of the finite energy resolution (about 100 keV) and hence, the inherent energy averaging. Occurrence of TRNI in direct reactions was considered by Moldauer (1968a and 1968b) but not in the context of spin correlations. The indirect relation obtained in this context between A_{FC} and α_T is expected to be of order one (Davis 1990) and so is the subject of renewed theoretical effort. The forthcoming result will allow direct comparison of the bounds placed on TRNI by unpolarized detailed balance tests and by the FC test, and suggests that they will be very similar. The bound may be lowered in that event, by repeating the experiment with increased beam polarization and intensity, and target alignment. The case is similar to that for the measurement of the direct reaction component of the three-fold correlation $\vec{s} \cdot \vec{I} \times \vec{k}$ (Soderstrum 1988) in which the implied bound on α_{PT} , the P-odd T-odd relative strength, has not been calculated. Other PNC, TRNI tests all place uncertain bounds on α_T , although limits on the electric dipole moment of the neutron place a stringent bound on α_{PT} unlikely to be surpassed by the neutron transmission measurement.

An epithermal neutron transmission measurement of the five-fold correlation planned at the Los Alamos Neutron Scattering Center (LANSCE) will take advantage of the enhancements of symmetry violating effective nucleon-nucleon interactions in the compound nuclear system. That experiment is the natural successor to the PNC studies already under way there and the FC test presented here. A null result is expected to reduce the bound on α_T to 10^{-6} .

Chapter 7

CONCLUSIONS

Time reversal invariance has been tested in a completely new system. An analyzing power was determined for the five-fold correlation $(\vec{s} \cdot \vec{I} \times \vec{k})(\vec{I} \cdot \vec{k})$ in polarized neutron scattering on an aligned target. The analyzing power was deduced from the neutron transmission by double modulation of the scattering. The neutron polarization was reversed every 100 milliseconds (section 5.3) and the target alignment axis was rotated about the neutron spin direction (section 2.3.2) between experimental runs. The analyzing power obtained in section 6.3, $(1.0 \pm 6.3) \times 10^{-4}$, is consistent with time reversal invariance. Possible false T-odd signals have been considered in section 6.2 and demonstrated to be less than the sensitivity of the current experiment. The incident neutron energy of 2 MeV makes this test sensitive to a manifestation of TRNI in direct interactions. The bound obtained is comparable to the value of α_T of 2.6×10^{-4} obtained by Harney from analysis of detailed balance experiments. The present bound could be improved somewhat with longer running time, higher beam intensity, or increased neutron polarization or target alignment. However, a dramatic improvement is expected when the experiment is repeated at the Los Alamos Neutron Scattering Center. The epithermal neutrons will probe the compound nuclear interaction in which large enhancements of the neutron-nucleon symmetry breaking are expected. The in-

creased sensitivity to TRNI will improve the bound on the spreading width by a couple or so orders of magnitude. That experiment is made easier by the knowledge gained on systematics and procedures from the 2 MeV measurement.

The nuclear deformation effect has been measured at four energies with the aligned holmium target. The novel method involved transmission through different axes of the deformed nuclei instead of transmission through the nuclei oriented and unoriented. The results are in excellent agreement with previous measurements (section 3.3). The use of a rotating single crystal has enabled us to “see” the deformed nuclei rotate.

The deformation effect was reproduced using coupled channels calculations for the deformed optical model (section 4.2). Optical model parameters were taken from a previously published set that had reproduced several observables for nucleon scattering on ^{165}Ho . The parameters describing the deformation were permitted to vary to obtain the best fit to the present data and past data combined. The calculated effect is in good agreement overall with the data and has improved upon a previous adiabatic coupled channels calculation. Quantitatively, we feel the fit to data could be improved even more by readjustment of other optical model parameters. This “fine-tuning” will be explored in the future.

The deformation parameters obtained by calculating the nuclear deformation effect are similar to those obtained from inelastic scattering or electromagnetic decay experiments (section 4.3). We have considered hexadecapole deformation—about which experimental information is lacking for the odd-mass heavy nuclei. Its value is small as anticipated from systematics in even-even nuclei, and slightly negative. Hexacontatetrapole deformation was also considered and found to have a very small effect, on the order of a percent.

Chapter 8

APPENDICES

8.1 HOLMIUM TARGET THICKNESS

The holmium target is cylindrical. Therefore, its mean thickness depends non-linearly on the area of illumination by the beam. For a cylinder of radius r , the average chord length in a circle of radius r when a window of width w is centered on a diameter (figure 8.1) is

$$\bar{x} = \frac{r[\alpha_l + \frac{\sin 2\alpha_l}{2}]}{\sin \alpha_l}, \quad (8.1)$$

where $\sin \alpha_l = w/2r$. If $w = 2r$ is taken such that the entire circle is considered, then $\alpha_l = \pi/2$ and $\bar{x} = \frac{\pi}{2}r$. The geometric solid angle fixed by the polyethylene collimator is 4.6 msr or a 1.9° by 1.9° cone. This defines a window within the center of the holmium target that is 2.20 cm square. Thus if the 2.29 cm diameter holmium cylinder is placed centrally in the detector's field of view, all detected neutrons have passed through holmium, whose mean thickness is 1.85 cm . However, the polyethylene is not a perfect absorber, and so the solid angle is somewhat larger. By measuring the attenuation of the neutrons through the (warm, unoriented) holmium target, the target was found to be overilluminated by the beam. The results are consistent with an illuminated area at the center of the target of

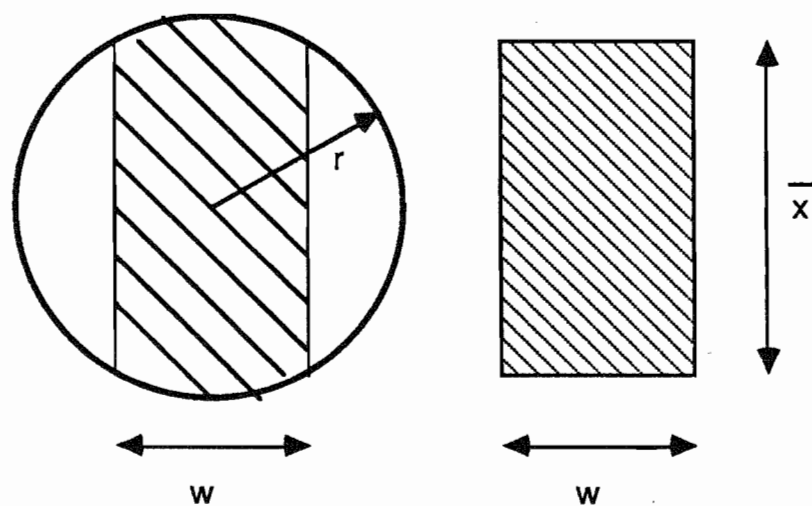


Figure 8.1: Cross section of cylindrical holmium target. The shaded area is the section within the window of width w set by the solid angle of the detector collimation. The mean target thickness is the average chord length through this area.

2.45 *cm* square. This was verified with aluminum targets of uniform thickness but various widths. All targets covered the apparent solid angle vertically. The likelihood of overillumination was indicated by a holmium target-in, target-out transmission measurement, in which the transmission through the holmium was somewhat larger than expected. This was done at room temperature so some of the copper coldfinger was visible in the detector solid angle because thermal contraction of the cryostat upwards was absent. The copper section was essentially a disk, 2.16 *cm* in diameter, seen edge-on. The effective neutron aperture is depicted in figure 8.2. The ratio of transmission for target-in to target-out is

$$trans = \frac{A_{air} + A_{Ho}e^{(-\rho\bar{x}\sigma)_{Ho}} + A_{Cu}e^{(-\rho\bar{x}\sigma)_{Cu}}}{A_{air} + A_{Ho} + A_{Cu}e^{(-\rho\bar{x}\sigma)_{Cu}}}, \quad (8.2)$$

with transmission through air = 100% and total area (A) = w^2 . The cross sections are input, and w is varied until the relative transmission calculated agrees with that observed. The procedure is repeated similarly for different sizes of aluminum in place of the holmium. The results were averaged to arrive at $w = 2.45$ *cm*. Hence the real target thickness is the mean chord length for the whole cylinder, 1.80 *cm*, since the entire width of the target is seen. Moreover, some neutrons are detected which miss the target; the fraction that pass through holmium is just 2.29×2.45 over 2.45×2.45 , or 93.5%.

Provided \bar{x} is correct, the ramifications of some neutrons passing around the holmium target for these experiments are minor. Both the deformation effect and the five-fold correlation measurements involve detecting modulations in the total neutron yield. Detected neutrons that have not interacted with the target serve merely to raise the background count rate on which such modulations are measured. A general treatment of the case in which a fraction H of the detected neutrons "hit" the target, and $M = 1 - H$ "miss" the target consists of modifying equation 3.11 to read

$$N(\theta, t) = N_0(t)(He^{-n\sigma\tau(\theta)} + M). \quad (8.3)$$

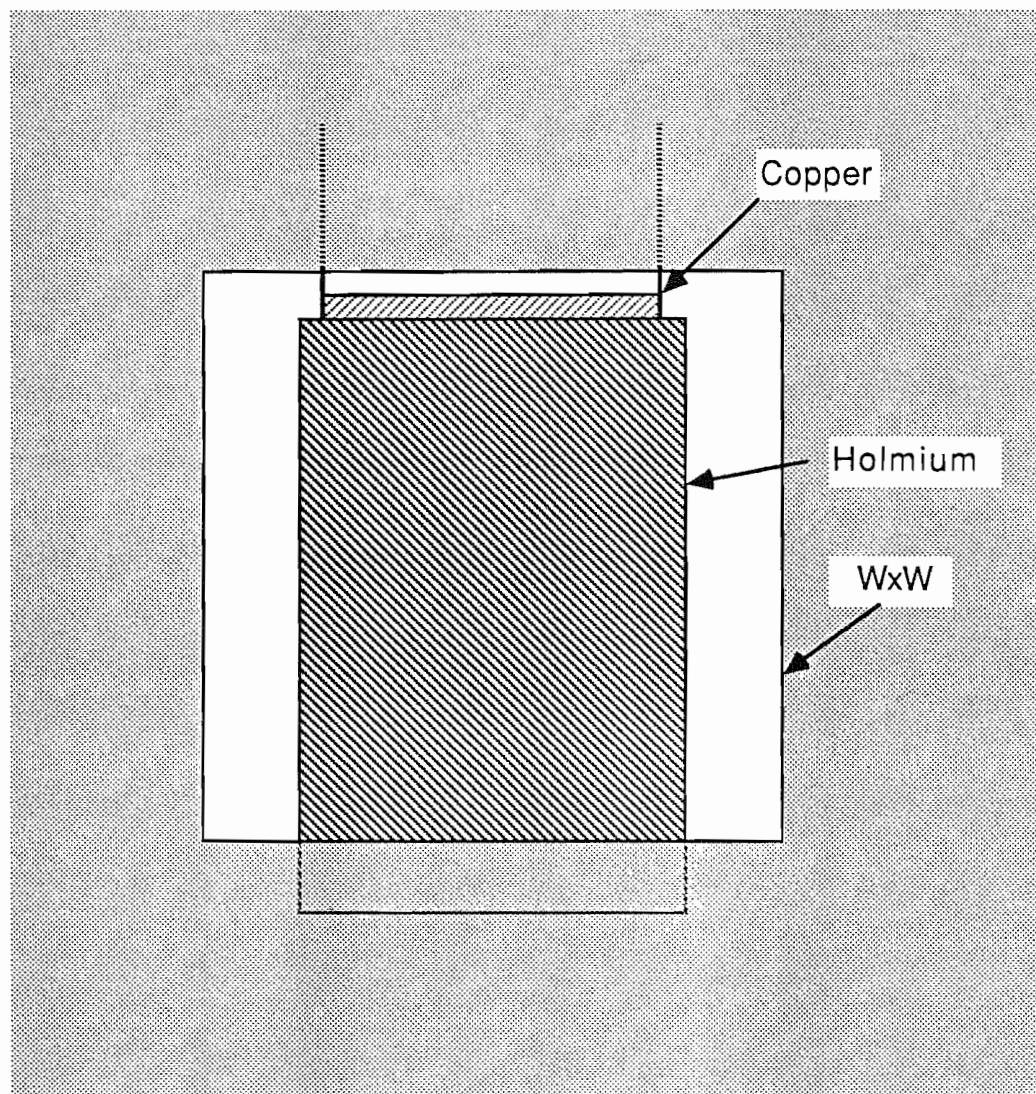


Figure 8.2: View of the target within the solid angle of the detector collimator. The window is a vertical slice through the center of the target, with dimension w a free parameter.

By subtracting away the long-term changes of the yield in time, through fitting with quadratics—or any other method of extracting the modulation, the additional term is removed:

$$N^*(\theta) = N(\theta, t) - F(t) \simeq N_0^* H e^{-n\sigma_T(\theta)}. \quad (8.4)$$

From this it is clear that the factor H need not be known. For example, in the simplest case of only $K = 2$ order alignment,

$$\ln N^*(\theta) = \ln(N_0^* H e^{-n\sigma_0}) - t_{20}(\theta) n \sigma_2. \quad (8.5)$$

The coefficients in the σ_2 term are identical to those in equation 3.15. This argument still holds when N is also a function of incident beam spin, as in the five-fold correlation experiment.

With a density of $\rho = 3.21 \times 10^{22} \text{ cm}^{-3}$, the holmium target thickness is therefore $n = \rho \bar{x} = 5.78 \times 10^{-5}$ per mbarn. Multiplying this by the energy dependent total cross-section σ_0 yields the mean thickness in units of a mean free path.

8.2 DEFORMATION CALCULATION CODE

Several steps are necessary to perform the coupled channels calculations of chapter 4. Program YOUNG.FOR is the program to compute and print energy dependent deformed optical model parameters using the set in (Young 1983). It prints on device 1. Then CONPAR.FOR reformats these parameters to be acceptable for input to the code ECIS. CONPAR looks for the parameter file on device 2, reading a template such as HO.DAT on device 1; it prints the ECIS input file on device 7. This input file must be assigned to device 5 to be read by ECIS. Output of interest from ECIS is sent to device 6—that written to device 66 can be deleted. ECIS is executed as a BATCH job, since over 8 minutes of CPU time are used in the calculation of the S-matrix at each energy. The input for holmium is for the three lowest states in ^{165}Ho explicitly, as a deformed rotational band. ECIS.INF in the TUNL directory explains in detail the elements in HO.DAT or other ECIS input files. The ECIS output of interest are the real and imaginary $S_J(lj \rightarrow l'j')$ matrix elements. L-S coupling is used: $\vec{l} + \vec{s} = \vec{j}$, $\vec{j} + \vec{I} = \vec{J}$ for the incoming channel. The outgoing channel is denoted by primed quantities. The matrix is output in blocks of J^π , up to the maximum J specified. For each submatrix S_J of particular J , allowable values are $j = l \pm 1/2$ and $|J - I \pm 1/2| \leq l \leq (J + I + 1/2)$. Each complex element is labelled by ECIS with IC , ICP , N , L and J . N denotes the outgoing state of the target, I' . As we are interested in elastic scattering, all records with $N \neq 1$ are ignored. IC labels a set of possible l', j' for some pair of l, j . The identification $S_J(lj \rightarrow l'j')$ must be made. When $IC = 1$ and $N = 1$, $L = l = l'$ and $J = j = j'$. Subsequent values of L and J are l' and j' with l and j unchanged, until IC is incremented and l and j are reset to the present L and J .

DEFORME.FOR is the code which extracts S-matrix elements from the ECIS output and calculates cross-sections. It reads on device 1 and writes to device 7, and is run interactively as it asks for the rank K of the statistical tensor in equation 3.2. Although t_{K0} is encoded in the equation, it is set equal to 1.0. Therefore

the calculated cross-section corresponds to the σ_K of equation 3.6. This can be converted to σ_{tot} due to maximal orientation by multiplying by the maximum value of t_{K0} .

One needs be aware that in executing DEFORME, a limited form of title is necessary within the ECIS input and output. The input to ECIS can consist of runs at different energies (or perhaps, different β_2 values.) For such input, the title denotes the beginning of a new input set. Similarly, the title denotes a new set of output. However, during its scan of ECIS output, DEFORME is expecting S-matrix elements. Hence the title must not contain characters where DEFORME is reading numbers; moreover a -1 at the very beginning of the title flags DEFORME that that character record is the title. The title in HO.DAT is acceptable. This requirement can be ignored with the version DEFORM.FOR, which expects only one run set from ECIS. A second warning applies to the logic flags used in HO.DAT. Some of these select choices of output such as C-matrix elements and transmission coefficients. If logic flags are used as in HO.DAT, then DEFORME can handle the ECIS output. However, DEFORME has not been tested for different output created by other sets of logic flags. Such output is probably unwarranted, as it can get quite long because of all the amplitudes.

DEFORME is limited in the size of J it can accept, depending upon K . This limitation actually occurs in the angular momentum coupling subroutines, which can couple only three momenta whose total $j_1 + j_2 + j_3 \leq 33$. This is because the algorithms involve factorials, and $34!$ is too large for single precision. In practice, this means that for $K = 0$, J must be ≤ 12 , and for $K = 2$, $J \leq 11$. Therefore it is of no use to execute ECIS for large maximum possible J (indeed, floating point underflow errors occur in ECIS); however, from 10-20 MeV all S_J for J up to 11 must be used in order to reach convergence in the sums.

REFERENCES

- [Ada78] J. M. Adams and G. White. *A Versatile Pulse Shape Discriminator for Charged Particle Separation and Its Application to Fast Neutron Time-of-Flight Spectroscopy*. Nuclear Instruments and Methods, **156** 459(1978).
- [Alf73] V. P. Alfimenkov, V. N. Efimov, Ts. Ts. Pantelev, and Yu. I. Fenin. *Interaction of Polarized Resonant Neutrons in Oriented Nuclei*. Soviet Journal of Nuclear Physics, **17** 149(1973).
- [And70] A. C. Anderson. *Elementary Dilution Refrigeration*. Review of Scientific Instruments, **41** 1446(1970).
- [And80] A. C. Anderson. *Instrumentation at Temperatures Below 1 K*. Review of Scientific Instruments, **51** 1603(1980).
- [Apo70] A. A. Aponick, Jr., C. M. Chesterfield, D. A. Bromley, and N. K. Glendenning. *Quadrupole and Hexadecapole Deformations in Rare Earth Nuclei*. Nuclear Physics, **A159** 367(1970).
- [Ara85] F. Arash, M. J. Moravcsik, and G. R. Goldstein. *Dynamics-Independent Null Experiment for Testing Time-Reversal Invariance*. Physical Review Letters, **54** 2649(1985).

- [Bar83] V. G. Baryshevskii. *P- and T-violating Phenomena in the Passage of Neutrons through Matter Containing Polarized Nuclei*. Soviet Journal of Nuclear Physics, **38** 699(1983).
- [Bar86] A. L. Barabanov. *Violation of Time Parity in Neutron Interaction with Aligned Nuclei*. Soviet Journal of Nuclear Physics, **44** 755(1986).
- [Bar87] A. L. Barabanov. *Possibility of Experimental Study of the Correlation of Partial Neutron Amplitudes in Reactions with Oriented Nuclei*. Soviet Journal of Nuclear Physics, **45** 597(1987).
- [Bar89] J. Bartel, M. B. Johnson, and M. K. Singham. *Pion Single-Charge-Exchange Scattering and Nuclear Structure in Deformed Nuclei*. Annals of Physics, **195** 89(1989).
- [Ben89] R. Bengtsson, J. Dudek, W. Nazarewicz, and P. Olanders. *A Systematic Comparison between the Nilsson and Woods-Saxon Deformed Shell Model Potentials*. Physica Scripta, **39** 196(1989).
- [Bev69] Philip R. Bevington. *Data Reduction and Error Analysis for the Physical Sciences*. McGraw-Hill Book Company, 1969.
- [Bey89] M. Beyer. *Time-Reversal Invariance in Multipole Mixing Ratios*. Nuclear Physics, **A493** 335(1989).
- [Bha82] T. S. Bhatia, G. Glass, J. C. Hiebert, L. C. Northcliffe, W. B. Tippen, B. E. Bonner, J. E. Simmons, C. L. Hollas, C. R. Newsom, P. J. Riley, and R. D. Ransome. *Difference between Polarization and Analyzing Power for 800-MeV n-p Elastic Scattering: Test of Time-Reversal Invariance*. Physical Review Letters, **48** 227(1982).
- [Bla52] J. M. Blatt and V. F. Weisskopf. *Theoretical Nuclear Physics*. Wiley and Sons, 1952.

- [Bla64] W. C. Black, W. R. Roach, and J. C. Wheatley. *Speer Carbon Resistors as Thermometers for Use Below 1 K*. Review of Scientific Instruments, **35** 587(1964).
- [Bla83] E. Blanke, H. Driller, W. Glöckle, H. Genz, A. Richter, and G. Schrieder. *Improved Experimental Test of Detailed Balance and Time Reversibility in the Reactions $^{27}\text{Al} + p \rightleftharpoons ^{24}\text{Mg} + \alpha$* . Physical Review Letters, **51** 355(1983).
- [Boe88] Felix Boehm. *Time Reversal Tests with Polarized Nuclei - A Review*. Hyperfine Interactions, **43** 95(1988).
- [Boh87] A. Bohr and B. R. Mottelson. *Nuclear Structure: Single-Particle Motion*, volume 1, page 28. W. A. Benjamin, 1987.
- [Bow90a] J. D. Bowman, C. D. Bowman, J. E. Bush, P. P. J. Delheij, C. M. Frankle, C. R. Gould, D. G. Haase, J. Knudson, G. E. Mitchell, S. Penttila, H. Postma, N. R. Roberson, S. J. Seestrom, J. J. Szymanski, V. W. Yuan, and X. Zhu. *Parity Nonconservation for Neutron Resonances in ^{238}U* . Physical Review Letters, **65** 1192(1990).
- [Bow90b] J. D. Bowman, C. D. Bowman, J. Knudson, S. Penttila, S. J. Seestrom, J. J. Szymanski, V. W. Yuan, C. R. Gould, D. G. Haase, G. E. Mitchell, N. R. Roberson, P. P. J. Delheij, H. Postma, and E. D. Davis. *Search for Parity and Time Reversal Symmetry Violation Using Polarized Neutron-Nucleus Interactions*. In H. Henrikson and P. Vogel, editors, *Fundamental Symmetries in Nuclei and Particles*. World Scientific, 1990.
- [Bra58] A. Bratenahl, Peterson, and Stoering. Physical Review, **110** 927(1958).
- [Bri62] D. M. Brink and G. R. Satchler. *Angular Momentum*. Clarendon Press, 1962.

- [BS57] R. J. Blin-Stoyle and M. A. Grace. In S. Flügge, editor, *Handbuch der Physik V. XLII*, page 555. Springer-Verlag, 1957.
- [BS73] R. J. Blin-Stoyle. *Fundamental Interactions and the Nucleus*, chapter X. North-Holland, 1973.
- [Chr64] J. H. Christenson, J. W. Cronin, V. L. Fitch, and R. Turlay. *Physical Review Letters*, **13** 138(1964).
- [Cle89] Thomas B. Clegg. *Polarized H^- and D^- Source Development at the Triangle Universities Nuclear Laboratory*. In K. J. Heller, editor, *AIP Conference Proceedings 187*, page 1227, 1989. Particles and Fields Series 37, Series editor R. G. Lerner.
- [Cow88] R. A. Cowley and S. Bates. *The Magnetic Structure of Holmium: I*. *Journal of Physics C: Solid State Physics*, **21** 4113(1988).
- [Dav] E. D. Davis. private communication.
- [Dav86] C. A. Davis, L. G. Greeniaus, G. A. Moss, D. A. Hutcheon, C. A. Miller, R. Abegg, A. W. Stetz, W. C. Olsen, G. C. Neilson, G. Roy, and J. Uegaki. *Test of Time Reversal Invariance in p - p Elastic Scattering at 198.5 MeV*. *Physical Review C*, **33** 1196(1986).
- [DeG65] S. R. DeGroot, H. A. Tohloek, and W. J. Huiskamp. In K. Siegbahn, editor, *Alpha-, Beta-, and Gamma-Ray Spectroscopy*, page 1199. North-Holland, 1965.
- [DeL71] L. E. DeLong, O. G. Symko, and J. C. Wheatley. *Continuously Operating ^4He Evaporation Refrigerator*. *Review of Scientific Instruments*, **42** 147(1971).

- [Del81] J. P. Delaroche, G. Haouat, J. Lachkar, Y. Patin, J. Sigaud, and J. Chardine. *Deformations, Moments, and Radii of $^{182,183,184,186}W$ from Fast Neutron Scattering*. Physical Review C, **23** 136(1981).
- [Del82] J. P. Delaroche. *Sensitivity of Tungsten Neutron Cross Sections to Target Band Mixing and β_6 Deformation*. Physical Review C, **26** 1899(1982).
- [deR89] E. M. M. deRas, J. P. Vaane, and W. van Suetendael. *Investigation of the Nature of a Contamination Caused by Tritium Targets used for Neutron Production*. In *U.S. Sixth Coordination Meeting for the Program to Meet Nuclear Data Needs for Fusion Energy*, page 119, 1989.
- [Don76] T. R. Donoghue, Sr. M. A. Doyle, H. W. Clark, L. J. Dries, J. L. Regner, W. Tornow, R. C. Byrd, P. W. Lisowski, and R. L. Walter. *Equality of Analyzing Power and Polarization in the Reaction $^3H(p,n)^3He$* . Physical Review Letters, **37** 981(1976).
- [Dri79] H. Driller, E. Blanke, H. Genz, A. Richter, G. Schrieder, and J. M. Pearson. *Test of Detailed Balance at Isolated Resonances in the Reactions $^{27}Al + p \rightleftharpoons ^{24}Mg + \alpha$ and Time Reversibility*. Nuclear Physics, **A317** 300(1979).
- [Fag76] R. L. Fagaly and R. G. Bohn. *Simple Method for Determining Molar Flow Rates in Dilution Refrigerators*. Review of Scientific Instruments, **47** 1307(1976).
- [Fas73] U. Fasoli, G. Galeazzi, D. Toniolo, and G. Zago. *Fast-Neutron Transmission through a Polarized Holmium Target*. Lettere al Nuovo Cimento, **6** 485(1973).

- [Fas78] U. Fasoli, G. Galeazzi, P. Pavan, D. Toniolo, G. Zago, and R. Zannoni. *The Spin-Spin Effect in the Total Neutron Cross Section of Polarized Neutrons on Polarized ^{165}Ho* . Nuclear Physics, **A311** 368(1978).
- [Fis67] T. R. Fisher, R. S. Safrata, E. G. Shelley, J. McCarthy, S. M. Austin, and R. C. Barrett. *Interaction of Fast Neutrons with Oriented Ho^{165}* . Physical Review, **157** 1149(1967).
- [Fra75] H. Frauenfelder and E. M. Henley, editors. *Nuclear and Particle Physics*. Benjamin/Cummings, 1975.
- [Fre87] J. B. French, A. Pandey, and J. Smith. *Compound-Nuclear Tests of Time Reversal Invariance in the Nucleon-Nucleon Interaction*. In N. R. Roberson, C. R. Gould, and J. D. Bowman, editors, *Tests of Time Reversal Invariance in Neutron Physics*. World Scientific, 1987.
- [Fre88] J. B. French, V. K. B. Kota, A. Pandey, and S. Tomsovic. *Statistical Properties of Many-Particle Spectra VI. Fluctuation Bounds on N-N T-Noninvariance*. Annals of Physics, **181** 235(1988).
- [Fro77] G. Frosatti, H. Godfrin, B. Hébral, G. Schumacher, and D. Thoulouze. *Conventional Cycle Dilution Refrigeration Down to 2.0 mK*. In *Physics at Ultralow Temperatures*, page 205. Physical Society of Japan, 1977. Proceedings of ULT Hakone Symposium.
- [Gim81] J. L. Gimlett, H. E. Henrikson, N. K. Cheung, and F. Boehm. *Atomic Final State Effects and a Limit for Time Reversal Invariance in ^{191}Ir* . Physical Review C, **24** 620(1981).
- [Gle68] N. K. Glendenning, D. L. Hendrie, and O. N. Jarvis. *Relation between the Optical Potential for Spherical and Deformed Nuclei*. Physics Letters, **26B** 131(1968).

- [Gou81] C. R. Gould, L. L. Holzweig, S. E. King, Y. C. Lau, R. V. Poore, N. R. Roberson, and S. A. Wender. *The XSYS Data Acquisition System at Triangle Universities Nuclear Laboratory*. IEEE Transactions in Nuclear Science, **NS-28** 3708(1981).
- [Gou87] C. R. Gould, D. G. Haase, J. P. Soderstrum, L. W. Seagondollar, M. B. Schneider, and N. R. Roberson. *Tests of Time Reversal Invariance with MeV Neutrons and Polarized and Aligned Holmium*. In N. R. Roberson, C. R. Gould, and J. D. Bowman, editors, *Tests of Time Reversal Invariance in Neutron Physics*. World Scientific, 1987.
- [Gou90] C. R. Gould, D. G. Haase, N. R. Roberson, H. Postma, and J. D. Bowman. *Parity and Time Reversal Violation in Resonance Neutron Total Cross Sections with Polarized Targets*. International Journal of Modern Physics A, **5** 2181(1990).
- [Hai72] R. C. Haight, J. E. Simmons, and T. R. Donoghue. *Polarization and Polarization Transfer in the Reaction $T(p,n)^3\text{He}$* . Physical Review C, **5** 1826(1972).
- [Hal84] A. L. Hallin, F. P. Calaprice, D. W. MacArthur, L. E. Pilonen, M. B. Schneider, and D. F. Schreiber. *Test of Time-Reversal Symmetry in the β Decay of ^{19}Ne* . Physical Review Letters, **52** 337(1984).
- [Har90] H. L. Harney, A. Hüpper, and A. Richter. *Ericson Fluctuations, Detailed Balance and Time-Reversal Invariance*. Nuclear Physics A, **518** 35(1990).
- [Hen68] D. L. Hendrie, N. K. Glendenning, B. G. Harvey, O. N. Jarvis, H. H. Duhm, J. Saudinos, and J. Mahoney. *Determination of Y_{40} and Y_{60} Components in the Shapes of Rare Earth Nuclei*. Physics Letters, **26B** 127(1968).

- [Hni87] V. Hnizdo and K. W. Kemper. *Spin-Spin Dependence of Total Cross Sections as an Effect of Static Nuclear Deformation*. Physical Review Letters, **59** 1892(1987).
- [Jai90] A. K. Jain, R. K. Sheline, P. C. Sood, and K. Jain. *Intrinsic States of Deformed Odd-A Nuclei in Mass Regions ($151 \leq A \leq 193$) and ($A \geq 221$)*. Reviews of Modern Physics, **62** 393(1990).
- [Kab82] P. K. Kabir. *Test of T Invariance in Neutron Optics*. Physical Review D, **25** 2013(1982).
- [Kab86] P. K. Kabir. *The Investigation of Fundamental Interactions with Cold Neutrons*. In G. L. Greene, editor, *NBS Special Publication 711*, page 81, 1986.
- [Kab88a] P. K. Kabir. *Polarization-Asymmetry Relations in Neutron Optics*. Physical Review Letters, **60** 686(1988).
- [Kab88b] P. K. Kabir. *Transformation of Neutron Polarization in Polarized Media and Tests of T Invariance*. Physical Review D, **37** 1856(1988).
- [Knu90] J. N. Knudson, J. D. Bowman, S. I. Penttilä, J. R. Comfort, B. G. Ritchie, J. Goergen, D. Mathis, J. Tinsley, S. S. Hanna, B. King, D. Počanić, R. A. Loveman, L. S. Fritz, and N. S. Dixon. *Neutron Deformation in ^{165}Ho* . submitted to Physical Review Letters, (1990).
- [Koe66] W. C. Koehler, J. W. Cable, M. K. Wilkinson, and E. O. Wollan. *Magnetic Structures of Holmium I: The Virgin State*. Physical Review, **151** 414(1966).
- [Kos89] J. E. Koster, D. G. Haase, and R. G. Goodrich. *Comment on Superconducting Fixed Points and Interpolations*. Cryogenics, **29** 1017(1989).

- [Kra73] K. S. Krane. *Orientation Parameters for Low-Temperature Nuclear Orientation*. Nuclear Data Tables, **11** 407(1973).
- [Kru69] M. Krusius, A. C. Anderson, and B. Holström. *Calorimetric Investigation of Hyperfine Interactions in Metallic Ho and Tb*. Physical Review, **177** 910(1969).
- [Li86] Q. Li, C. H. Watson, R. G. Goodrich, D. G. Haase, and H. Lukefahr. *Thick Film Chip Resistors for Use as Low Temperature Thermometers*. Cryogenics, **26** 467(1986).
- [Lim86] C. C. Lim. *Indium Seals for Low-Temperature and Moderate-Pressure Applications*. Review of Scientific Instruments, **57** 108(1986).
- [Lis73] Horst Liskien and Arno Paulsen. *Neutron Production Cross Sections and Energies for the Reactions $T(p,n)^3\text{He}$, $D(d,n)^3\text{He}$, and $T(d,n)^4\text{He}$* . Nuclear Data Tables, **11** 569(1973).
- [Llo51] S. P. Lloyd. Physical Review, **83** 716(1951).
- [Löb70] K. E. G. Löbner, M. Vetter, and V. Hönig. *Nuclear Intrinsic Quadrupole Moments and Deformation Parameters*. Nuclear Data Tables, **A7** 495(1970).
- [Lou74] O. V. Lounasmaa. *Experimental Principles and Methods Below 1 K*. Academic Press, 1974.
- [Lüd57] G. Lüders. *Proof of the TCP Theorem*. Annals of Physics, **2** 1(1957).
- [Mar66] H. Marshak, A. C. B. Richardson, and T. Tamura. *Effect of Nuclear Alignment on the 14-MeV Total Neutron Cross Section of ^{165}Ho* . Physical Review, **150** 996(1966).

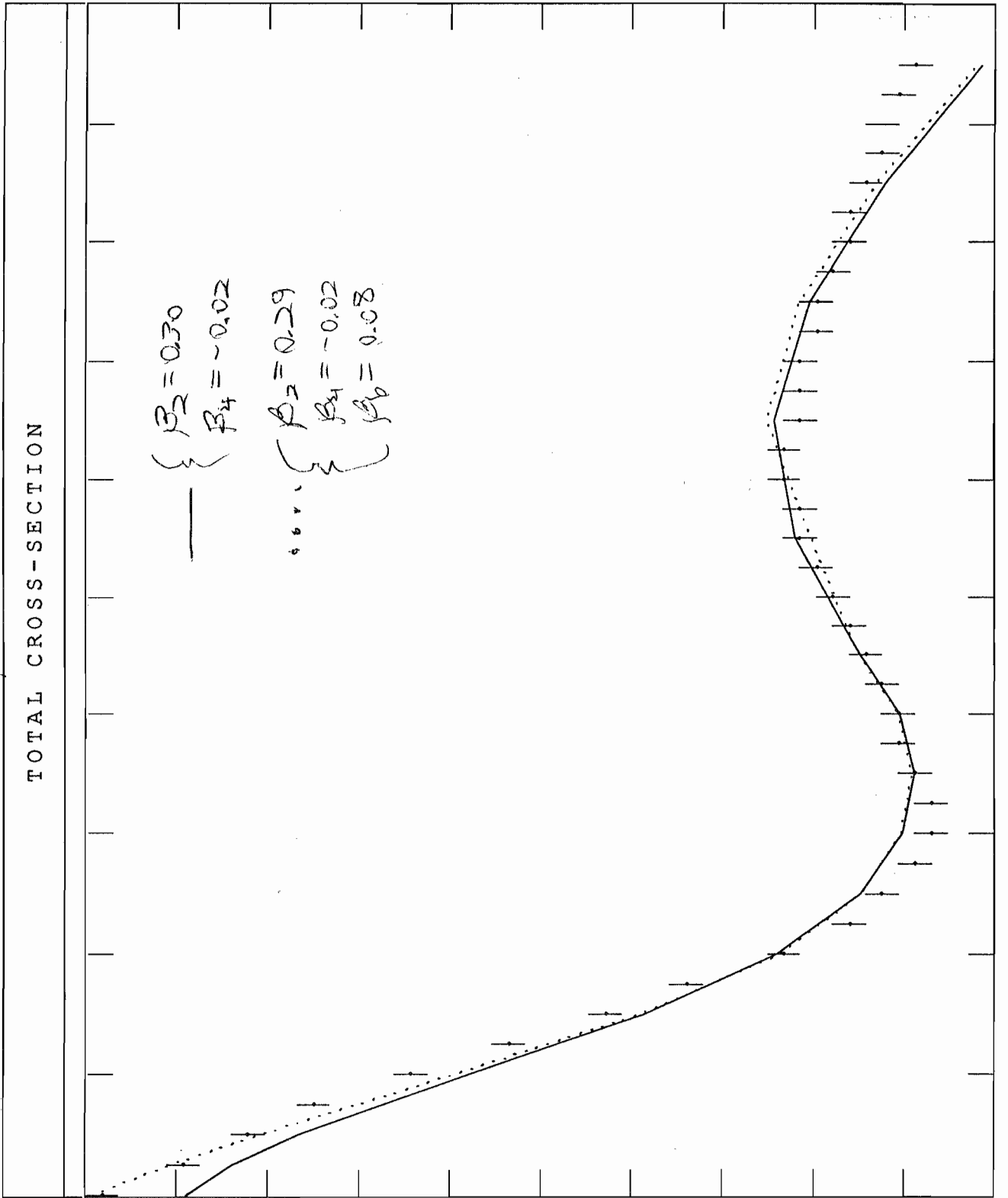
- [Mar70] H. Marshak, A. Langsford, T. Tamura, and C. Y. Wong. *Total Neutron Cross Section of Oriented ^{165}Ho from 2 to 135 MeV*. Physical Review C, **2** 1862(1970).
- [Mar79] H. Marshak and B. G. Turrell. *γ -Ray Emission from Oriented Nuclei in a Multiaxis Nuclear Spin System: $^{166m}\text{Ho}^{165}\underline{\text{Ho}}$* . Solid State Communications, **30** 677(1979).
- [McC68] J. S. McCarthy, T. R. Fisher, E. G. Shelley, R. S. Safrata, and D. Healey. *Inversion in the Deformation Effect for Neutron Transmission Through Oriented Ho^{165}* . Physical Review Letters, **20** 502(1968).
- [McC84] P. V. E. McClintock. *Matter at Low Temperatures*. Wiley, 1984.
- [McL88] V. McLane, C. L. Dunford, and P. F. Rose. *Neutron Cross Sections*, volume 2. Academic Press, 1988.
- [Mol68a] P. A. Moldauer. *Effects of T Violation in Nuclear Reactions*. Physical Review, **165** 1136(1968).
- [Mol68b] P. A. Moldauer. *T-Violation and Detailed Balance in Direct Reactions*. Physics Letters, **26B** 713(1968).
- [Naz90] W. Nazarewicz, M. A. Riley, and J. D. Garrett. *Equilibrium Deformations and Excitation Energies of Single-Quasiproton Band Heads of Rare-Earth Nuclei*. Nuclear Physics, **A512** 61(1990).
- [Pow75] R. J. Powers, F. Boehm, P. Vogel, A. Zehnder, T. King, A. R. Kunselman, P. Roberson, P. Martin, G. H. Miller, R. E. Welsh, and D. A. Jenkins. *Precise Determination of E2 and E4 Moments in ^{165}Ho from Muonic X Rays*. Physical Review Letters, **34** 492(1975).

- [Ray70] J. Raynal. *Optical Model and Coupled-Channel Calculations in Nuclear Physics*. Technical Report IAEA-SMR-9/8, International Atomic Energy Agency, 1970.
- [Roa54] Raymond J. Roark. *Formulas for Stress and Strain*. McGraw-Hill, third edition, 1954.
- [Rob81] N. R. Roberson and S. E. Edwards. *Interface for the TUNL VAX Data Acquisition Facility*. IEEE Transactions in Nuclear Science, NS-28 3834(1981).
- [Rom65] W. A. Roman. *The Metallographic Preparation of Some Rare-Earth Metals*. Journal of Less-Common Metals, 10 150(1965).
- [Ros81] R. Rosenbaum and A. Breuer. *Simple and Efficient Step Heat Exchangers*. Physica, 107B 593(1981).
- [Sac87] Robert G. Sachs. *The Physics of Time Reversal*. University of Chicago Press, 1987.
- [Sim73] J. E. Simmons, W. B. Broste, T. R. Donoghue, R. C. Haight, and J. C. Martin. *Sources of Polarized Neutrons from 2 to 33 MeV using Polarization Transfer Reactions at 0°*. Nuclear Instruments and Methods, 106 477(1973).
- [Sim74] M. Simonius. *Theory of Polarization Measurements, Observables, Amplitudes and Symmetries*, volume 30 of *Lecture Notes in Physics*. Springer-Verlag, 1974.
- [Smi88] Eric N. Smith. *Cryogenic Design Aids: Recipes*. In Robert. C. Richardson and Eric N. Smith, editors, *Experimental Techniques in Condensed Matter Physics at Low Temperatures*. Addison-Wesley Publishing Company, 1988. Frontiers in Physics 67.

- [Sod88] J. P. Soderstrum, C. R. Gould, D. G. Haase, L. W. Seagondollar, M. B. Schneider, and N. R. Roberson. *Limits on P- and P, T-violating Absorption of MeV Neutrons in ^{165}Ho* . Physical Review C, **38** 2424(1988).
- [Ste67] William A. Steyert, Jr. *Thermal Transport Across Superconducting Solder Joints Near 0.1 K*. Review of Scientific Instruments, **38** 964(1967).
- [Ste89] A. M. Stewart and S. J. Collocott. *The Specific Heat of Samarium and Holmium in the Range 2–32 K*. Journal of Physics: Condensed Matter, **1** 677(1989).
- [Sto82] Leo Stodolsky. *Parity Violation in Threshold Neutron Scattering*. Nuclear Physics, **B197** 213(1982).
- [Sto86a] Leo Stodolsky. *Novel Time-Reversal Tests in Low-Energy Neutron Propagation*. Physics Letters B, **172** 5(1986).
- [Sto86b] N. J. Stone and H. Postma, editors. *Low-Temperature Nuclear Orientation*. Elsevier Science Publishing Company, Inc., 1986. (North-Holland Physics Publishing).
- [Str62] D. L. Strandburg, S. Legvold, and F. H. Spedding. *Electrical and Magnetic Properties of Holmium Single Crystals*. Physical Review, **127** 2046(1962).
- [Tam65] Taro Tamura. *Analyses of the Scattering of Nuclear Particles by Collective Nuclei in Terms of the Coupled-Channels Calculation*. Reviews of Modern Physics, **17** 679(1965).
- [Toh53] H. A. Tohloek and J. A. M. Cox. Physica, **19** 101(1953).
- [Tor81] W. Tornow, R. C. Byrd, P. W. Lisowski, R. L. Walter, and T. R. Donoghue. *Comparison of Analyzing Power and Polarization in the Reaction $^3\text{H}(p, n)^3\text{He}$ (II)*. Nuclear Physics, **A371** 235(1981).

- [Tra73] N. Trautner, G. Løvholden, and P. R. Christensen. *Elastic and Inelastic Deuteron Scattering from ^{152}Sm and ^{162}Dy* . Physics Letters, **44B** 41(1973).
- [Tre84] R. P. Trelle, J. Birkhäuser, F. Hinterberger, S. Kuhn, D. Prasuhn, and P. Von Rossen. *No Evidence for Time Reversal Invariance Violation from $(^3\text{He},\vec{p})$ Polarization Measurements*. Physics Letters, **134B** 34(1984).
- [Wag65] R. Wagner, P. D. Miller, T. Tamura, and H. Marshak. *Interaction of 350-keV Polarized Neutrons with Oriented ^{165}Ho Nuclei*. Physical Review, **139** B 29(1965).
- [Wei90] Hans A. Weidenmüller. *What Can We Learn from Tests of Fundamental Symmetries in Compound-Nucleus Reactions?* In H. Henrikson and P. Vogel, editors, *Fundamental Symmetries in Nuclei and Particles*. World Scientific, 1990.
- [Whe68] J. C. Wheatley, O. E. Vilches, and W. R. Abel. *Principles and Methods of Dilution Refrigeration*. Physics, **4** 1(1968).
- [Whe74] J. C. Wheatley, R. E. Rapp, and R. T. Johnson. *Principles and Methods of Dilution Refrigeration II*. Journal of Low Temperature Physics, **4** 1(1974).
- [You83] P. G. Young, E. D. Arthur, C. Philis, P. Nagel, and M. Collin. *Analysis of $n+^{165}\text{Ho}$ and ^{169}Tm Reactions*. In K. H. Böckhoff, editor, *Nuclear Data for Science and Technology*, page 792. D. Reidel Publishing Company, 1983. Proceedings of the International Conference, Antwerp, September 1982.

$$V_R = V_{y, \text{max}} - 0.01 E^2 \quad r = 1.26$$



7500
7220
6940
6660
6380
6100
5820
5540
5260
4980
4700

S I G M A O m b

3 7 11 15 19

Neutron Energy (MeV)